HIGH AVERAGE POWER YB:YAG THIN DISK LASER AND ITS APPLICATION FOR AN RGB LASER SOURCE

A dissertation submitted to the

SWISS FEDERAL INSTITUTE OF TECHNOLOGY ZURICH

for the degree of

DOCTOR OF NATURAL SCIENCES

presented by

EDITH INNERHOFER

Dipl.-Phys. (Swiss Federal Institute of Technology Zurich, Switzerland)
born on March 16, 1975
citizen of Willisau Land (LU) and Italy

accepted on the recommendation of
Prof. Dr. U. Keller, Supervisor
Prof. Dr. T. Esslinger, Co-Examiner
PD Dr. R. Paschotta, Co-Examiner

Mai 2005

Table of Contents

List of Abbreviations and Physical Symbols

AC	autocorrelation
A_L	laser mode area in the gain medium
AlAs	aluminum arsenide
AlGaAs	aluminum gallium arsenide
APM	additive pulse mode locking
AR	antireflective, antireflection
$\chi^{(2)}$	second-order nonlinearity of a medium
γ_{SPM}	nonlinear coefficient of self phase modulation
CIE	Commission Internationale de l'Eclairage
CLT	congruent lithium tantalate
cw	continuous-wave
ΔR	modulation depth
ΔR_{ns}	nonsaturable losses
D	amount of intracavity group delay dispersion
D65	D65 white light (ISO 10526:1999/CIE S005/E-1998 standard)
DM	dispersive mirror
E_P	pulse energy
$E_{sat,L}$	saturation energy of the gain medium
E_{satA}	saturation energy of the absorber
f_{rep}	fundamental repetition rate
fs	femtosecond
$F_{sat,A}$	saturation fluence of the saturable absorber
$F_{sat,L}$	saturation fluence of the gain medium
FWHM	full width at half maximum
GaAs	gallium arsenide
GDD	group delay dispersion
GHz	gigahertz
GTI	Gires–Tournois interferometer
GVM	group velocity mismatch
GW	gigawatt
HDTV	high-definition television

HR	high reflectivity
HT	high transmission
InGaAs	indium gallium arsenide
kHz	kilohertz
KLM	Kerr lens mode locking
λ_L	laser wavelength
λ_P	pump wavelength
$\lambda/2$	half-wave plate
LBO	lithium triborate (LiB_3O_5)
$LiNbO_3$	lithium niobate
$LiTaO_3$	lithium tantalate
LMA	large mode area
lm	lumen. Amount of light that falls on a unit area at unit distance from a light source of one candela (a 100 W light bulb emits $\approx$ 120 candela and has an output of $\approx$ 1400 lm)
LT	low temperature
μJ	microjoule
μm	micrometer
M^2	transverse beam quality factor
MBE	molecular beam epitaxy
Mg:SLN	MgO-doped stoichoimetric lithium niobate
Mg:SLT	MgO-doped stoichoimetric lithium tantalate
MHz	megahertz
ML	mode–locked or mode locking
MOCVD	metal organic chemical vapor deposition
MW	megawatt
n_2	nonlinear refractive index
Nd:Glass	neodymium-doped glass
Nd:YAG	neodymium-doped yttrium aluminum garnet ($Nd^{3+}:Y_3Al_5O_{12}$)
nm	nanometer
OPA	optical parametric amplifier/amplification
OPG	optical parametric generator/generation
OPO	optical parametric oscillator/oscillation
PBS	polarizing beam splitter
PICASO	phase and intensity from correlation and spectrum only
PPLN	periodically poled lithium niobate
PPLT	periodically poled lithium tantalate

PPMgSLT	periodically poled MgO-doped stoichoimetric lithium tantalate
PPSLT	periodically poled stoichiometric lithium tantalate
ps	picosecond
QML	Q–switched mode locking
RGB	red-green-blue
R_{ns}	nonsaturable reflectivity
ROC	radius of curvature
$\sigma_{abs, L}$	absorption cross section at the laser wavelength
$\sigma_{em, L}$	emission cross section at the laser wavelength
SESAM	semiconductor saturable absorber mirror
SF10	schott glass SF10
SFG	sum frequency generator/generation
SHB	spatial hole burning
SHG	second-harmonic generator/generation
SLN	stoichiometric lithium niobate
SLT	stoichiometric lithium tantalate
SPM	self phase modulation
τ_A	absorber recovery time (1/e decay time)
τ_P	FWHM pulse duration (1/e)
τ_{rad}	fluorescence lifetime (1/e decay time)
TBP	time-bandwidth product
TEM_{00}	transverse electromagnetic ground mode
T_{oc}	output coupler transmission
W	watt
x, y, z	chromaticity coordinates
X, Y, Z	imaginary primary values
X, Y, Z	imaginary primaries
Yb	ytterbium (Yb^{3+})
Yb:KGW	ytterbium-doped potassium gadolinium tungstate (Yb^{3+}:$KGd(WO_4)_2$)
Yb:KYW	ytterbium-doped potassium yttrium tungstate (Yb^{3+}:$KY(WO_4)_2$)
Yb:YAG	ytterbium-doped yttrium aluminum garnet (Yb^{3+}:$Y_3Al_5O_{12}$)

Table of Figures

Publications

*Parts of this thesis are published in the following
journal papers and conference proceedings:*

Journal Papers

1. E. Innerhofer, F. Brunner, S. V. Marchese, R. Paschotta, G. Arisholm, T. Usami, H. Ito, S. Kurimura, K. Kitamura, and U. Keller, "Analysis of nonlinear wavelength conversion system for a red-green-blue laser projection source," *submitted to* JOSA B (2005).

2. S. V. Marchese, E. Innerhofer, R. Paschotta, S. Kurimura, K. Kitamura, G. Arisholm and U. Keller, "Room temperature femtosecond optical parametric generation in MgO-doped stoichiometric $LiTaO_3$," *submitted to* Opt. Lett. (2005).

3. G. J. Spühler, L. Krainer, E. Innerhofer, R. Paschotta, K. J. Weingarten and U. Keller, "Soliton mode-locked Er:Yb:glass laser," Opt. Lett 30, 263 (2004).

4. F. Brunner, E. Innerhofer, S. V. Marchese, T. Südmeyer, R. Paschotta, T. Usami, H. Ito, S. Kurimura, K. Kitamura, G. Arisholm and U. Keller, "Powerful RGB laser source pumped with a mode-locked thin disk laser," Opt. Lett. 29, 1921 (2004).

5. E. Innerhofer, F. Brunner, S. V. Marchese, T. Südmeyer, R. Paschotta and U. Keller, "RGB Source Powers Up Laser Projection Displays," Photonics Spectra, June (2004).

6. E. Innerhofer, T. Südmeyer, F. Brunner, R. Paschotta and U. Keller, "Mode-locked high-power lasers and nonlinear optics - a powerful combination," Laser Phys. Lett. 1, 82 (2004).

7. T. Südmeyer, E. Innerhofer, F. Brunner, R. Paschotta, U. Keller, T. Usami, H. Ito, M. Nakamura, K. Kitamura, D. C. Hanna, "High power femtosecond fiber-feedback OPO based on periodically poled stoichiometric $LiTaO_3$," Opt. Lett. 29, 1111 (2004).

8. T. Südmeyer, F. Brunner, E. Innerhofer, R. Paschotta, K. Furusawa, J. C. Baggett, T. M. Monro, D. J. Richardson, U. Keller, "Nonlinear femtosecond pulse compression at high average power levels by use of a large area holey fiber," Opt. Lett. 28, 1951 (2003).

9. E. Innerhofer, T. Südmeyer, F. Brunner, R. Häring, A. Aschwanden, R. Paschotta, U. Keller, C. Hönninger, M. Kumkar, "60 W average power in 810-fs pulses from a thin-disk Yb:YAG laser," Opt. Lett. 28, 367 (2003).

10. F. Brunner, T. Südmeyer, E. Innerhofer, R. Paschotta, F. Morier-Genoud, J. Gao, K. Contag, A. Giesen, V. E. Kisel, V. G. Shcherbitsky, N. V. Kuleshov, U. Keller, "240-fs pulses with 22–W average power from a mode-locked thin-disk Yb:KY(WO$_4$)$_2$ laser," *Opt. Lett.* **27**, 1162 (2002).

Conference Papers

1. S. V. Marchese, E. Innerhofer, R. Paschotta, U. Keller, S. Kurimura and K. Kitamura, "Room temperature high power femtosecond optical parametric generation based on MgO-doped stoichiometric $LiTaO_3$", CLEO Europe and EQEC 2005, München (Germany), talk CD3-3-WED.

2. E. Innerhofer, F. Brunner, S. V. Marchese, R. Paschotta, U. Keller, K. Furusawa, J. C. Baggett, T. M. Monro and D. J. Richardson, "32 W of average power in 24-fs pulses from a passively mode-locked thin disk laser with nonlinear fiber compression", Advanced Solid-State Photonics (ASSP '05), Vienna, talk TuA3.

3. S. V. Marchese, E. Innerhofer, F. Brunner, T. Südmeyer, R. Paschotta, U. Keller, T. Usami, H. Ito, S. Kurimura and K. Kitamura, "Powerful RGB laser source based on a passively mode-locked thin disk laser", EPS- QEOD Europhoton Conference, Lausanne (Switzerland) 2004, talk TuD2.

4. E. Innerhofer, F. Brunner, T. Südmeyer, S. V. Marchese, R. Paschotta, U. Keller, T. Usami, H. Ito, S. Kurimura and K. Kitamura, "Powerful RGB laser source for projection displays based on a passively mode-locked thin disk laser", Conference on Lasers and Electro-Optics (CLEO '04), San Francisco (California), (invited presentation), talk CMU1.

5. F. Brunner, E. Innerhofer, T. Südmeyer, R. Paschotta, U. Keller, T. Usami, H. Ito, S. Kurimura and K. Kitamura, "Two-stage optical parametric generator with multi-Watt outputs in ultrashort pulses around 800 nm and 1450 nm", Advanced Solid-State Photonics (ASSP '04), Santa Fe (New Mexico), talk TuC1.

6. E. Innerhofer, T. Südmeyer, F. Brunner, R. Paschotta, and U. Keller, "Mode-locked high-power lasers and nonlinear optics - a powerful combination", LPHYS 2003 in Hamburg, (invited presentation), talk 5.1.3.

7. T. Südmeyer, F. Brunner, E. Innerhofer, R. Paschotta, U. Keller, T. Usami, H. Ito, M. Nakamura, K. Kitamura, K. Furusawa, J. C. Baggett, T. M. Monro, and D. J. Richardson, "High-Power Femtosecond Nonlinear Devices Pumped with a Mode-Locked Thin Disk Laser," CLEO Europe and EQEC 2003, München (Germany), (invited presentation), talk CE3-1-TUE.

8. F. Brunner, T. Südmeyer, E. Innerhofer, R. Paschotta, U. Keller, K. Furusawa, J. C. Baggett, T. M. Monro, and D. J. Richardson, "Sub-40-fs pulses with 18-W average power from a passively mode-locked thin disk Yb:YAG laser with nonlinear fiber compression," Conference on Lasers and Electro-Optics 2003, Baltimore (Maryland), talk CWM.

9. F. Brunner, T. Südmeyer, E. Innerhofer, R. Paschotta, and U. Keller, "Passively mode-locked high-power lasers and femtosecond high-power nonlinear frequency conversion," 11th International Conference Laser Optics 2003, St. Petersburg (Russia), (invited presentation), talk WeR1-29.

10. F. Brunner, T. Südmeyer, E. Innerhofer, R. Paschotta, U. Keller, K. Furusawa, J. C. Baggett, T. M. Monro, and D. J. Richardson, „Nonlinear femtosecond pulse compression at high average power levels using a large mode area holey fiber," LOYS-2003, St. Petersburg (Russia), talk ThS3-01.

11. E. Innerhofer, T. Südmeyer, F. Brunner, R. Häring, A. Aschwanden, R. Paschotta, C. Hönninger, M. Kumkar, and U. Keller, "Thin disk Yb:YAG lasers generating 60 W average power in picosecond or femtosecond pulses," Advanced Solid-State Photonics (ASSP '03), San Antonio (Texas), talk WE2.

12. T. Südmeyer, E. Innerhofer, F. Brunner, R. Paschotta, U. Keller, T. Usami, H. Ito, M. Nakamura, K. Kitamura, and D. C. Hanna, "Femtosecond fiber-feedback OPO with 18 W average power based on periodically poled stoichiometric $LiTaO_3$," Advanced Solid-State Photonics (ASSP '03), San Antonio (Texas), talk MD2.

13. T. Südmeyer, F. Brunner, E. Innerhofer, R. Paschotta, and U. Keller, "Novel ultrashort parametric systems based on passively mode-locked thin disk lasers with high average power", SPRC Annual Meeting in Stanford 2002, (invited presentation).

14. R. Paschotta, F. Brunner, E. Innerhofer, T. Südmeyer, and U. Keller, "Ultrashort pulses with high average power", talk at IQEC/LAT 2002 in Moscow, June 2002, **(invited presentation)**, talk JSuB1.

15. F. Brunner, T. Südmeyer, E. Innerhofer, R. Paschotta, F. Morier-Genoud, U. Keller, J. Gao, K. Contag, A. Giesen, V. E. Kisel, V. G. Shcherbitsky, and N. V. Kuleshov, "240-fs pulses with 22-W average power from a passively mode-locked thin-disk Yb:KY(WO$_4$)$_2$ laser", CLEO 2002 in Long Beach (California), talk CME3.

16. E. Innerhofer, T. Südmeyer, F. Brunner, R. Häring, A. Aschwanden, R. Paschotta, U. Keller, C. Hönninger, and M. Kumkar, "60 W average power in picosecond pulses from a passively mode-locked Yb:YAG thin-disk laser", CLEO 2002 in Long Beach (California), talk CTuD4.

17. R. Paschotta, F. Brunner, E. Innerhofer, T. Südmeyer, and U. Keller, "High average power femtosecond and picosecond lasers", Advanced Solid-State Lasers 2002 in Quebec City (Canada), February 2002, **(invited presentation)**, talk MC1.

Various talks

1. E. Innerhofer, "Mode-locked Yb:YAG thin disk laser and its application for an RGB (red-green-blue) laser system and for nonlinear fiber compression", Seminar talk, Mazur group at Harvard University, Cambridge, MA (2005).

2. E. Innerhofer, "Powerful RGB (red-green-blue) laser source for projection displays based on a passively mode-locked thin disk laser", Seminar talk, Quantum measurement group at MIT, Cambridge, MA (2005).

3. E. Innerhofer, F. Brunner, T. Südmeyer, S. V. Marchese, R. Paschotta, U. Keller, T. Usami, H. Ito, S. Kurimura and K. Kitamura, "Powerful RGB laser source for projection displays based on a passively mode-locked thin disk laser", Seminar talk, Spectra-Physics, Mountain-View, CA (2004).

4. F. Brunner, T. Südmeyer, E. Innerhofer, R. Paschotta, and U. Keller, „High-Power Femtosecond Lasers and Nonlinear Devices," New Focus Student Award Final Competition, Baltimore (MD, USA), June 2, 2003.

Abstract

This thesis describes the development of a passively mode-locked Yb:YAG thin disk laser with 80 W of average power in femtosecond pulses and its application as a pump source for several nonlinear optical devices.

Femtosecond lasers with high average output powers are attractive sources for many applications. Among those that greatly benefit from the high peak power of such laser systems are nonlinear wavelength conversion, micromachining and time-resolved spectroscopy.

In the first part, this thesis reports on the realization of an Yb:YAG laser delivering femtosecond pulses with unprecedented average power. This laser is based on the combination of a thin disk laser head and a semiconductor saturable absorber mirror (SESAM). The thin disk laser concept employs a sophisticated geometry of the gain medium that allows for high power laser operation with diffraction-limited beam quality. The SESAM on its part offers unique freedom in the design of important absorber parameters for stable and reliable passive mode locking. We demonstrate a first setup of the Yb:YAG thin disk laser for the generation of tunable pulses from 6-24 ps with up to 60 W of average power and a second setup delivering 80 W of average power in 705 fs pulses. In addition, we address the challenges that have to be overcome to scale the average power of a femtosecond thin disk laser to very high power levels.

The second part of this thesis is dedicated to how the limitations of the gain materials in terms of accessible wavelengths and obtainable pulse durations can be overcome with nonlinear optical devices. High average power mode-locked thin disk lasers with ultrashort pulse durations constitute ideal pump sources for nonlinear optical devices.

The range of accessible wavelengths can be greatly expanded by nonlinear frequency conversion. A first application of nonlinear frequency conversion is the generation of red, green, and blue (RGB) laser beams for large-scale projection displays. We experimentally demonstrate and numerically analyze an RGB laser system based on a high power femtosecond laser and subsequent frequency conversion stages that presents, compared to previously demonstrated systems, some significant advances in terms of simplicity and practicability. The pump source for the nonlinear conversion stages consists of a single laser oscillator without any amplifier stages. The system does not require any resonant cavities, and all nonlinear crystals except one are operated at room temperature. The RGB laser source simultaneously generates average powers of 8 W at 603 nm, 23 W at 515 nm, and 10.1 W at 450 nm.

The remaining temperature-stabilized crystal in the optical parametric generator (OPG) of the RGB system can in the future be replaced with a crystal operated at room temperature without temperature stabilization. We present a room temperature OPG based on MgO-doped $LiTaO_3$ with a signal average power of up to 2.4 W at a wavelength of 1484 nm. Even higher powers in the signal and idler waves can be generated with a *fiber-feedback* optical parametric oscillator (OPO). A *fiber-feedback* OPO is a high gain OPO with a signal feedback through a single-mode fiber. It exhibits attractive properties such as a compact setup, low sensitivity to cavity losses and low sensitivity to detuning of the cavity length. We report on a *fiber-feedback* OPO generating 19 W of average power in 840-fs pulses at a wavelength of 1448 nm.

The obtainable range of pulse durations of a thin disk laser is set by the laser material and can be expanded with external pulse compression. We demonstrate pulse compression in a large mode area microstructured (holey) fiber to a pulse duration of 24 fs while maintaining an average power of 32 W at the full laser repetition rate of 57 MHz. This system delivers 16 MW of peak power in a linearly polarized and nearly diffraction-limited beam. With such performance, applications in strong-field physics at unprecedented repetition rates are within reach.

Kurzfassung (German)

Diese vorliegende Doktorarbeit beschreibt die Entwicklung eines passiv modengekoppelten Scheibenlasers mit einer hohen mittleren Leistung von 80 W in Femtosekundenpulsen und seine Anwendung als Pumpquelle für verschiedene nichtlineare optische Systeme.

Modengekoppelte Laser mit hoher mittlerer Ausgangsleistung sind attraktiv für eine Vielzahl von Anwendungen. Beispiele für Anwendungen, welche von der hohen Spitzenleistung solcher Laser profitieren sind nichtlineare Frequenzkonversion, Feinbearbeitung von Werkstoffen oder zeitaufgelöste Spektroskopie.

Der erste Teil dieser Doktorarbeit beschreibt die Realisierung eines Yb:YAG Lasers mit Femtosekundenpulsen und einer bisher unerreichten hohen mittleren Leistung. Dieser Laser basiert auf der Kombination von einem Scheibenlaser mit einem sättigbaren Halbleiterspiegel (SESAM). Das Scheibenlaserkonzept verwendet eine raffinierte Geometrie des Verstärkermediums, welches hohe Leistungen mit beugungsbegrenzter Strahlqualität ermöglicht. SESAMs ihrerseits bieten eine einzigartige Freiheit in der Wahl der relevanten Absorberparameter, um stabile und zuverlässige Modenkopplung zu erreichen. Wir stellen einen ersten Laseraufbau des Yb:YAG-Scheibenlasers vor für die Erzeugung von abstimmbaren Pulsdauern von 6-24 ps mit einer mittleren Leistung von bis zu 60 W und einen zweiten Aufbau für die Erzeugung einer mittleren Leistung von 80 W in Pulsen von 705 fs Dauer. Weiter sprechen wir die Herausforderungen an, die zur Skalierung eines Scheibenlasers mit Femtosekundenpulsen zu sehr hohen mittleren Ausgangsleistungen überwunden werden müssen.

Der zweite Teil dieser Doktorarbeit widmet sich der Überwindung der Einschränkungen der Lasermaterialien für Hochleistungs-Femtosekundenlaser

in Bezug auf deren erreichbare Wellenlängen und möglichen Pulsdauern. Modengekoppelte Scheibenlaser mit hoher mittlerer Leistung und Femtosekundenpulsen stellen ideale Pumpquellen für nichtlineare optische Systeme dar.

Der Bereich zugänglicher Wellenlängen kann mit nichtlinearer Frequenzkonversion bedeutend erweitert werden. Eine erste Anwendung nichtlinearer Frequenzkonversion in dieser Doktorarbeit ist die Erzeugung von roten, grünen und blauen (RGB) Laserstrahlen für grossflächige Projektionen von Bildern oder Filmen. Wir stellen experimentelle Resultate und eine ausfühliche nummerische Analyse einer RGB Laserquelle vor, die auf einem Hochleistungs-Femtosekundenlaser und auf aufeinanderfolgenden Frequenz-konversionsstufen basiert und bedeutende Fortschritte im Vergleich zu früher demonstrierten Systemen im Bezug auf Einfachheit und praktischer Anwendbarkeit beinhaltet. Die ganze für die nichtlinearen Frequenz-konversionsstufen benötigte Pumpleistung wird durch einen einzelnen Laseroszillator ohne Verstärkerstufen bereitgestellt. Das System benötigt keine resonanten Kavitäten, und alle nichtlinearen Kristalle bis auf einen werden bei Raumtemperatur betrieben. Die RGB-Laserquelle erzeugt gleichzeitig mittlere Leistungen von 8 W bei 603 nm, 23 W bei 515 nm und 10.1 W bei 450 nm.

Der letzte temperatur-stabilisierte Kristall im optisch parametrischen Generator (OPG) der RGB Laserquelle wird in Zukunft ebenfalls mit einem Kristall ersetzt werden können, der bei Raumtemperatur ohne Temperatur-stabilisierung betrieben wird. Deshalb demonstrieren wir einen OPG basierend auf MgO-dotiertem LiTaO$_3$ mit einer mittleren Signalleistung von bis zu 2.4 W bei einer Wellenlänge von 1448 nm. Noch höhere mittlere Leistungen von Signal- und Idlerwellen können mittels eines *fiber-feedback* optisch parametrischen Oscillators (OPO) erzeugt werden. Ein *fiber-feedback* OPO ist ein OPO mit einer hohen parametrischen Verstärkung und mit Signalrückkopplung durch eine Faser. Dieses System weist attraktive Eigenschaften auf wie zum Beipiel einen kompakten Aufbau und eine geringe Empfindlichkeit auf Kavitätsverluste sowie auf Veränderungen der Kavitätslänge. Wir berichten über einen *fiber-feedback* OPO mit 19 W mittlerer Leistung in 840 fs Pulsen bei einer Signalwellenlänge von 1448 nm.

Der Bereich von zugänglichen Pulsdauern eines Scheibenlasers ist durch die Lasermaterialien eingeschränkt und kann mittels externer Pulsverkürzung deutlich erweitert werden. Wir demonstrieren Pulsverkürzung in einer mikro-strukturierten Faser mit grosser effektiver Querschnittsfläche zu einer Pulsdauer von 24 fs unter Beibehaltung einer hoher mittleren Leistung von 32 W bei der vollen Pulswiederholrate des Lasers von 57 MHz. Die Spitzenleistung dieses Systems beträgt 16 MW in einem linear polarisierten und nahezu beugungsbegrenzten Strahl. Mit einer solcher Leistung könnten Experimente im Gebiet der Hochintensitätsphysik mit bisher unerreicht hohen Pulswiederholraten möglich werden.

Chapter 1

Introduction and Motivation

In the forty five years since the first successful demonstration of a laser[1] by Maiman in 1960 [1], lasers have become widespread devices and can be found in almost every aspect of our life such as in medicine, biology, metrology, information technology, and entertainment, to name only a few. Regarding this extraordinary growing demand of lasers, it seems justified to enquire about the reason for this immense success. This reason certainly lies in the unique property of the radiation that a laser emits. Among the most outstanding characteristics of a laser is the high degree of spatial and temporal coherence. Spectral properties can vary from an octave-spanning bandwidth to monochromatic light. The laser output can be continuous-wave or pulsed, with pulse durations as short as a few femtoseconds. When tightly focused, immense intensities can be achieved.

The first diode-pumped laser was demonstrated in 1964 [2] and the benefits of diode pumping over lamp pumping have already been discussed in an early review paper by Byer [3]. However, only in the mid-1980s, with the introduction of epitaxial processes and a greatly increased sophistication in the junction structure of gallium arsenide (GaAs) devices, laser diodes became commercially available with output powers of several watts. These were the first devices with sufficient power to render them useful for the pumping of Nd:YAG lasers. The benefits of diode-pumped lasers include compactness, high

---

[1] "Laser" is an acronym for light amplification by stimulated emission of radiation.

efficiency, reduced thermal effects in the gain medium, and a long lifetime. Decreasing costs of diode lasers and increasing diode powers have gone hand-in-hand and triggered an increasing demand on diode-pumped lasers.
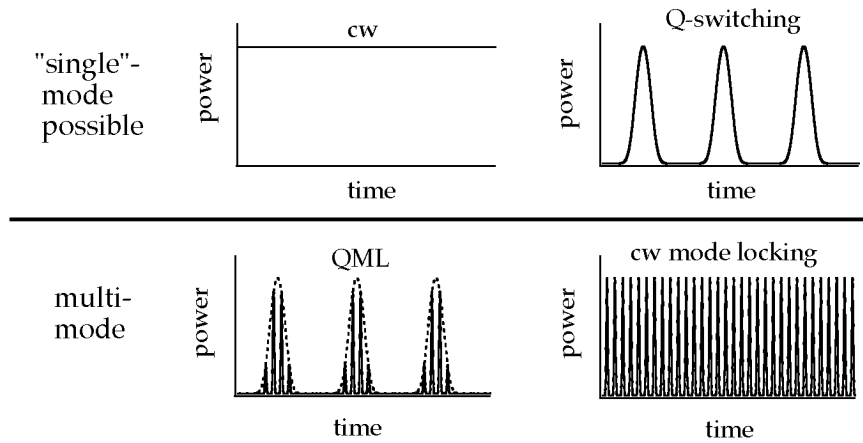
Figure 1.1: Four different temporal regimes of laser operation.

Considering the temporal characteristics of a continuously pumped laser, we distinguish between four different operation regimes: continuous-wave (cw), Q switching, Q–switched mode locking (QML), and cw mode locking (see Figure 1.1). In the cw and the Q-switching regimes, it is possible to operate the laser in a single-longitudinal-mode, which makes them very interesting for spectroscopic or interferometric applications (e.g. in the LIGO[2] project). In the Q-switched mode locking and cw mode locking regimes, the laser output is characterized by trains of short pulses in the picosecond to femtosecond regime with high (Q–switched mode locking) or low (cw mode locking) amplitude fluctuations (see Figure 1.1). Such lasers are interesting for applications that require a high peak power and/or good temporal resolution. In this thesis, we will only deal with lasers operating in the cw mode-locking regime. A good overview over all the four operation regimes can be found in Ref. [4].

Laser light can be very efficiently concentrated in time. Ultrashort light pulses are in most cases generated with passively mode-locked lasers. In this regime of operation, usually a single pulse propagates between mirrors inside a

---

[2] LIGO = light interferometer for gravitational wave observation

laser cavity and generates an output pulse each time it hits a partially reflective mirror (output coupler). A semiconductor saturable absorber mirror (SESAM) allows for the generation of ultrashort pulses as the absorber exhibits lower losses for higher intensities, thus favoring pulsed operation against other regimes such as cw operation. The emitted beam consists of a sequence of pulses separated by the round-trip time of the resonator. Typically the pulse duration is short compared to the resonator round-trip time; therefore the peak power of the pulses is significantly higher than the average power. For example, the round-trip time in the laser presented in Section 3.2.4.2 is 18 ns and the pulse duration 705 fs, resulting in a peak power 22'000 times higher than the average power of the laser.

Applications in nonlinear optics greatly benefit from the high peak powers of such passively mode-locked lasers. However, for a long time, their average output power was limited to a few watts only, a power level that was too low for many applications.

In the first part of the present thesis (Chapter 3), we demonstrate the scaling of the average output power of femtosecond lasers to unprecedented levels of 80 W in femtosecond pulses and 60 W in tunable picosecond pulses. The concept of a passively mode-locked thin disk laser is a combination of the thin disk laser concept [5] (see Section 3.2.1) with a SESAM [6, 7] (see Section 2.2) and turned out to be a power-scalable concept for femtosecond lasers [8]. High average power diffraction limited laser operation is a precondition for passive mode locking. The thinness of the gain material in a thin disk laser combined with large mode areas of pump and laser beams result in a nearly one-dimensional heat flow parallel to the laser propagation direction in the cavity. This way, the thermally induced problems in the gain material that are typical for high power lasers (such as thermal lensing) can be drastically reduced.

The second part of the thesis will concentrate on nonlinear experiments performed with the Yb:YAG thin disk laser as a pump source. A first example is a powerful red-green-blue (RGB) laser system for image projection applications [9, 10]. Laser projectors exhibit significant advantages over conventional lamp projectors. The superposition of three laser beams with a suitable combination of wavelengths in the red, green, and blue spectral region can provide access to

a wide color gamut (see Figure 4.19) and allows excellent color saturation to be achieved. The required projection technology already exists, while the design of a suitable RGB laser source with high output power is still challenging, particularly when additional requirements are introduced, such as long life time, stable maintenance-free long-term operation, compactness and reasonable prize. An interesting approach is to start with a single infrared laser and generate all colors from this in nonlinear conversion stages. We have successfully built a multi-watt RGB laser system based on a high power femtosecond laser and subsequent frequency conversion stages that presents some significant advances in terms of simplicity and practicability (*see* Chapter 4). We in addition carefully analyze this system using advanced numerical methods [11].

Additional examples for nonlinear optical experiments are given in Chapter 5. For the first time, we demonstrate efficient optical parametric generation (OPG) at room temperature (see Section 5.2) directly pumped with a mode-locked thin disk laser. The recent development of high-quality MgO-doped LiTaO$_3$ [12] allow for stable OPG operation without active temperature stabilization. Even higher average powers of the signal and idler waves can be obtained with a *fiber-feedback* optical parametric oscillator (OPO) (see Section 5.3). A *fiber-feedback* OPO is a synchronously pumped high gain OPO with signal feedback through a single mode fiber.

The pulse duration of a mode-locked laser is limited by the emission bandwidth of the laser material. If pulse durations shorter than the duration supported by the material are desired, the optical bandwidth has to be increased with nonlinear effects, such as with nonlinear broadening in a fiber. Pulse compression in a fiber is a well-established technology [13, 14], but has been limited for a long time to average powers in the order of a few watts. Südmeyer et al. [15] applied this technique for the first time at a high average power level in 2003. We report in Section 5.4 on nonlinear pulse compression with even higher average power and shorter pulse duration.

This thesis is organized as follows: In Chapter 2, we shortly review the process of passive mode locking and will address the most important macroscopic parameters of saturable absorbers. Chapter 3 describes the

development of a high average power Yb:YAG thin disk laser and its different setups for the generation of picosecond and femtosecond pulses. In Chapter 4, we present an RGB laser system for the generation of high average output powers in the red, the green and the blue spectral region. The potential of this system, its advantages and possible improvements are analyzed with numerical simulations. Chapter 5 deals with additional nonlinear optical experiments that are pumped with the Yb:YAG laser. A room temperature OPG based on MgO-doped LiTaO$_3$ and a *fiber-feedback* OPO generating high average signal power at 1.5 μm are presented. Finally, we report on nonlinear pulse compression with a large mode area microstructured fiber. The results of this work are summarized in Chapter 6, where also an outlook to future projects is given.

Chapter 2

Passive Mode Locking

In this Chapter, we give a short introduction into three basic passive mode-locking mechanisms and discuss them with respect to the application in compact, diode-pumped solid-state lasers. Then we introduce a special type of saturable absorbers: The semiconductor saturable absorber mirror (SESAMs) [6, 7]. The SESAM provides unique properties to achieve reliable passive mode locking both in the femtosecond and in the picosecond regime. In Section 2.1, we will give a short general overview about mode locking, in particular about passive mode locking. The important absorber parameters, which determine the laser dynamics, will be introduced in Section 2.2. Chapter 2.3 gives a review about the stability limits of continuous-wave passive mode locking, particularly the stability against Q switching.

2.1 Mechanism of passive mode locking

Ultrashort light pulses are generally generated with mode-locked lasers. In this regime of operation, usually a single pulse propagates in the laser cavity. The output pulse is generated each time when the pulse in the cavity hits the output coupler mirror. In the femtosecond regime, the pulses are short compared to the cavity roundtrip time.

In the frequency domain description it is obvious that mode locking cannot be achieved if a significant amount of the laser power is contained in higher

order transverse cavity modes, because they usually have different resonance frequencies. As a consequence a periodic recurrence of constructive addition of all mode amplitudes is not possible. Therefore, laser operation on the fundamental transverse cavity mode (TEM_{00}) is a prerequisite for stable mode locking.

In the time domain, the many phase-locked axial modes result in a short pulse of a duration inversely proportional to the spectral width of all the phase-locked axial modes. Generally, passive mode locking generates shorter pulses and is much simpler than active mode locking. As we are interested in ultrashort laser pulse durations, we limit ourselves to passive mode locking.

Mode locking a laser usually implies the existence of a short time window during a cavity round-trip, in which the net gain is positive (see Figure 2.1). There are three different ways to achieve a short net-gain window, depending on the gain and absorber properties, which are described as follows: Mode locking with a slow saturable absorber [16, 17] (see Figure 2.1a), mode locking with a fast saturable absorber [18, 19] (see Figure 2.1b), and soliton mode locking [20, 21, 22, 23] (see Figure 2.1c).
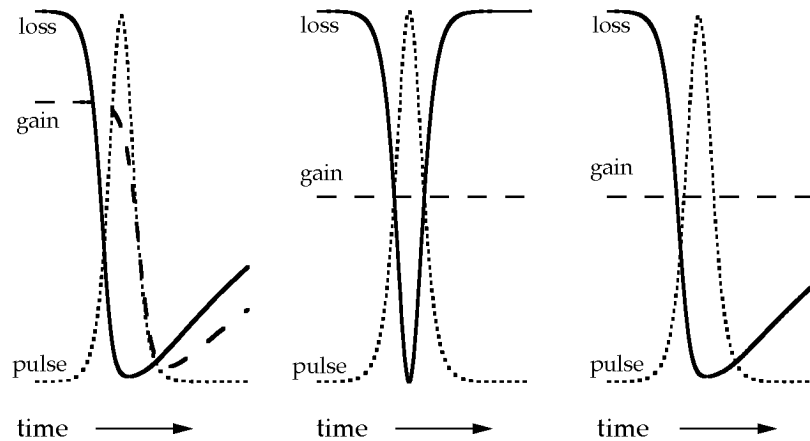
Figure 2.1: Pulse-shaping and stabilization mechanisms owing to gain and loss dynamics in a mode-locked laser in case of using: (a) a slow saturable absorber plus slow gain saturation, (b) a fast saturable absorber, and (c) a slow saturable absorber plus soliton formation.

With a slow saturable absorber ("slow" in this context means "slow compared to the achieved pulse duration but fast compared to the cavity round-trip time"), a short net-gain window can only be obtained in combination with dynamic gain saturation (see Figure 2.1a). This type of mode locking applies to dye lasers [24] or semiconductor lasers [25, 26, 27, 28], which feature a small gain saturation energy. For solid state lasers, the saturation energy of the gain is large compared to typical intra-cavity pulse energies, due to the relatively small laser cross sections. As a consequence, the gain does not saturate during a pulse passage and is fixed at a constant level corresponding to the total cavity loss.

In the fast saturable absorber model, no dynamic gain saturation occurs and the short net-gain window is formed by a fast recovering saturable absorber alone (see Figure 2.1b). This was initially believed to be the only stable approach to passive mode locking of solid-state lasers. Additive pulse mode locking (APM) [29, 30] was the first passively mode locking technique for solid-state lasers. However, APM was not suitable for real world applications, because critical interferometric cavity length stabilization was needed for stable operation. In 1991, a breakthrough in passively mode-locked solid-state lasers was initiated by the discovery of Kerr lens mode locking (KLM) [31, 32, 33]. KLM was the first demonstration of a simple and reliable intra-cavity mode locking technique for solid-state lasers. Because of its simplicity, KLM replaced the more complicated coupled cavity mode locking techniques. With this technique, pulses as short as $\approx$ 5.8 fs have been demonstrated [34, 35]. These are the shortest pulses ever produced directly from a laser oscillator.

Besides the tremendous success of KLM, there are some significant limitations for practical or "real-world" ultrashort lasers. The fast saturable absorber process in KLM is based on self-focusing inside the laser crystal emerging at high intensities. To enhance self-focusing the laser is usually operated close to the stability limit, so that the cavity is sensitive to small additional intra-cavity lensing effects. Furthermore, lasers generating ultrashort pulses based on the fast saturable absorber approach alone have an intrinsic problem: They do not self-start from continuous-wave (cw) – operation.

If we desire to obtain pulse durations in the femtosecond to a few picosecond regime without having to cope with the disadvantages of KLM, we normally have to resort to slow saturable absorbers. Slow absorbers take significantly longer to recover compared to the pulse duration. Consequently, there exists a window of positive net gain behind the trailing edge of the pulse (Figure 2.1c). One might expect that this situation is unstable because noise may grow after the pulse, or the pulse gets longer due to continuous amplification of the trailing edge. Indeed mode locking with a slow saturable absorber can only be explained by means of additional stabilizing effects.
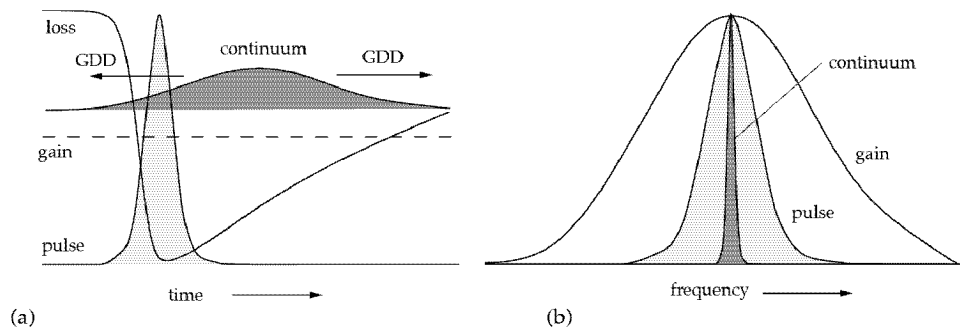
Figure 2.2: Soliton mode locking in (a) time and (b) frequency domain. The continuum spreads in time owing to group delay dispersion (GDD) and therefore, suffers from higher losses in the absorber, which is saturated by the shorter soliton pulse (a). However, the longer continuum pulse has a narrower spectrum and thus experiences higher gain than the spectrally broader soliton pulse (b).

Soliton mode locking can be qualitatively explained as follows (see Figure 2.2): The soliton pulse loses energy due to gain filtering (i.e. due to the limited gain bandwidth) and other cavity losses. These losses favor a long, low intensity background pulse, the so-called continuum, which experiences negligible bandwidth broadening from self phase modulation (SPM), but spreads in time due to GDD (see Figure 2.2a). Compared to the soliton pulse, the longer continuum has a narrower spectrum (see Figure 2.2b), which leads to a weaker gain filter and a higher effective gain. Without a suitable intra-cavity saturable absorber, the continuum would actually grow until it reaches the lasing threshold and thus ultimately would destabilize the soliton pulse.

However, introducing a saturable absorber that is fast enough to introduce sufficient loss for the growing and temporally spreading continuum to prevent it from reaching the lasing threshold can stabilize the soliton. The net gain window can be more than 100 times longer than the pulse duration before mode locking becomes unstable. This effect is particularly important at strong saturation of the absorber. A detailed theoretical treatment of soliton mode locking based on soliton perturbation theory can be found in Ref. [21]. The Yb:YAG laser described in this thesis is operated in the soliton mode locking regime.

An example for a saturable absorber is a semiconductor saturable absorber mirror (SESAM) [6, 7], which provide unique freedom in the design of important absorber parameters such as the saturation fluence or the recovery time (see Chapter 2.2). This flexibility in SESAM design made possible to obtain compact and reliable passively mode-locked lasers in the picosecond and femtosecond regime. In the picosecond regime, we use the SESAM in the fast saturable absorber regime (see Figure 2.1b). For femtosecond pulse generation, we operate the laser in the soliton mode-locked regime and use the SESAM to start and stabilize the mode locking process (see Figure 2.1c).

2.2 Semiconductor saturable absorber mirror

In this Chapter, we will give a short overview over the basic mode of operation of SESAMs, and briefly discuss the important absorber parameters that determine the mode locking dynamics. For a more detailed description of semiconductor saturable absorber mirrors (SESAMs), please refer to Refs. [6, 7, 36, 37].

2.2.1 Principle of operation

Semiconductors show a nonlinear reflectivity upon incidence of radiation due to absorption bleaching at high intensities. This makes them suitable in principle as a saturable absorber, i.e., as a device that shows higher reflection at high intensities/fluences, which favors the pulsed mode of operation over

continuous-wave operation. The bandgap of a semiconductor can be tailored to the desired laser wavelength. The response time (see Chapter 2.2.3) can be influenced by the growth temperature of the absorber, which determines the defect density in the bandgap. In addition, a semiconductor is a compact, passive device that does not need electrical control and can be fabricated by standard epitaxial growth techniques. Therefore, a semiconductor provides the basic features to passively mode-lock a solid-state laser.

2.2.2 SESAM structure

The SESAM consists of one or several absorber layers and non-absorbing spacer layers, which are integrated into a Fabry-Perot structure. The Fabry-Perot is formed by an epitaxially grown bottom mirror (of typically 25-30 quarter-wave layers of high and low index of refraction) and in the case of a low finesse device, the Fresnel reflection at the semiconductor air interface ($\approx 30\%$). High finesse devices have an additional dielectric or semiconductor coating on top with a custom designed reflectivity. The thickness of the Fabry-Perot structure is usually adjusted for antiresonance at the laser wavelength to avoid significant temperature dependence and optical bistability. The antiresonant design also leads to a flat and negligible group delay dispersion (GDD) around the laser wavelength. Figure 2.3 shows the structure of an antiresonant low-finesse SESAM, together with the standing-wave pattern of the optical field intensity inside this structure.
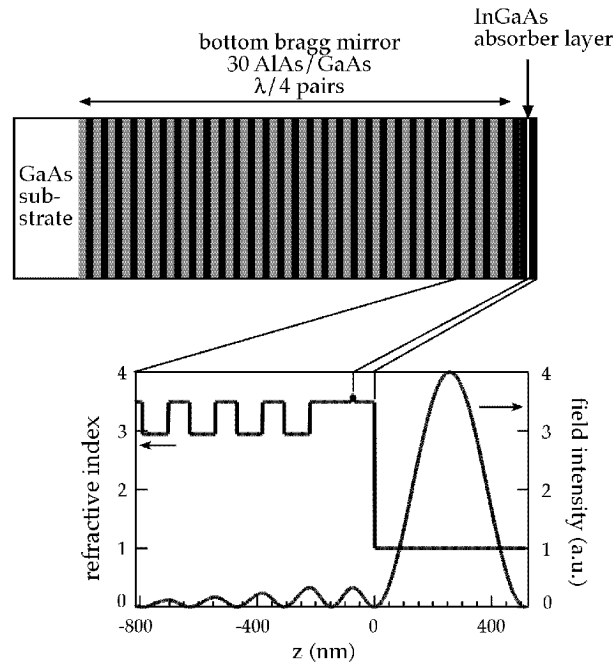
Figure 2.3:   Schematic structure of a low-finesse SESAM together with the standing-wave intensity pattern.

The typical InGaAs absorber layer thickness lies between 4 nm and 25 nm. In this range, the absorber forms a quantum mechanical potential well. The bandgap energy in the absorber region is determined by the energy difference of the highest states in the valence and lowest states in the conduction band and the material composition.

2.2.3 Macroscopic properties

The dynamics of a passively mode-locked laser are determined by the macroscopic properties of the SESAM. Figure 2.4 shows the typical nonlinear response of a SESAM as a function of the incident pulse fluence on the device. The maximum change in reflectivity is called modulation depth ΔR, which can be designed by the absorber thickness up to a certain amount. The amount of fluence, which is required to saturate $1/e$ of the modulation depth of an infinitesimal thin absorber layer, is named saturation fluence $F_{A, sat}$. Another important parameter are the nonsaturable losses ΔR_{ns}; they describe the losses introduced by the SESAM if it is fully saturated. The maximum achievable

reflectivity is called R_{ns}. Together with recovery behavior of the SESAM (see Figure 2.5) these parameters fully characterize such a device.
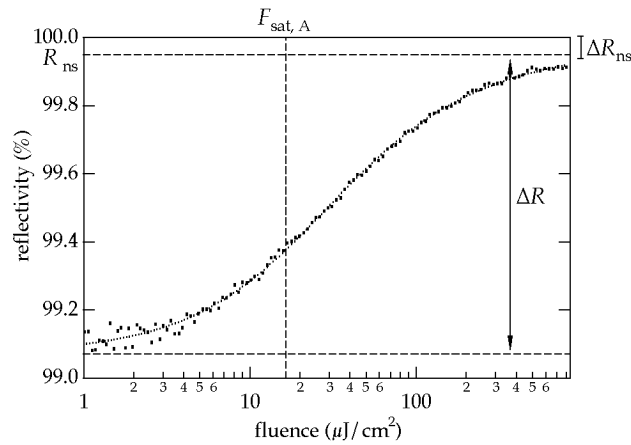
Figure 2.4: Measured change in reflectivity versus incident pulse fluence (dots) and theoretical fit (solid curve) for the SESAM depicted in Figure 2.3, measured with an Yb:YAG laser at a wavelength of 1030 nm.

Semiconductor saturable absorber mirrors (SESAMs) [6, 7] have been proved to be an excellent tool for passive mode locking and Q switching of a large variety of solid-state lasers. The reasons for this breakthrough are mainly that the main SESAM parameters can be designed over a wide range to achieve the best performance of the passively mode-locked or Q-switched laser in its desired operation mode. Thus, a precise control of the nonlinearity of the SESAM is achieved.

Carrier dynamics determines the impulse response of a SESAM. SESAMs typically show a bitemporal impulse response (see Figure 2.5). The fast component arises from intraband thermalization (carrier-carrier scattering) and cooling (carrier-phonon scattering) and lies typically between 50 fs and 200 fs. The slow component originates from trapping and carrier recombination and is typically of the order of tens to hundreds of picosecond.

The response time can be varied by the growth temperature of the SESAM. With low temperature (LT) growth, the number of traps can be enhanced,

which leads to a faster decay of the excited carriers, at the expense of increased nonsaturable losses. These losses are caused by various reasons such as clusters, defects, and surface effects. It has been shown, however, that a suitable annealing procedure [38] or doping of the semiconductor with beryllium [39] can help to obtain a fast recovery time and low nonsaturable losses simultaneously. The LT growth also helps to prevent surface striations due to the lattice mismatch.

The bitemporal response is important for passive mode locking. The slow component helps to initiate mode locking, while the fast time constant contributes to pulse shortening.
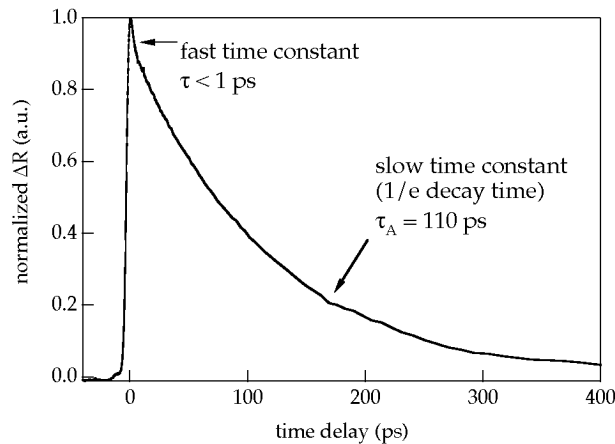
Figure 2.5:   Bitemporal impulse response of the SESAM shown in Figure 2.3 measured with an Yb:YAG laser at a wavelength of 1030 nm.

2.3 Stability limits of continuous-wave passive mode locking

The usually desired mode of operation of the laser is continuous-wave (cw) mode locking, where a train of pulses with constant duration, energy, and shape is generated. However, under certain conditions, the use of saturable absorbers may also lead to Q-switched mode locking (QML) (see Figure 1.1). In this case the laser emits bunches of mode-locked pulses, which may or may not

have a stable Q-switching envelope. The main challenge in passively mode-locked solid-state lasers is to overcome the tendency of the laser towards QML.

2.3.1 Q-switching instabilities

The regime of QML operation is usually unwanted as these oscillations lead to substantially higher peak powers near the maximum of the Q-switch envelope than in continuous mode-locked operation, where the pulse energy remains constant. The higher peak powers in QML can lead to damage of cavity elements, in particular of the saturable absorber. QML is a consequence of the lower absorption of a saturable absorber at higher pulse energies and therefore the reduced damping of the gain relaxation oscillations. There exists a threshold for the intra-cavity pulse energy E_p, above which stable cw mode locking is achieved in lasers without soliton mode locking. This threshold (see Ref. [40]) is given by the expression

$$E_p^{\;2} > E_{sat,L} \cdot E_{sat,A} \cdot \Delta R \tag{2.1}$$

Here, E_p is the intra-cavity pulse energy,

$$E_{sat,L} = \frac{hv \cdot A_L}{m \cdot \left(\sigma_{em,L} + \sigma_{abs,L} \right)} \tag{2.2}$$

$E_{sat,L}$ is the effective saturation energy of the laser medium, and A_L is the mode area in the laser medium. m is the number of passes through the gain medium per cavity round-trip. $\sigma_{em,L}$ and $\sigma_{abs,L}$ are emission and absorption cross sections at the laser wavelength and ΔR is the modulation depth of the absorber (see Section 2.2.3). Soliton formation has an additional stabilizing effect against QML. This can be understood by taking into account the coupling between pulse energy and spectral bandwidth via SPM (see Section 2.1). Please refer to Ref. [40] for further details. From Equation (2.1) we can derive guidelines that have to be fulfilled to reduce the tendency towards QML:

- Use a gain medium with small saturation fluence and optimize the pumping arrangement for a small mode area in the gain medium.

- Minimize the cavity losses so that a high intra-cavity pulse energy can be achieved.

- Operate the saturable absorber in the regime of strong saturation. Here SESAMs provide an exceptional amount of freedom, as the parameters can be custom designed in a broad range.

- Do not use a larger modulation depth than necessary.

- Use a cavity with a low repetition rate.

At a first glance, these seem to be rather straightforward guidelines. However, most of the above points have trade-offs in terms of efficiency and practicability or are detrimental with respect to other instabilities. We will address the challenges in fulfilling all the requirements for successful mode locking of high average power thin disk lasers more extensively in Section 3.1.

Chapter 3

High Average Power Passively Mode-Locked Yb:YAG Thin Disk Laser

The interest in the field of diode-pumped passively mode-locked solid-state lasers with high average output power is growing every year. An increasing number of applications in various fields (e.g. medicine, material processing, lithography and entertainment) benefit from the short pulse duration in combination with good transverse beam quality. Especially applications involving nonlinear effects greatly benefit from their high pulse energies and peak powers. An alternative way for reaching tens of watts of average power in ultrashort pulses is to amplify a mode-locked seed laser in multiple additional amplification stages [41, 42, 43]. However, for reasons of simplicity and compactness, it is advantageous to generate the pulses directly out of a mode-locked oscillator.

In this Chapter, we present a survey of different setups of an Yb:YAG thin disk laser. Section 3.1 addresses some challenges that have to be overcome to reach high average power in femtosecond pulses, for example thermal aberrations in the laser medium, mode locking instabilities, and damage in optical components. In Section 3.2.1 and 3.2.2, respectively, we briefly review the concept of a thin disk laser passively mode-locked with a semiconductor saturable absorber mirror (SESAM). This concept turns out to be power-

scalable, which arises from the special geometry of the gain medium and the absorber. Section 3.2 reviews the different setups of the Yb:YAG thin disk laser for the generation of 60 W average power in tunable 6-24 picosecond pulses at a pulse repetition rate of 34 MHz (see Section 3.2.3) and with up to 80 W of average power in 705 fs at a pulse repetition rate of 57 MHz (see Sections 3.2.4.1 and 3.2.4.2). In Section 3.3, we briefly address the challenges for scaling to higher average output powers and higher pulse energies.

3.1 Challenges for high average power femtosecond lasers

The development of lasers with very high average output power in femtosecond pulses requires a careful inspection of several topics, e.g. the problem of thermal lensing in the gain medium, the prevention from mode locking instabilities and the choice of the optimal gain material for the desired operation regime. These topics will be addressed in the following sections.

3.1.1 Degradation of the transverse beam quality

One of the most severe challenges for the development of high average power femtosecond lasers is the requirement of a nearly diffraction-limited transverse beam quality (TEM_{00}), because higher order transverse modes strongly disturb the mode locking process. Therefore, these lasers rely on the development of continuous-wave (cw) lasers with excellent transverse beam quality. For quite some time, the cw output power obtained in TEM_{00} mode was limited to about 100 W [44]. Recently, however, 1.36 kW of output power in a nearly diffraction-limited beam has been reported in a fiber laser [45].

In high average power lasers, the thermal load in the cavity components becomes strong, in particular in the gain medium, where a substantial amount of the pump power is converted into heat. In solid-state lasers (at least in high quality laser gain media), the primary source of heating is the quantum defect, which is defined as the fraction of energy, which is lost, when each pump photon is converted into a laser photon. There may also be non-radiative

relaxation processes, for example due to parasitic losses, exited-state absorption, upconversion, and quenching (see e.g. Ref. [46] and [47]). Thus, laser materials with a low quantum defect are expected to produce less heat as long as the parasitic losses are week. The generated heat causes a thermal gradient, which leads to wavefront distortions due to the deformation of the surfaces of the optical component or due to the thermo-optical effect [47, 48]. Unfortunately, the resulting thermal lenses usually exhibit strong aberrations, which can severely degrade the transverse laser beam quality.

There are a number of measures that can be taken in order to maintain TEM_{00} operation even at very high average powers:

- Reduction of the thermal load by choosing a gain material with a low quantum defect (in general 3-level or quasi-3-level systems, see Section 3.1.3) and intra-cavity components with low absorption.

- Reduction of the thermal gradients by choosing a beneficial geometry and cooling configuration with a large ratio of cooling surface to heated volume. This condition is fulfilled particularly nicely in fiber lasers, slab lasers, and thin disk lasers (see Section 3.2.1).

- Reduction of the thermal lensing effects for a given temperature distribution by choosing a material with small coefficients of thermal refractive index change (dn/dT) and thermal expansion $(L^{-1}dL/dT)$.

- Beam propagation parallel to the temperature gradient. The thermal lens is mostly affected by the transversal component of the thermal gradient. Therefore it is advantageous to have a nearly one-dimensional heat flow within the volume of the laser mode and here again, the thin disk laser concept provides an excellent solution (see Section 3.2.1).

3.1.2 Mode locking instabilities in high average power lasers

The discussion of the stability limits of continuous-wave passive mode locking in Section 2.3 is also valid for high-average output powers obtained for example with the thin disk laser concept (see Section 3.2.2). If the mode areas in the gain material and on the saturable absorber are scaled by the same factor as the intra-cavity power, the values for Q-switching instabilities do not change.

3.1.3 Choice of gain material

For the generation of high average power femtosecond laser pulses the choice of the gain material is a very important issue. In this Section the most important parameters for high power operation will be reviewed very briefly.

There are several requirements for gain materials to obtain high average power in ultrashort pulses. It should exhibit:

a. a broad gain bandwidth that supports femtosecond pulses,

b. a large emission cross section (see Section 2.3.1),

c. a high thermal conductivity (see Section 3.1.1),

d. a low quantum defect (see Section 3.1.1),

e. an absorption band for which high power, high-brightness laser diodes are available.

Besides the properties listed above, there are other benefits such as the absence of parasitic losses (e.g. upconversion [46], quenching [49] or exited-state absorption [47]) for a good efficiency and a large product of emission cross section and fluorescence life time resulting in a low laser threshold. However, it is difficult to find a laser material, which combines all those properties. Usually, there is a trade-off between a broad gain bandwidth, a large cross section and a good thermal conductivity.

One of the most suitable dopants for high power femtosecond lasers is ytterbium (Yb^{3+}) [50, 51]. It has a very simple energy level scheme with only two manifolds participating in the lasing process. Other energy levels lie far above the ground state, such that parasitic processes like upconversion [46] or excited-state absorption [47] are absent. The pump wavelength (λ_P) for Yb^{3+}–doped materials lies between 0.9 μm and 1.1 μm, a range for which high power InGaAs diode lasers are available. The quantum defect ($1-\lambda_P/\lambda_L$) of Yb^{3+}–doped materials is generally low: values as small as 1.6% have been reported in Yb:KYW [52] and the value for Yb:YAG pumped at 940 nm is 8.5%.

The gain material used in this thesis is Yb^{3+}:$Y_3Al_5O_{12}$ (Yb:YAG) because of its excellent thermal and mechanical properties. Figure 3.1 shows the

absorption and emission spectra of Yb:YAG, and the physical properties of Yb:YAG are summarized in Table 3.1.
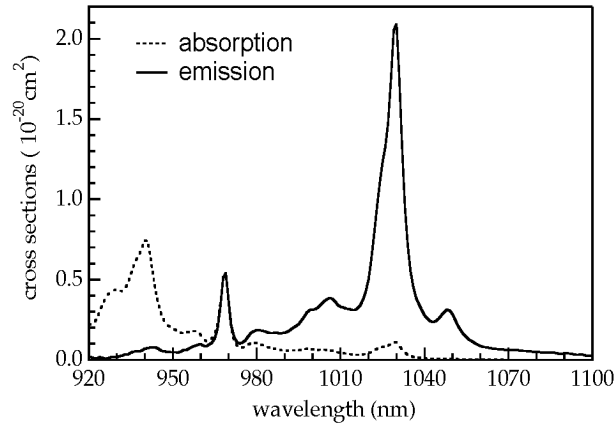
Figure 3.1: Absorption (dotted line) and emission (solid line) cross section of Yb:YAG.

The achievable pulse duration with Yb:YAG is on the order of several hundred femtoseconds. For pulse durations well below that, other gain materials as for example $Yb^{3+}:KGd(WO_4)_2/$ $KY(WO_4)_2$ (Yb:KGW/KYW) have to be used. With the choice of Yb:KYW as gain material, pulses a short as 240 fs at 22 W of average output power have been demonstrated from a passively mode locked thin disk laser [53]. Although Yb:YAG as well as Yb:KYW are very suitable materials for high average power femtosecond lasers, they still have disadvantages concerning thermal properties. They may be overcome by new gain materials as for example by the recently presented Yb^{3+}-doped sesquioxides $Yb:Sc_2O_3$ [54] and $Yb:Lu_2O_3$ [55]. They exhibit the highest thermal conductivity of all known Yb-doped laser materials and appear to be very promising for high power femtosecond laser operation.

Laser properties	Units	Yb:YAG
laser wavelength λ_L	μm	1.03 [a)]
emission bandwidth $\Delta\lambda$	nm	≈ 6.3 [a)]
emission cross section σ^L_{em}	10^{-20} cm^2	2.1 [a)]
pump wavelength λ_P	nm	940 [a)]
absorption cross section σ^P_{abs}	10^{-19} cm^2	0.01 [a)]
fluorescence lifetime τ_{rad}	μs	≈ 950 [a)]
transparency intensity I_{trans}	kW/cm^2	1.4 [a)]

Optical properties	Units	Yb:YAG
refractive index at λ_L	-	1.82 [a)]
temperature coefficient of refractive index dn/dT	10^{-6} K^{-1}	7.3 [b)]
nonlinear refractive index n_2	10^{-16} cm^2/W	6.2 [d)] (undoped)

Thermal properties	Units	Yb:YAG
thermal conductivity K (25 °C)	W/m·K	undoped: 14 [b)] 10% doped: 6 [c)]
coefficient of linear thermal expansion α_T (20 °C to 40 °C)	10^{-6} K^{-1}	7.5 [b)]

Table 3.1: Properties of Yb:YAG. Data were taken from the following references: [a)] [56], [b)] [47], [c)] [57], [d)] [58].

3.1.4 Cavity design

The design of the laser cavity is a crucial aspect for building high average power femtosecond lasers. Several conditions have to be fulfilled in order to achieve stable laser operation with femtosecond pulse durations and high average output power.

First of all, appropriate mode areas on the gain medium and the semiconductor saturable absorber mirror (SESAM) are required to prevent the laser from Q–switching instabilities (see Section 2.3.1). However, the scaling law for passively mode-locked thin disk lasers to achieve high average power demands large mode areas on both, the thin disk as well as on the SESAM (see

Section 3.2.2). In order to prevent the sensitive intra-cavity components (such as dispersive mirrors) from optical damage, the design has to be adjusted so that those components can be operated at relatively low peak intensities. Note that the SESAM is not the limiting component, as with an appropriate mode area the intensity on the SESAM is in the same range as in low power lasers.

For an optimal laser performance at the expected maximum power, the power dependant thermal lenses in the intra-cavity components have to be taken into account. Since the heat flow in the gain material and in the SESAM (see Section 3.2.2) is nearly one-dimensional, thermal lensing in those components is relatively weak. In contrast, we encountered strong thermal effects in the dispersive mirrors. Operating the dispersive mirrors at positions with large mode areas can reduce thermal lensing. A laser cavity with larger beams, however, also is more sensitive to even small perturbations.

An important precondition for stable passive mode-locking operation is that the laser operates in a fundamental transverse mode. As shown by Magni et al. [59], there exist two stability zones in a laser resonator containing a thermal lens, known as zone I and zone II. These zones are functions of the dioptric power of this lens. It is advantageous to operate the laser resonator in the stability zone I where the misalignment sensitivity of the cavity is much smaller than in zone II. In addition, it is desirable to have the laser operation point at the minimum of this stability zone where the laser mode radius is minimal and hardly changes with the dioptric power of the thermal lens (e.g. by increasing the pump power). The width of the stability zone is inverse proportional to the laser beam radius squared [59]. Therefore the thermal lens has to be known more precisely for large laser beam radii.

3.1.5 Dispersion compensation

Another crucial issue of a passively mode-locked high power thin disk laser is dispersion compensation. Stable soliton formation [21, 22, 60] in a mode-locked laser requires a certain amount of nonlinear phase shift in the cavity, which in a thin disk laser is mostly provided by the Brewster plate. Increasing the average output power of a mode-locked laser also increases its pulse energy. In order to

fulfill the equation for stable soliton pulses (see Equation (3.1)), the amount of group delay dispersion (GDD) has to be increased. The pulse duration in a soliton mode-locked laser is determined by Equation (3.1), where D is the amount GDD per cavity round-trip, γ_{SPM} is the nonlinear coefficient of self phase modulation (SPM) and E_p the intra cavity pulse energy.

$$\tau_{FWHM} \approx 1.76 \cdot \frac{2|D|}{|\gamma_{SPM}|E_p} \qquad (3.1)$$

The use of a prism pair is no longer a good solution, as this would require a large prism separation in order to generate the required GDD. Lasers for high power applications would require a prism material with a good thermal conductivity such as fused silica. With this material, a prism separation of 9.6 m would be needed for the generation of $-12'000$ fs^2 per cavity round-trip. One way to avoid such long prism separations would be to use a single prism in the intersection point of the cavity [61], but this wouldn't avoid thermal problems in the prism at high power levels of several tens of watts.

Another possibility for the dispersion compensation in mode-locked lasers is to use a Gires-Tournois interferometer (GTI) [62]. A GTI, however, is typically used for pulse durations above 100 fs, as its bandwidth is limited. Mode-locked thin disk lasers with output powers in the order of 20 W have been successfully mode-locked with a GTI [8, 63]. At higher average powers, however, a small curvature in the AR-coated substrate of the GTI can occur and this destroys the interference between the substrate and the high reflective mirror (see Section 3.2.3).

To overcome the drawbacks of prisms and GTIs for dispersion compensation in high average power femtosecond lasers, dielectric dispersive mirrors with a fixed amount of negative GDD per bounce can be used. Best laser performance of the femtosecond Yb:YAG thin disk laser (see Section 3.2.4.2) has been achieved with dispersive mirrors that have been optimized for small absorption and thus for weak thermal effects. However, in order to obtain the shortest soliton pulse durations, it's necessary to be able to fine-tune either the GDD or the SPM. Therefore, we operate a Brewster plate in an arm of the laser cavity, where the laser mode radius changes along the laser

propagation direction (see Figure 3.7). In this way, we can adjust the SPM by moving the Brewster plate to positions with a larger or smaller beam radius.

To summarize: the realization of a mode-locked thin disk laser with femtosecond pulse duration and very high average power in the order of several tens of watts requires a carefully designed cavity that simultaneously fulfills the requirements for single-transverse mode operation at high power, the boundary conditions for mode locking and which minimizes the thermal problems in the different intra-cavity components. Careful experimental optimization results in the optimal performance of the laser at the highest power levels.

3.2 Thin disk Yb:YAG laser

The first passively mode-locked Yb:YAG thin disk laser has been demonstrated by Aus der Au et al. in 2000 [8] with an average output power of 16.2 W in 730–fs pulses. The gain medium in a thin disk laser is used in reflection. Therefore, the laser beam always generates a standing-wave pattern in the disk, regardless of the type of the laser cavity (ring or standing-wave). As a consequence, spatial hole burning (SHB) is unavoidable [64]. This has a strong effect on the mode locking performance because it leads to inhomogeneous gain saturation. Therefore stable mode locking in an Yb:YAG thin disk laser is only possible in a relatively narrow band of pulse durations around 700 fs. As SHB determines the pulse duration in a thin disk laser, we first concentrate on the power scalability. Further reduction of the pulse duration down to 24-fs with 32 W of average power by external nonlinear pulse compression in a microstructured fiber will be addressed in Section 5.4.

3.2.1 Concept of a thin disk laser

A major challenge in scaling the average power of passively mode-locked lasers is to cope with the effects that are induced by the high thermal load (see Section 3.1). The geometry of the laser material and cooling configuration are crucial for the design of any high power laser for passive mode locking. The

thin disk laser head [5, 65] is a very successful concept suitable for diffraction-limited laser operation at high average output power. The gain material in the laser head has the shape of a very thin disk, which is mounted with one end face onto a heat sink. The cooled face of the disk is coated for high reflectivity (HR) at the laser and pump wavelength, while the other side has an antireflection (AR) coating for both wavelengths.

As the diameter of the pump beam is large compared to the thickness of the disk, the heat flux is nearly one-dimensional and directed along the optical axis of the laser. This leads to a nearly homogenous temperature profile within the pumped region in radial direction and thus to only weak thermal lensing and low stress-induced birefringence. Aberrations due to the thermal lens are confined to the border region of the pumped volume.

In all the experiments presented in this thesis, we used a thin disk laser head constructed by the company TRUMPF-Laser GmbH in Schramberg, Germany. The laser head contained a 100-μm thin Yb:YAG disk with a doping level of $\approx$10%. The disk is slightly wedged in order to eliminate effects from residual reflections from the AR coating. The reflecting face is directly attached to a cooling finger. We pump the Yb:YAG disk with up to 370 W at 940 nm from diode bars. The pump optic is aligned for 16 passes (i.e., 8 double passes) through the disk in order to ensure efficient pump absorption despite the small thickness of the disk (see Figure 3.2) [66]. The absorption length of the gain material is typically $\approx$1 mm. The diameter of the pump spot is $\approx$2.8 mm. Since the pump diameter is much larger than the thickness of the disk, the thermal lensing effect is weak with an estimated focusing power of < 0.3 m^{-1}.

Because of the high number of passes of the pump radiation through the gain material, a very high pump power density is obtained. This is beneficial for quasi-3-level laser mediums like Yb:YAG crystals emitting at the 1030-nm transition. This leads to a high inversion level and reduces the reabsorption losses [67]. The absorption wavelength for this transition is centered at 940 nm or 970 nm (see Figure 3.1), respectively, where high average power laser diode arrays are commercially available. The low quantum defect results in a good pump efficiency and low thermal load in the gain medium.
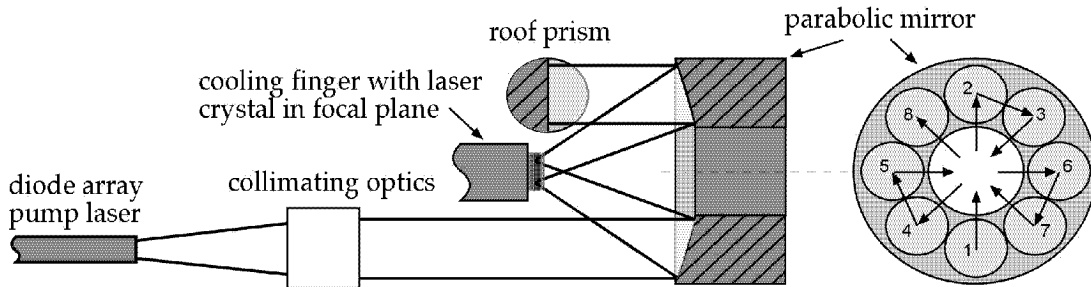
Figure 3.2:   Setup of the Yb:YAG thin disk laser head. The pump optics allows
              for 16 passes of the pump radiation through the gain material by
              using a parabolic mirror and a number of roof prisms.

However, the concept of a thin disk laser seems to be applicable only to a limited number of gain materials possessing a good thermal conductivity, a small quantum defect, a large product of upper-state lifetime and emission cross section. If these conditions are not fulfilled, the temperature rise and temperature gradient become too strong. Although Nd:YAG has been used as a gain material for thin disk lasers [68], it was less successful than Yb:YAG [69] because of its higher quantum defect. Until now, the most suitable material for very short pulses applicable in the thin disk laser concept is Yb:KYW [53], while other broadband gain materials such as Nd:glass or Ti:sapphire seem not to be suitable. Next to the above-mentioned properties, the gain crystal should exhibit the potential for high doping densities to reduce the number of pump passes through the gain material.

3.2.2 Concept of mode-locked thin disk lasers

The thin disk laser in combination with a semiconductor saturable absorber mirror (SESAM) is very well suited for passive mode locking. Such a laser generates stable and reliable (see Section 2.2) pulse trains with tens of watts of average output power in picosecond (see Section 3.2.3) and sub-picosecond pulses (see Section 3.2.4) in a diffraction-limited beam.

A crucial feature of the thin disk concept is power scalability, which arises from the special geometry of gain medium and saturable absorber. Doubling the mode areas on thin disk and the SESAM while doubling the pump power doubles the average output power of a mode-locked thin disk laser. The heat

flow on the SESAM is similar to the gain medium nearly one-dimensional because the thickness of the substrate is very small compared to the laser beam diameter. Not only the thermal situation remains the same, but also the intensities incident on the gain medium and the absorber remain unchanged. As a result of this behavior, neither the absorption nor the saturation of the gain and the SESAM are modified, and therefore the tendency towards QML (see Section 2.3.1) also remains unchanged.

In the following Sections we present different Yb:YAG thin disk lasers. One thin disk laser configuration is optimized for the generation of tunable pulses from 6-24 ps with 60 W of average output power (see Section 3.2.3) and two configurations for the generation of femtosecond pulses, one with a pulse repetition rate of 34 MHz (see Section 3.2.4.1) and another with higher pulse repetition rate of 57 MHz (see Section 3.2.4.2). In all those configurations, we used the same thin disk laser head described in Section 3.2.1.

3.2.3 Picosecond Yb:YAG laser

In the picosecond laser, a self-made Gires-Tournois interferometer [62] (GTI) is used for the dispersion compensation. The GTI consists of a fused-silica plate and a high reflector. With a change of the air gap between the substrate and the high reflector with a piezo, the amount of group delay dispersion (GDD) can be adjusted from highly negative to highly positive values. The fused-silica substrate of the GTI is AR-coated on one side. With a simple cavity for continuous-wave operation we obtained 103 W of output power with an excellent beam quality, with a measured M^2-factor of 1.05. The laser cavity for mode locking (see Figure 3.3) contains a number of dielectric high reflectors (HR) on fused-silica substrates (for reduced thermal effects), a 1.2–mm thick Brewster plate for linear laser polarization and a circular aperture for mode selection. We used a 60 μm thick etalon to restrict the bandwidth in order to obtain stable picosecond pulses. Without the etalon, we have observed a tendency for double pulsing in this operation regime, which is probably related to spatial hole burning [64].

The SESAM [6, 7] used for the passive mode locking process was grown with metal organic chemical vapor deposition (MOCVD) and contains a 10 nm thick InGaAs absorber in a standard low-finesse design. The calculated laser mode radius is ≈ 1.14 mm on the thin disk and ≈ 0.84 mm on the SESAM. The transmission of the output coupler is 4.7%.

With the cavity shown in Figure 3.3, we achieve an average power of 56-60 W at 1030 nm at a pulse repetition rate of 34 MHz. The FWHM pulse duration is tunable (by variation of the GDD with the GTI) between 5.6 ps and 23.8 ps (see Figure 3.4) [70]. The GTI substrate has a thickness of 2 mm and the air gap is estimated to be ≈ 78 μm for the shortest pulses, corresponding to a GDD of -86'000 fs^2. The pulse energy of these pulses is 1.7 μJ corresponding to a peak power of 270 kW.
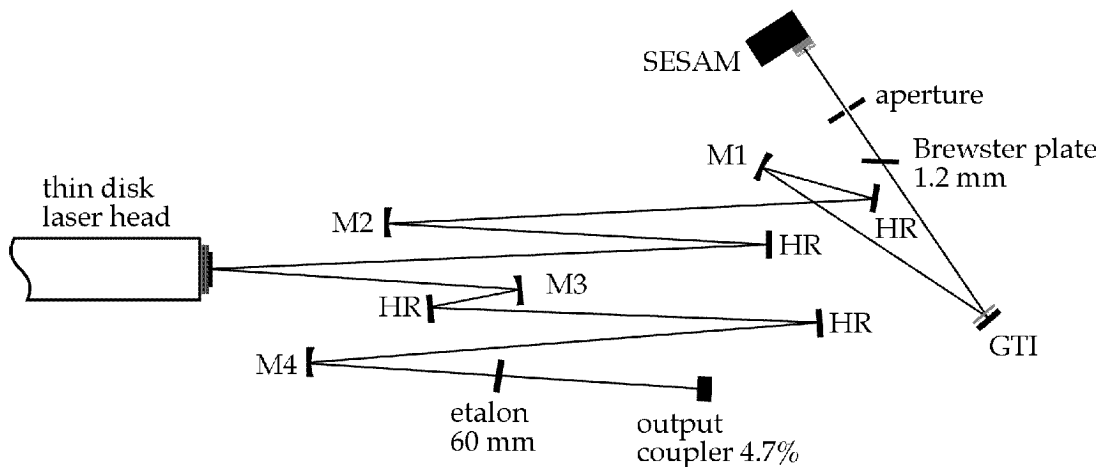
Figure3.3:   Setup of the picosecond Yb:YAG thin disk laser. $M1$-$M4$, spherically curved mirrors; HR, high reflectors; SESAM, semiconductor saturable absorber mirror; GTI, Gires-Tournois Interferometer.

Q-switching instabilities [40] are nicely suppressed (see Section 2.3.1). The weak sidebands in the radio-frequency spectrum are about 40 dB below the carrier, corresponding to fluctuations of the pulse energy by only a few percent. These fluctuations are most probably related to thermal effects in the GTI that caused a small curvature of the substrate.
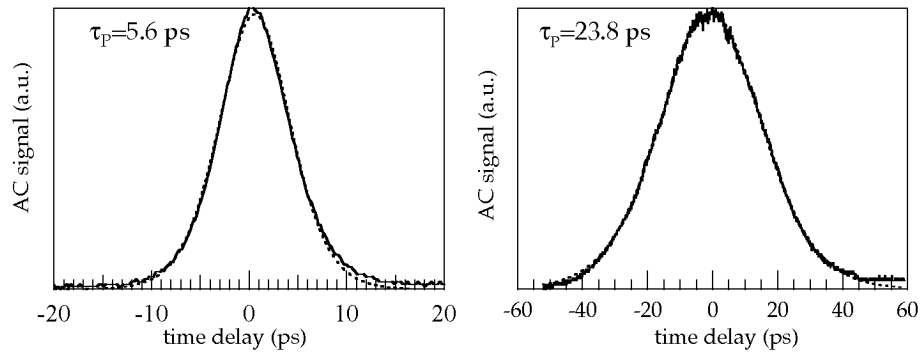
Figure 3.4: Autocorrelation of the 6 ps (left) and the 24 ps (right) pulses from the Yb:YAG thin disk laser. The dashed lines (representing $sech^2$–fits) overlap the data well.

In order to improve the stability of the mode-locked laser and to reduce the pulse duration to femtosecond pulses, we decided to change the way of dispersion compensation. The following laser designs (see Section 3.2.4) are based on dispersive mirrors for the generation of negative GDD instead of using a GTI to avoid such pulse energy fluctuations, as those disturb nonlinear experiments that are pumped with the femtosecond Yb:YAG thin disk laser (see Chapter 4 and Chapter 5).

3.2.4 Femtosecond Yb:YAG laser

The dispersion compensation to achieve femtosecond pulses with an Yb:YAG thin disk laser is based on dispersive mirrors, which introduce a fixed amount of negative GDD per bounce. Mode locking with femtosecond pulse duration is obtained with two different designs. The first design has a pulse repetition rate of 34 MHz, where we achieve stable mode locking with 60 W of average output power and a pulse duration of 810 fs. The second laser was designed for a higher pulse repetition rate of 57 MHz and we achieve even higher output powers of up to 80 W in 705 fs pulses.

3.2.4.1 60-W setup with 34-MHz repetition rate

In this Section we review the thin disk Yb:YAG laser operating at a pulse repetition rate of 34 MHz. The saturation fluence and modulation depth of the

SESAM were measured to be 20 µJ/cm^2 and 0.8%, respectively. To minimize the losses, we grew the SESAM by molecular chemical vapor deposition (MOCVD). The SESAM contains a single 10-nm-thick InGaAs quantum well in a standard low-finesse design [6, 7]. The SESAM exhibits a bitemporal impulse response with a fast (<1 ps) and a slow (102 ps) recovery time component. The SESAM is mounted on a water-cooled heat sink kept at ≈ 20°C.

We need sufficient self phase modulation and negative group delay dispersion (GDD) for soliton mode locking [21]. As the Kerr nonlinearity of the thin disk alone is too small for stable soliton pulses, we used a 1-mm-thick Brewster plate to increase the nonlinearity and to enforce linear polarization of the laser mode. The negative GDD is introduced by 11 dispersive mirrors, generating a total GDD of -22'000 fs^2 per round-trip. These mirrors have been produced by Layertec, Germany, and have been optimized for small absorption and thus for weak thermal effects.
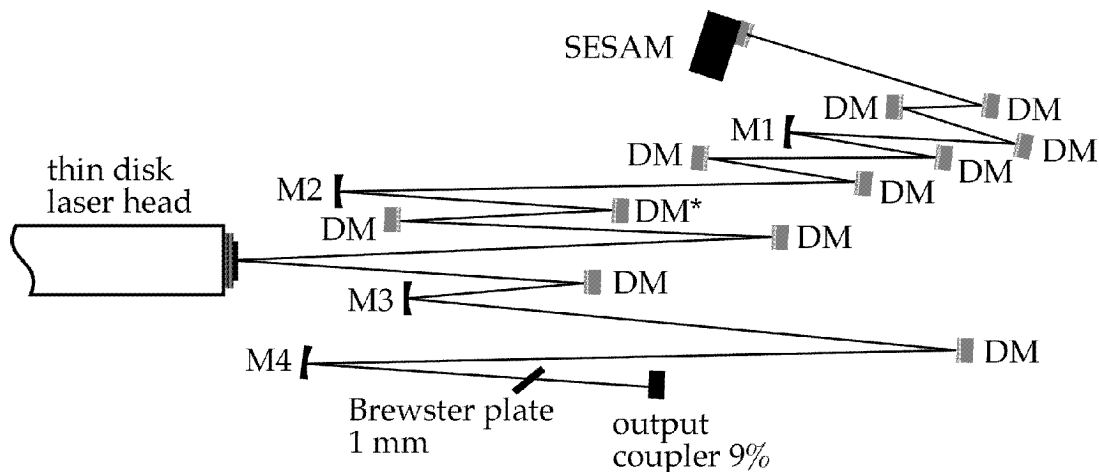
Figure 3.5: Setup of the Yb:YAG thin disk laser for the 810-fs pulses with 60 W average output power: M1-M4, spherically curved mirrors; DMs, dispersive mirrors with -1050 fs^2 per bounce; DM*, dispersive mirror with -540 fs^2 per bounce.

With the setup shown in Figure 3.5, we obtain self-starting mode locking with an average output power of 60 W in pulses of 810-fs duration (FWHM) at center wavelength of 1030 nm (Figure 3.6). We pump the Yb:YAG disk with 310 W at 940 nm.

The transmission of the output coupler is 9.0%. The pulse repetition rate is 34.3 MHz, corresponding to an output pulse energy of 1.75 μJ and a peak power as high as 1.9 MW. The time–bandwidth product is 0.34, which is slightly larger than the ideal time-bandwidth product for soliton pulses (0.315). The achieved beam quality is close to the diffraction limit, with an M^2 value measured to be below 1.1.
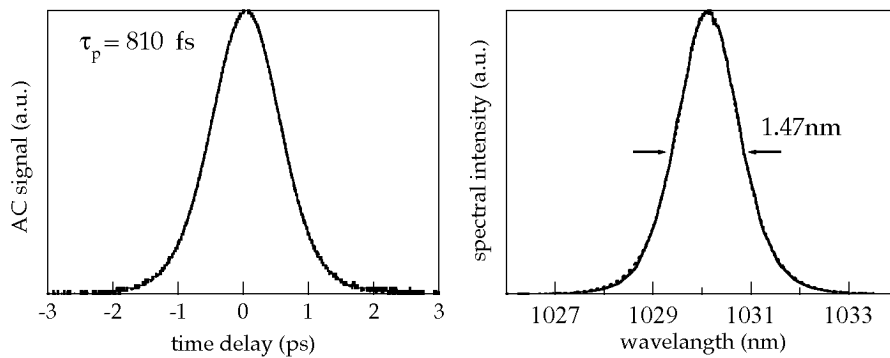
Figure 3.6:   Autocorrelation trace (right) and optical spectrum (left) of the 810–fs pulses obtained from the thin disk Yb:YAG laser at 60 W average output power. The dashed curves, representing sech²-fits, overlap the data well.

The laser mode radius in thin disk is calculated to 1.14 mm and the one on the SESAM 0.85 mm. Excessive thermal effects from the SESAM have not been observed, but there seem to be some thermal lensing effects in the dispersive mirrors, making the alignment somewhat more difficult than with normal highly reflecting mirrors. In addition, because of the very high intra-cavity intensity on the dispersive mirrors, we have seen damage of the dispersive mirrors. The dispersive mirrors have been operated at positions in the cavity with a laser mode radius between 200-800 μm leading to a very high peak intensity of 34 GW/cm² for the smallest laser mode radius. As the cavity was operated in the stability zone II [59], it was relatively sensitive against cavity misalignment.

A previous cavity setup of this laser was operated with only -9400 fs² intra-cavity dispersion, a lower output coupler transmission, and a smaller beam

radius on the Brewster plate. It was designed to make the generation of 800-fs solitons possible, assuming the calculated Kerr nonlinearity ≈ 45 mrad per cavity round-trip. However, in this configuration operated at full power the laser generated bunches of three or four pulses with equal energy, spaced by typically 0.7 to 0.8 ns, as was seen with a fast sampling oscilloscope. In this multiple pulsing regime, the autocorrelation, the sampling oscilloscope signal, and a photodiode signal observed with a radio-frequency spectrum analyzer appeared to be as stable as in the single-pulse regime. With lower pump power, fewer pulses or even a single pulse with similar energy was observed.

For the picosecond thin disk laser (see Section 3.2.3), we believe that we didn't have multiple pulses circulating in the laser cavity, because the calculated GDD required for soliton pulses of -91'000 fs^2 is close to the estimated value of -86'000 fs^2 introduced by the GTI.

We managed to obtain single pulses in the femtosecond regime at full power by exchanging some of the dispersive mirrors for others with more negative dispersion. These findings suggest that we had soliton pulses in the laser, but there was a significant additional nonlinear phase shift in the cavity. (Note that for a typical beam radius of the order of 0.6 mm the intra-cavity peak intensity is $\approx$3.7 GW/cm^2.) These findings also explain why we observed only a slight change of the pulse duration when we moved the Brewster plate to a position in the cavity where the beam radius was considerably smaller: Apparently only a smaller part (roughly one-sixth) of the total nonlinear phase shift ($\approx$0.1 rad) comes from the Brewster plate. The Yb:YAG disk does not significantly contribute to the Kerr nonlinearity because of its small thickness and large mode radius.

We took a number of measures to determine the origin of this additional nonlinear phase shift in the laser cavity and found out that it didn't appear that there was additional positive dispersion in the cavity (requiring more negative dispersion for solitons). We further could exclude the dispersive mirrors to be the origin of this phase shift, but couldn't finally determine the origin of this nonlinearity. As we didn't encounter such an additional phase shift in the 57–MHz setup anymore (see Section 3.2.4.2), we didn't further investigate this issue.

To confirm single-pulse operation in the final setup (in addition to the measurement with the sampling oscilloscope), we measured the efficiency of second-harmonic generation in a critically phase-matched 5-mm-long LiB_3O_5 crystal. We did this measurement with the output beam of the laser attenuated to a few watts in the regime with low conversion efficiency. The measured efficiency is in reasonable agreement with the expectation for single-pulse operation, whereas in earlier cases with multiple pulsing the efficiencies were significantly lower because of the reduced peak powers.

3.2.4.2   80-W setup with 57-MHz repetition rate

To overcome the damage problem of the dispersive mirrors and to improve the stability of the laser, we decided to change the setup for operation in stability zone I and to increase the pulse repetition rate to reduce the pulse energy. Moreover, the cavity allows operating the dispersive mirrors at positions with larger laser mode radii and we increased the nonlinear phase shift in the Brewster plate to increase the stability of the mode locking process. The thermal effects in the dispersive mirrors could be further reduced with new mirrors, which showed less thermal lensing effects. As a consequence of designing the mirrors for minimal absorption, they exhibit less negative GDD per bounce. This can be balanced by increasing the number of the dispersive mirrors.

A 1.5–mm–thick Brewster plate provides the required nonlinear phase shift of 69 mrad per cavity round-trip for soliton mode locking. In addition, the Brewster plate enforces linear polarization of the laser. The negative GDD is introduced by 11 dispersive mirrors, generating a total GDD of ≈-12000 fs^2 per cavity round-trip. We operate the dispersive mirrors with mode radii between 740–1000 μm and so we could reduce the maximum peak intensity by a factor of 17 below 2.2 GW/cm^2 compared to the laser discussed in Section 3.2.4.1. At this peak intensity we didn't observe damage of the dispersive mirrors anymore.

The laser mode radius in this configuration is calculated to be 1.18 mm on the thin disk and 0.68 mm on the SESAM. We again use a semiconductor saturable absorber mirror for the passive mode locking process grown with MOCVD and based on a standard low-finesse design [6, 7]. The measured

saturation fluence of this SESAM is 17 μJ/cm² and the modulation depth is 0.9% (see Figure 2.4 and Figure 2.5). The structure of the SESAM contains a single 10–nm–thick InGaAs quantum well. The SESAM exhibits a bitemporal impulse response with a fast (<1 ps) and a slow (110 ps) recovery time component. The SESAM is mounted on a water-cooled heat sink kept at ≈ 20°C and operated 67–times above the saturation fluence. Despite this relatively high saturation parameter, we didn't observe damage of the SESAM in the mode locking operation.
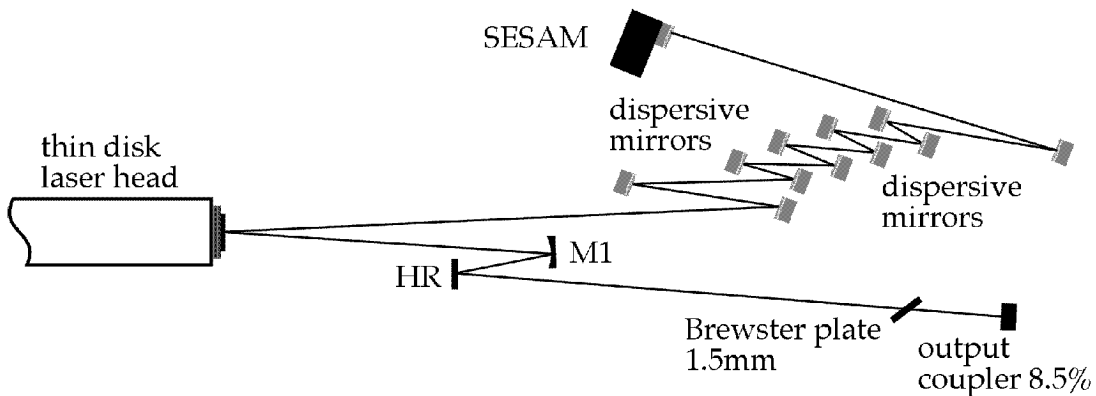
Figure 3.7:   Setup of the Yb:YAG thin disk laser for the 705-fs pulses with 80 W average output power: SESAM, semiconductor saturable absorber mirror; $M1$, spherically curved mirror; dispersive mirrors with -550 fs² per bounce; HR, high reflector.

Such a high saturation parameter can be reduced with an additional coating on top of the SESAM. Top-coated SESAMs with a higher saturation fluence and therefore lower modulation depth have been grown by molecular beam epitaxy (MBE) and have already been successfully used in the laser.

The setup of the optimized laser cavity is shown in Figure 3.7. We obtain self-starting mode locking with an average output power of 80 W in pulses of 705-fs duration (FWHM) at center wavelength of 1030 nm (Figure 3.8). The transmission of the output coupler is 8.5%. The pulse repetition rate is 57 MHz, leading to an output pulse energy of 1.4 μJ and a peak power of 1.75 MW. The pulses are transform-limited solitons and the output beam is nearly diffraction-limited, with an $M^2 < 1.1$.
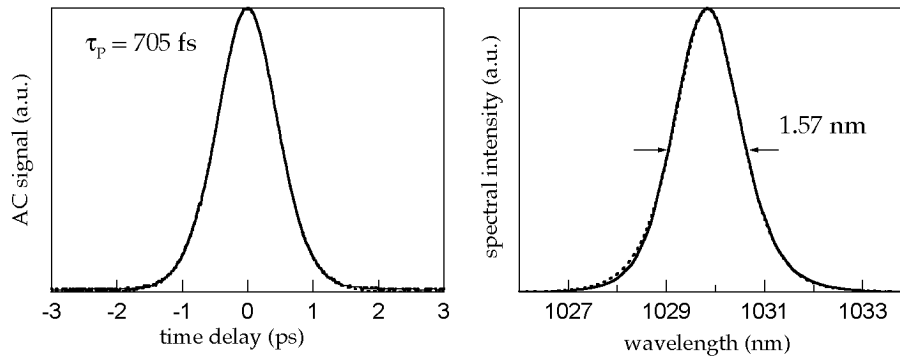
Figure 3.8:   Autocorrelation trace (right) and optical spectrum (left) of the 705-fs pulses at 80-W average output power. The dashed curves represent sech^2 fits.

To our knowledge, this is the highest average output power from a mode-locked laser with femtosecond pulse duration reported to date.

3.3 Further scaling of passively mode-locked thin disk lasers

In this paragraph, we will shortly address the issue of scaling passively mode-locked thin disk lasers to higher average output powers and to higher pulse energies.

3.3.1 Towards higher average power

Despite the power scalability of the concept of a thin disk laser mode-locked with a SESAM, the further progression to higher average output power in femtosecond pulses is not straightforward. First of all, a laser head that is running in single-transverse mode with a large pump mode area is required. This seems to be more difficult to achieve at higher power levels, as the pump mode area on the thin disk has to be increased and it is more difficult to have good quality disks with larger diameters. In addition, a larger laser mode radius results in a smaller width of the stability range against thermal lensing

[59] and therefore one has to know the thermal lens of the gain medium more accurate to get stable laser operation. And as the focusing power of the thermal lens changes with pump power, it even can happen for a very large laser mode areas (and thus small stability range) that the laser cavity is no longer stable over the whole pump power range.

An issue that also will have to be considered is damage of intra-cavity components, as scaling of the mode area on disk and SESAM doesn't necessary scale the mode area on other critical components. Thermal induced stress caused by inhomogeneous temperature distributions in the gain medium also is an issue that will be more severe at higher power levels and can lead to stress fracture of the disk.

Possible solutions for increasing the average output power of a thin disk laser while retaining the intra-cavity intensity on the sensitive components would be either increasing the mode areas on those components or increasing the number of passes of the laser resonator over the gain material. With such additional gain also the output coupling could be increased resulting in lower intra-cavity power.

3.3.2 Towards higher pulse energies

Scaling the thin disk laser to higher pulse energies is currently limited by the damage of the dispersive mirrors. The pulse repetition rate presented in the result with 60 W in 810-fs pulses (see Section 3.2.4.1) was 34 MHz. Since the laser beam radii on the dispersive mirrors were between 200-800 μm, the corresponding peak intensities were as high as 34 GW/cm^2 for the smallest mode radii. In this configuration, we regularly observed damage of dispersive mirrors. With the modified design of the 57-MHz cavity (see Section 3.2.4.2), we operated the dispersive mirrors at larger mode radii between 770-1000 μm and therefore had a 17-times lower peak intensity (below 2.2 GW/cm^2) on the dispersive mirrors.

We believe that the maximum peak intensity our dispersive mirrors can stand lie between those two values. A first step towards higher pulse energy will be to reduce the pulse repetition rates while keeping the laser mode radii

on the dispersive mirrors as large as possible. For example with the same beam parameters as for the 80 W laser, but with a pulse repetition rate of 30 MHz, the peak intensity on the dispersive mirrors would be below 4.2 GW/cm^2, resulting in an increase of the pulse energy from 1.4 µJ to 2.7 µJ.

However, a further rise of the pulse energy seems only possible by keeping the peak intensity on the dispersive mirrors constant. There are future plans to increase the number of passes of the laser beam over the disk. This will increase the laser gain. In order to keep the intra-cavity power constant, the transmission of the output coupler has to be increased by the same factor as the laser gain. One important issue will be the strength of the cumulative effects (due to the multiple passes over the disk) of beam distortions caused by thermal lensing and imperfections in the disk. Another crucial aspect will be the cavity design, which even gets more challenging because of additional boundary conditions.

Chapter 4

High Power RGB Laser Source

There is a demand for large digital laser projection displays, as could be used e.g. in cinemas and for flight simulators. Laser projectors have numerous advantages over conventional lamp projectors. The color gamut (see Section 4.5) from a red-green-blue (RGB) laser source is much wider than the one from a high-definition TV (HDTV) and excellent color saturation can be achieved. A laser projector permits fully digital data recording, handling, transmission and storage, which brings additional advantages compared to analog film rolls. Moreover, the large focal depth of laser beams allows for projection even onto curved surfaces.

The required projection technology already exists, whereas the design of a suitable RGB laser source with very high output power is still challenging, particularly when additional requirements, such as long life time, stable maintenance-free long-term operation, compactness and reasonable price, are introduced. An interesting approach is to start with a single infrared laser, from which all colors are generated in nonlinear conversion stages. Previously, the required high infrared power for a system with several watts per color could only be produced by supplementing the infrared laser with one or several amplifier stages [42, 71]. Passively mode-locked thin disk lasers ([53, 72] and Chapter 3) promise a significant advance towards commercially viable RGB sources, as they directly allow to generate very high powers.

For a given laser wavelength, a variety of different combinations of nonlinear conversion stages could generate the RGB beams (see e.g. Ref. [73]). In practice, the viability of a scheme depends strongly on the laser parameters such as pulse duration, peak power, and beam quality. Ideally, one should find the optimal conversion scheme for given laser parameters. However, this would be prohibitively complicated because of the number of possible schemes to evaluate and the large number of parameters corresponding to multiple conversion stages in each scheme. Furthermore, there is not a well-defined optimum in terms of technical parameters like output power and beam quality. The optimal scheme for an application may depend on additional constraints such as cost and availability of components. For these reasons we restrict our analysis to one particular scheme. This RGB system [9] consists of a passively mode-locked thin disk laser used as pump source, a frequency doubler, an optical parametric generator (OPG), an optical parametric amplifier (OPA), and two sum frequency generation (SFG) stages. Thanks to the short pulses and the high peak power a mode-locked thin disk laser generates, the system eliminates the need for resonant conversion stages, and with the exception of the crystal in the OPG, all the crystals are critically phase-matched and operated at room temperature. The temperature-stabilized crystal in the OPG stage can in future be replaced with a magnesium-doped crystal operated at room temperature, as we have recently shown [74]. Our analysis of the RGB system is based both on the mentioned experimental results and on an advanced numerical model [11] that allows to simulate the nonlinear conversions.

In this Chapter we will present a powerful RGB laser source that simultaneously generates 8 W in the red, 23 W in the green and 10.1 W in the blue spectral region. In Section 4.1, we discuss the experimental and simulation results for the second-harmonic generation stage. The advantages of a setup with an OPG and a subsequent OPA and its performance details are addressed in Section 4.2. The two SFG stages are discussed in Section 4.3. Section 4.4 presents a discussion of the overall system and its potential for further improvements. Finally, in Section 4.5, we review the definitions of a chromaticity chart and a color gamut and compare the achieved performance of the RGB system with a color gamut of a HDTV.

4.1 Second-harmonic generation

The infrared pump power for the nonlinear conversion stages of the RGB system is delivered by an Yb:YAG thin disk laser passively mode-locked with a SESAM [6, 7]. The Yb:YAG laser has been presented in Section 3.2.4.2 and delivered 79 W of average power in 780 fs. With a spectral bandwidth of 1.67 nm, the time-bandwidth product is 0.37, which is slightly larger than the ideal time-bandwidth product for soliton pulses (0.315). The pulse repetition rate is 57 MHz, leading to an output pulse energy of 1.39 μJ and a peak power of 1.57 MW. All pulse lengths and spectral widths in the following Chapter are given as full width at half maximum (FWHM) and the time bandwidth products are based on these measures. The beam radii correspond to $1/e^2$ intensity radii. The high average output power of the Yb:YAG thin disk laser is sufficient to pump all subsequent nonlinear conversion stages, so that no laser amplification stage is required.

4.1.1 Experiment

The experimental setup of the RGB system is shown in Figure 4.1. The laser output beam first enters a frequency doubler based on a 5-mm-long antireflection-coated LiB_3O_5 (LBO) crystal. LBO is an attractive nonlinear material with versatile phase-matching options and the potential for high power operation. We use a critical phase-matching scheme of type I (oo-e) at room temperature with a phase-matching angle of $\varphi_{pm} = 13.77°$ and a nonlinear coefficient of $d_{31} = 0.85$ pm/V (using the notation of Roberts [75]). For the phase-matching scheme with the propagation direction in the XY plane, the effective nonlinearity is $d_{eff} = d_{31} \cdot \cos(\varphi_{pm}) = 0.827$ pm/V and the walk-off angle for the second harmonic wave is $\rho = 8.29$ mrad. The pump beam was focused to a spot with a beam waist of ≈ 130 μm radius.
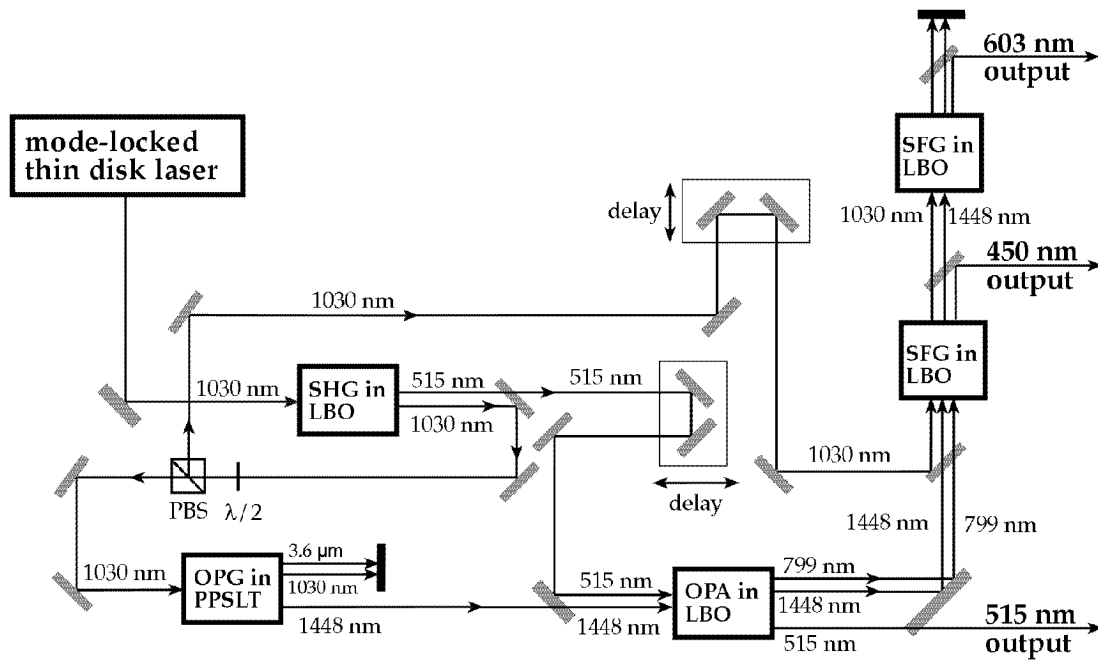
Figure 4.1: Experimental setup of the RGB source. λ/2, half-wave plate; PBS, polarizing beam splitter; SHG, second-harmonic generation; OPG, optical parametric generation; OPA, optical parametric amplification; SFG, sum frequency generation. All beams are collinear in the nonlinear crystals, although for clarity they are shown with some spatial separation.

With the crystal in the beam waist, we obtained up to 48 W of average power at 515 nm, corresponding to a conversion efficiency of 61% (see Figure 4.2). During the RGB experiment, we intentionally moved the SHG crystal somewhat out of the beam focus (to a position with pump radius ≈ 150 μm) so as to obtain 45.6 W in the green beam and 30.3 W residual power at 1030 nm. At this power level, the pump intensity in the LBO crystal was 4.4 GW/cm². The beam quality of the green wave is close to the diffraction limit with an M^2 value of 1.1, where a knife-edge method was used for the measurement.
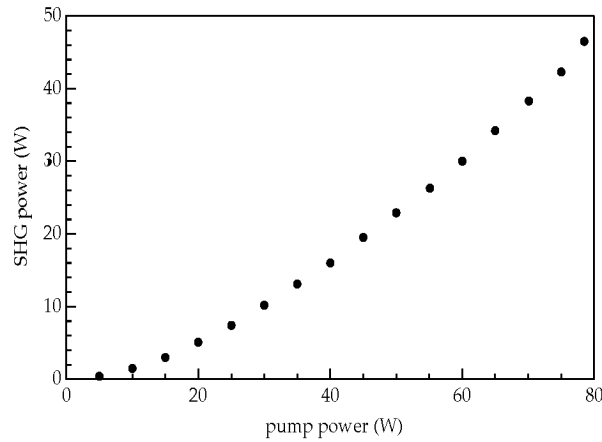
Figure 4.2:   Measured power slope of the 515-nm wave after the frequency
doubler.

4.1.2 Simulation and discussion

We simulated the nonlinear interaction in the SHG stage using a Fourier-space method in three dimensions (one temporal and two transverse spatial dimensions) to solve the coupled differential equations for the slowly varying eigenmode amplitudes. This numerical method also includes the effects of birefringence and exact dispersion [11]. The computer program can handle arbitrary propagation directions in uniaxial and biaxial crystals. The numerical model is capable of using the output field from a previous stage as input for a subsequent nonlinear process. This is important because the beam qualities of the pump waves degrade due to pump depletion effects.

The numerical simulations are generally in good agreement with the measurements. They show that the beam quality of the generated second-harmonic wave remains good even for very high conversion efficiencies (see Figure 4.3); i.e., the simulation yields $M^2 < 1.1$ even for 84% conversion efficiency. On the other hand, due to pump depletion, the M^2 factor of the residual pump wave increases for increasing conversion efficiency.
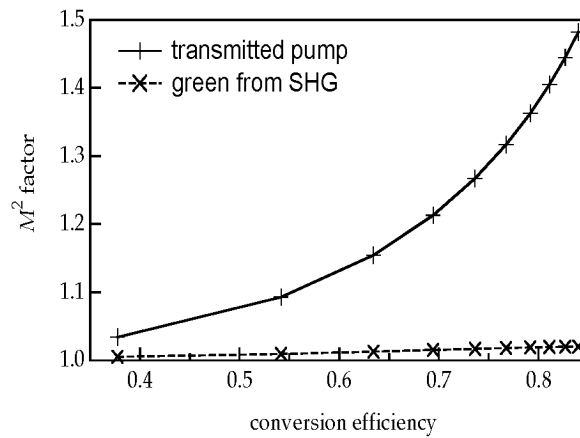
Figure 4.3: Simulated beam quality of the second-harmonic wave at 515 nm and the transmitted pump wave at 1030 nm in the SHG. The data points correspond to different pump powers in the range of 30 – 300 W, and the beam quality is plotted versus the conversion efficiency.

Simulations predict that a conversion efficiency of 86% could be obtained by using a longer (12-mm-long) LBO crystal with the same pump intensity as used for the RGB experiment. While the generated green wave still shows an M^2 factor of 1.04 (see simulated near field fluence in the right graph of Figure 4.4) at a conversion efficiency of 86%, the beam quality of the pump beam has already deteriorated (see left graph of Figure 4.4).

Figure 4.4: Simulated near field fluence of the residual pump (left) and the second-harmonic wave (right) in the SHG stage for 86% conversion efficiency with a 12-mm-long LBO crystal.

For the experimental conditions, good beam quality for both second-harmonic and residual pump is expected. As a result of pump depletion and temporal walk-off, the pulse durations of the second-harmonic wave and the transmitted pump beam increase for increasing conversion efficiency. For the 5–mm-long LBO crystal used in the experiment, the spatial walk-off is more important than the temporal walk-off. The amount of green power generated is crucial for the following OPG/OPA, as it serves as the pump power for the amplifier stage. However, we also need sufficient power at 1030 nm for the OPG and the subsequent sum frequency stages.

4.2 Optical parametric generator and optical parametric amplifier
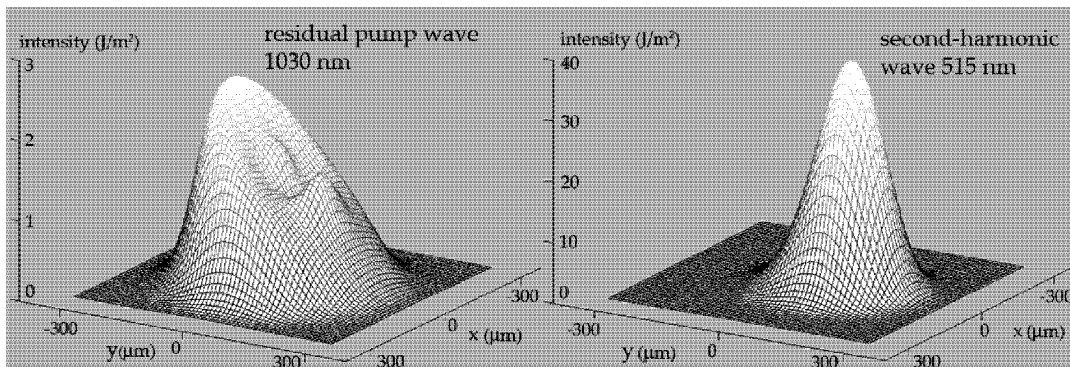
4.2.1 Experiment

We have chosen the approach of an OPG and a subsequent OPA to generate waves with multiwatt average power at 800 nm and at 1.5 μm required for the following SFG stages. With this approach, the problem of insufficient output beam quality in efficient high gain parametric processes [76] can be solved. A more detailed discussion of this issue can be found in the following Section. The OPG stage generates a signal wave at 1448 nm and an idler wave at 3568 nm. The OPG is based on a periodically poled stoichiometric $LiTaO_3$ (PPSLT) crystal [77]. This material is very attractive for high power parametric processes because of its versatility concerning phase matching, its high nonlinearity and its high photorefractive damage resistance. The wavelengths of the generated signal and idler waves can be selected with the grating period and operation temperature of the PPSLT crystal. The OPA stage based on LBO boosts the power at 1448 nm to the multiwatt level and at the same time creates an idler wave at 799 nm. The two-stage approach allows for a nearly diffraction-limited beam quality of signal and idler waves because the power amplifier stage is operated with a lower gain (energy gain of $\approx$ 8 dB) so that gain guiding is less important.

We pump the OPG stage with a fraction of the residual 1030-nm light from the SHG. The uncoated PPSLT crystal of the OPG stage has a length of 17.5 mm and is operated in a temperature-stabilized oven at 150 °C to avoid photorefractive damage. Very recently, we have demonstrated stable room temperature OPG operation in periodically poled MgO-doped stoichiometric $LiTaO_3$ with high average power (see Section 5.2 and [74]), which would allow to operate of the OPG stage in a future RGB system at room temperature. We use the PPSLT crystal in a double-pass configuration to obtain sufficient parametric gain without reaching the threshold for optical damage. After a first pass through the crystal, the pump and signal waves are re-imaged with a curved mirror into the crystal for a second pass. The idler wave and some parasitic green light arising from higher-order phase-matched second-harmonic generation are eliminated after the first pass through the OPG crystal with dichroic mirrors. Finally, the signal wave is separated from the pump with a dichroic mirror. The poling period of the nonlinear crystal is 29 μm. The nonlinear coefficient of the PPSLT crystal is estimated to be 8.2 pm/V (see Section 4.2.2). Fresnel reflections on the uncoated crystal faces introduce relatively large losses of $\approx$13% at a wavelength of 1030 nm per surface, which could be drastically reduced with an antireflection coating. The pump waist in the nonlinear crystal is 22 μm, which leads to an internal pump peak intensity of 11.6 GW/cm^2 for 7.7 W of pump power incident on the crystal (calculated with the simulated pump pulse duration of 1180 fs for the residual 1030 nm wave after the SHG stage). At this intensity, the OPG runs stably without crystal damage and generates 1.6 W of average power at 1448 nm. The OPG threshold was at 6.4 W of pump power incident on the crystal. The measured intensity autocorrelation and the optical spectrum at a signal average power of 1.6 W are shown in Figure 4.5. The intensity autocorrelation shows signs of strong temporal pulse distortion. Despite this temporal pulse distortion, we roughly estimated the FWHM pulse duration of the signal to $\approx$ 1.4 ps (for a sech^2-fit).
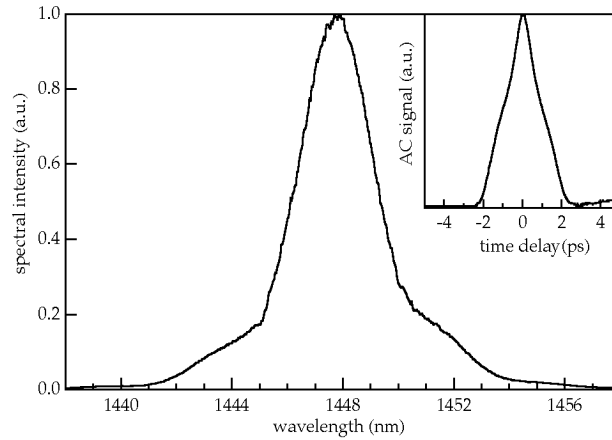
Figure 4.5:   Optical spectrum and autocorrelation trace (inset) from the OPG
at 1.6 W of average signal power.

The parametric amplifier stage is based on a 10-mm-long LBO crystal that is critically phase-matched at room temperature. The LBO crystal in the OPA is pumped with the green beam from the SHG. The beam waist of the 515-nm wave in the antireflection-coated LBO crystal is 125 μm and the signal waist 210 μm. The antireflection coating (AR) of the LBO introduces relatively large reflection losses of 1% at 515 nm, 2% at 799 nm and 4.2% at 1448 nm and those losses could be reduced with better coatings. Phase matching is achieved with a type-I scheme (oo-e in XY plane) at room temperature with a phase-matching angle of $\varphi_{pm} = 11.85°$ and a nonlinear coefficient of $d_{31} = 0.85$ pm/V. The effective nonlinearity is 0.83 pm/V and the walk-off angle of the pump wave $\rho = 7.21$ mrad.
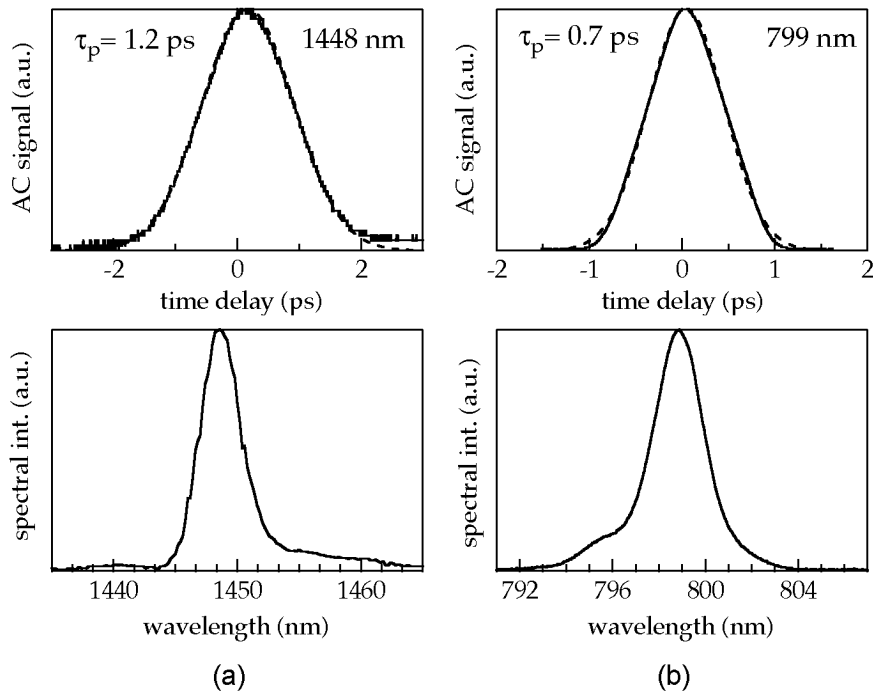
Figure 4.6: Optical spectrum (bottom) and autocorrelation (top) of the signal wave at 1448 nm (a) and the idler wave at 799 nm (b) of the OPA.

The peak intensity of the pump wave in the LBO crystal for a pump power of 42.4 W of the OPA is calculated to be 3.9 GW/cm^2 (without pump depletion and for a simulated pulse duration of the green pump pulses of 680 fs). We obtained up to 7 W of average signal power at 1448 nm and 11.9 W of average idler power at 799 nm. The internal conversion efficiency from pump to signal and idler waves combined is 47%. The measured pulse durations for signal and idler are 1.2 ps and 0.7 ps, respectively (see Figure 4.6). The beam quality of the idler is close to the diffraction limit with a measured M^2 factor of 1.2. The residual 23 W of green light is separated from the signal and idler wavelengths and used as a first output of the RGB system. The beam quality of the 515-nm output is still fairly good with an M^2 factor of 1.9. The degradation of the spatial beam quality of the 515-nm light is caused by pump depletion in the OPA stage.

4.2.2 Simulation and discussion

For the generation of wavelengths in the blue and the red spectral region with the process of sum frequency generation with the fundamental wave at 1030 nm, beams at 800 nm and at 1.5 μm with high average power and good beam quality are required. Optical parametric oscillators (OPOs) are often used to generate beams in the 1.5-μm spectral region. However, a disadvantage is the required synchronization of the OPO cavity with the laser cavity, which for long-term stable operation in the femtosecond regime often requires a feedback stabilization scheme, which would make the RGB setup more complex. Such additional complexity is avoided with the use of an OPG. However, OPGs require a high parametric gain and thus high intensities in the nonlinear crystal. Therefore, OPGs are typically pumped with amplified laser sources that operate at kilo-hertz repetition rates and are therefore not suitable for most laser displays. An OPG directly pumped with a mode-locked laser (at a multi-MHz repetition rate) has been demonstrated for the first time in 2001 with femtosecond pulses from a passively mode-locked thin disk laser [78, 79]. Somewhat later, similar experiments have been performed with higher average power in picosecond pulses [80].

Although the necessary pump power is now directly available from lasers, the generation of high power 800-nm and 1.5-μm beams in a single OPG stage is not practical. First, it has been recognized that the combination of high parametric gain, high output power and good conversion efficiency is subject to severe limitations, which are related to gain guiding [76]. Second, generating these wavelengths in an OPG would require a green pump beam, and crystals with gain high enough for the OPG, such as lithium tantalate, would be susceptible to optical damage from a high-power green beam. By combining a 1-μm pumped OPG stage of lower output power with a 515-nm pumped high power OPA with moderate gain based on LBO, we have evaded all the above-mentioned limitations. Note that the conversion efficiency of the OPG is not very important since the OPA can cope with limited signal pulse energy.

We investigated the OPG process further using the same numerical simulation model as in Section 4.1.2 [11]. The model uses signal and idler inputs with numerically generated fluctuations to simulate the quantum noise, from

which the OPG starts. The GVM automatically enters the model by using the Sellmeier equations of Ref. [81] to calculate the wavelength dependence of the refractive index. The measured OPG threshold is consistent with a nonlinearity of 8.2 pm/V in the simulations, which seems to be a reasonable value. Note that we are using a double-pass configuration, where pump and signal beams are reflected back into the crystal with a curved mirror. We also found that a significantly higher conversion efficiency would in principle be possible for pumping further above threshold, but even if damage could be avoided in this regime of operation, problems would arise from pulse break-up: for high pump powers, an additional pulse behind the main pulse is generated and results in a broadening of the pulse (see dashed line in the right graph of Figure 4.9). This explains the roughly triangular shape of the autocorrelation (see Figure 4.5) for the highest output powers. The distorted pulse is a result of combined pump depletion, GVM, and, at the highest powers, backconversion.

We also used the numerical model to investigate how to optimize the performance of the OPA. The pump power at 515 nm is an important parameter for increasing the average power of the generated signal and idler waves. More pump power results in higher average power of both the signal and idler waves (see Figure 4.7a).
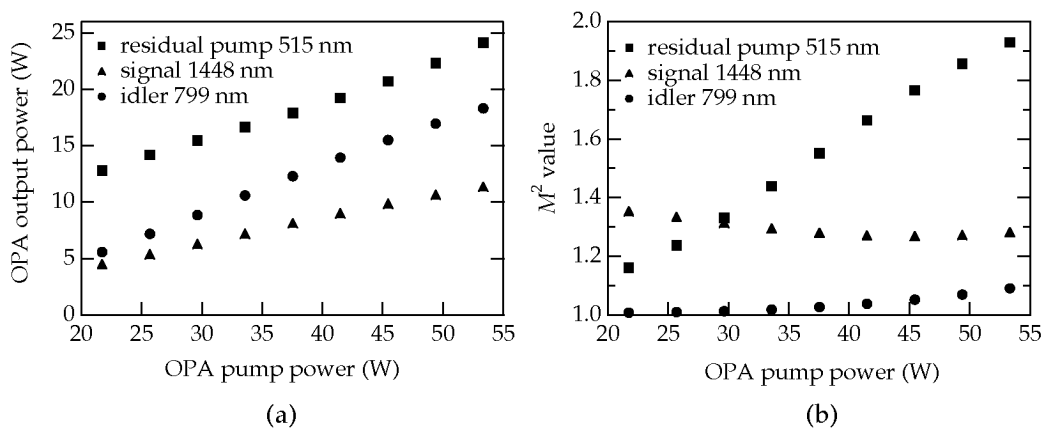

Figure 4.7: Dependence of the output power (a) and the beam quality (b) of the OPA on the 515-nm pump power.

The beam quality of the signal wave is slightly improved for higher pump powers, whereas the beam quality of the residual pump gets reduced due to pump depletion (Figure 4.7b). The pulse duration of the signal wave is decreasing for increasing pump power while pump depletion causes the transmitted pump pulse duration to increase. As the saturation of the amplifier is significant, the output powers of signal and idler waves can only slightly be increased for higher seed average power (see Figure 4.8a).

(a)   (b)
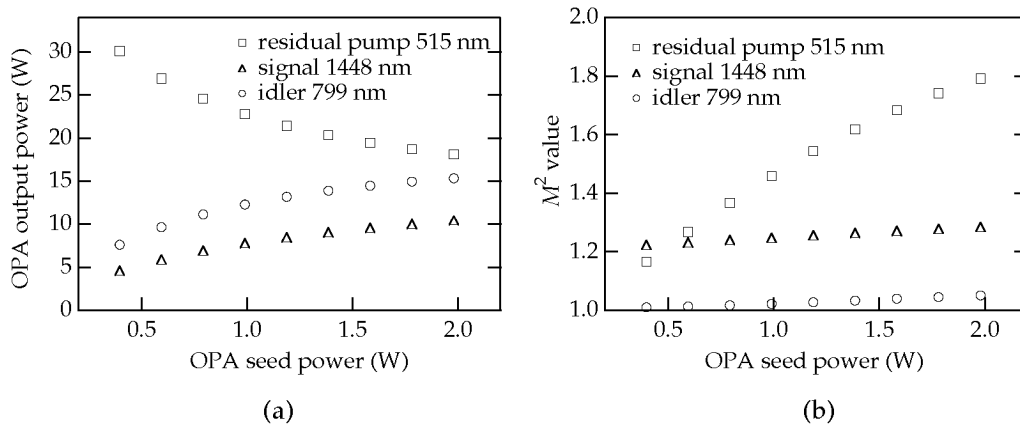
Figure 4.8:   Dependence of the output power (a) and the beam quality (b) of the OPA on the 1448-nm seed power.

It might seem beneficial to use a longer nonlinear crystal to improve the conversion efficiency, but due to the spatial walk-off the signal and idler powers are reduced for crystals longer than 10 mm (with the beam radii optimized for each crystal length). Better conversion could be obtained with a walk-off-compensated setup, in which a second crystal is oriented so as to compensate the walk-off from the first crystal. For example, with two 5-mm-long LBO crystals in a walk-off compensating setup (instead of one 10-mm-long crystal and with similar beam radii), the output powers of the signal and idler wave would be increased by 12% and 11%, respectively. We did not use a shorter crystal, because the pump radius would then have to be smaller and this would result in higher pump intensity, increasing the risk of damage. In addition, stronger focusing in the 10 mm crystal will not improve the efficiency either, because of backconversion and spatial walk-off.

The amplification process smoothes the temporal pulse shape of the input signal pulse. Figure 4.9 shows a simulation of the temporal (see Figure 4.9, upper graphs) and spatial (see Figure 4.9, lower graphs) pulse shapes of the signal wave before (dashed curve) and after (solid curve) the amplification process in the OPA. In both simulations, we used the pump pulses at 515 nm originating from the SHG simulations.
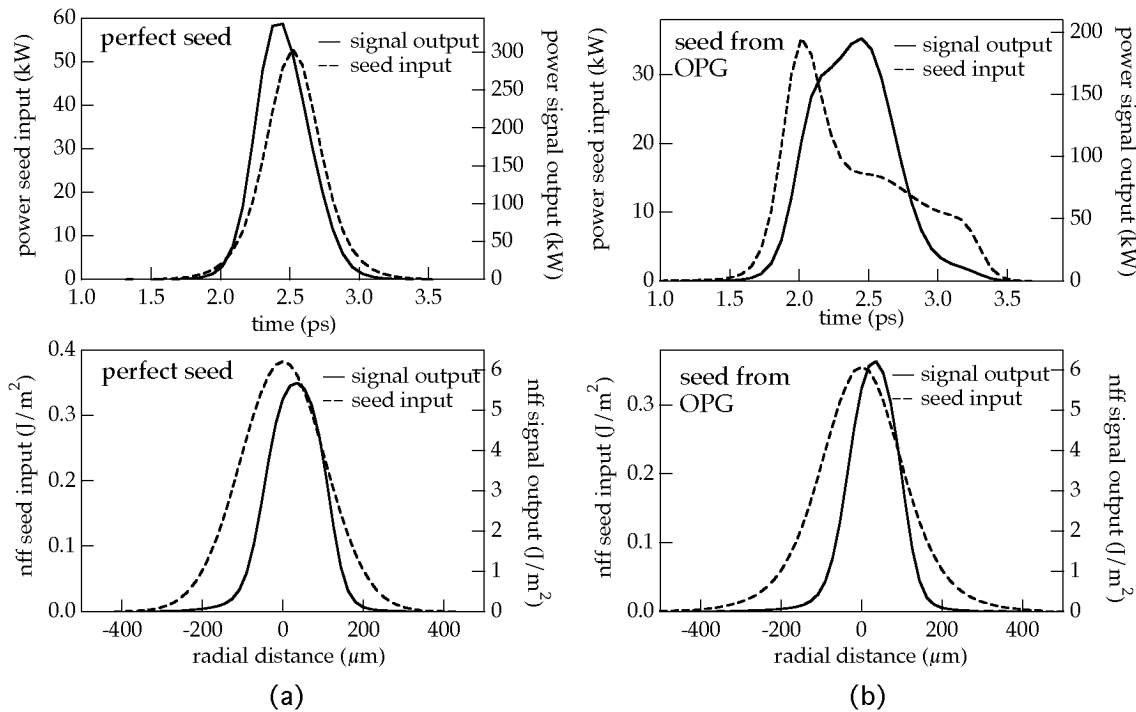
Figure4.9:   Simulated instantaneous power (top) and near field fluence (bottom) in the critical plane of the signal pulse before (dashed) and after (solid) the OPA for a perfect Gaussian seed beam (a) and a simulated OPG signal (b). The temporal profile of the distorted signal wave (b) is improved during the amplification process. (nff corresponds to near field fluence).

While in the left graphs in Figure 4.9, the seed pulse is assumed to have a perfect Gaussian spatial shape and a $sech^2$–shaped temporal profile, we used the simulated signal output pulse from the OPG stage in the right graph. The ideal pulse was chosen such that it had the same pulse energy and FWHM pulse duration as the simulated OPG signal pulse. The improvement of the temporal shape of the OPG signal pulse can clearly be seen. The signal output

power of the OPA for an ideal seed beam would however be 10% higher than with the real temporally distorted beam from the OPG.

The simulated optical spectrum (see Figure 4.10b) of the green output of the RGB system is quite similar to the measured optical spectrum (see Figure 4.10c). The shoulders in the optical spectrum of the green output are caused by pump depletion, which imposes fast temporal variations on the pump beam resulting in a broader spectrum. The simulated optical spectrum of the pump pulse entering the OPA stage does not yet show such shoulders (see Figure 4.10a).

(a)   (b)   (c)
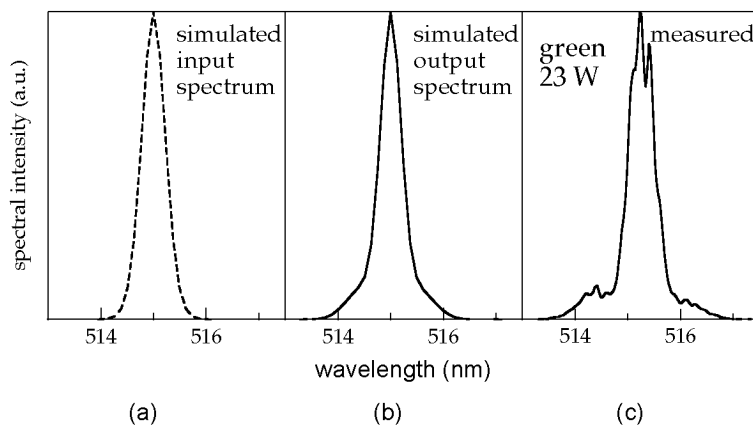
Figure 4.10: Simulated optical spectrum of the pump beam at 515 nm before (a) and after (b) the amplification process in the OPA stage. Measured optical spectrum (c) of the 515-nm output of the RGB system (i.e. after the OPA). The shoulders in the spectrum are caused by pump depletion.

The effect of pump depletion in the OPA can also be seen in the simulated near field fluence of the residual 515-nm pump wave (see Figure 4.11, right graph).
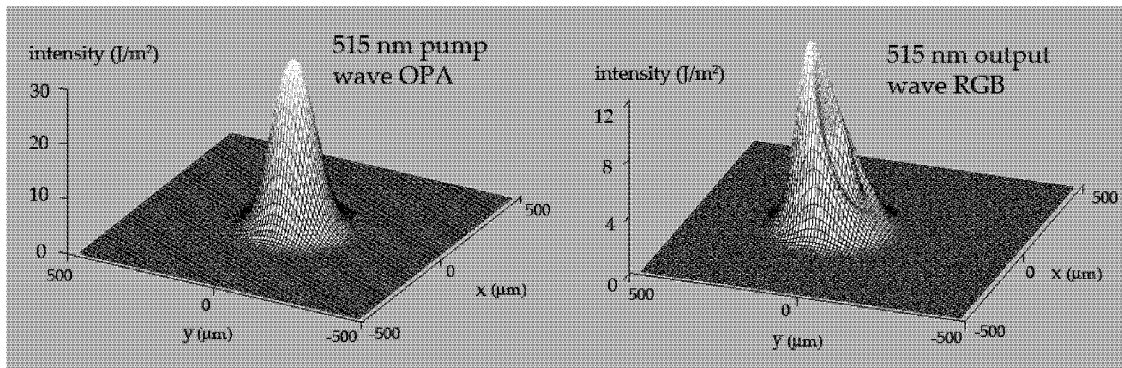
Figure 4.11: Simulated near field fluence of the 515 nm beam before (left) and
after (right) the amplification process in the OPA. The residual
pump beam shows signs of pump depletion and backconversion.

Note that the power losses at the imperfect AR coatings (see Section 4.2.1) are significant. Assuming that we could obtain LBO crystals with only 1% reflectivity per surface for all wavelengths, simulations suggest that we would obtain 5% higher signal and 3% higher idler powers, namely 9.6 W at 1448 nm and 14.5 W at 799 nm. As the amount of signal and idler power is crucial for the following SFG stages, this would significantly increase the power of the generated red and blue beams.

4.3 Sum frequency generation

4.3.1 Experiment

The wavelengths in the blue and the red spectral region are generated in two subsequent SFG stages where we mix the idler and signal wave from the OPA with the residual 22.6 W of 1030-nm light from the frequency doubler. The two SFG stages are based on two antireflection-coated LBO crystals, both critically phase-matched at room temperature. The first SFG crystal is 10 mm long and mixes the 799-nm wave with the 1030-nm beam to generate the blue color at a wavelength of 450 nm (see right graph in Figure 4.12). The beam radii in the waist of the 1030-nm wave and the idler beam from the OPA are 205 μm. Phase-matching in the first SFG stage is achieved with a type-I scheme (oo-e in XY

plane) with a phase-matching angle of $\varphi_{pm} = 22.46°$ and a nonlinear coefficient of $d_{31} = 0.85$ pm/V. The effective nonlinearity is 0.79 pm/V and the walk-off angle of the blue beam $\rho = 12.9$ mrad. The AR coating of this LBO crystal again introduces relatively large reflection losses per surface of 1.2% at 1030 nm, 1.8% at 799 nm, 4% at 450 nm, and 3% at 1448 nm. The second SFG crystal is 15 mm long and generates the red beam at 603 nm (see left graph in Figure 4.12) by mixing the 1448-nm wave with the remaining 1030-nm light. Phase matching in the antireflection coated LBO crystal is obtained with a type-I scheme (oo-e) with a rather small phase-matching angle $\varphi_{pm} = 0.6°$, i.e., close to a noncritically phase-matched configuration, where the spatial walk-off is also small ($\rho = 365$ μrad). The effective nonlinear coefficient is 0.85 pm/V. The beam radii of the 1030-nm input wave and the 1448-nm wave are both 105 μm in the waist. Because of the small spatial walk-off, we can use a tighter beam waist than in the first SFG stage. The reflection losses in the coatings of this LBO crystal are 1.8% at 1030 nm, 1% at 603 nm, and 3.5% at 1448 nm. The peak intensity of the pump waves added in those two LBO crystals is well below 2 GW/cm^2.
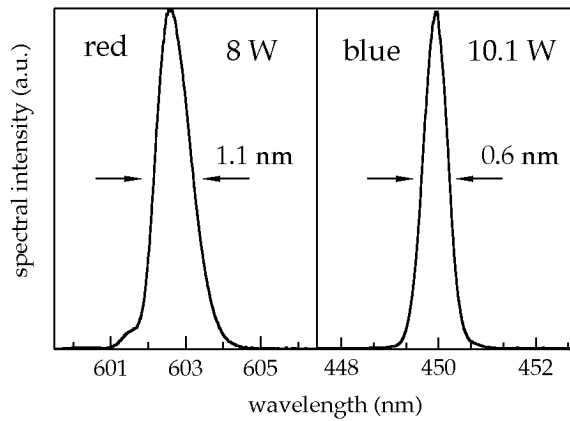

Figure 4.12: Measured optical spectra of the 603-nm red (left) and 450-nm blue (right) outputs of the RGB system.

The generated blue beam at 450 nm has an average power of 10.1 W and the beam quality is close to the diffraction limit, with $M^2 = 1.1$. The average power of the red beam at 603 nm is 8 W, again in a nearly diffraction-limited beam with $M^2 = 1.1$.

4.3.2 Simulation and discussion

The following discussion is based on qualitative considerations, numerical simulations (based on the same numerical code as described above), and on experimental experience, which is in good agreement with the simulations.

The order of the two sum frequency generation stages (first for blue, then for red) is dictated by phase-matching considerations: the SFG for generation of red light is close to noncritically phase-matched, i.e., with a very small spatial walk-off, which allows strong focusing and thus reasonable efficiency even with a low power in the residual 1030-nm light. On the other hand, the SFG stage for generation of blue light has a large spatial walk-off, which prevents strong focusing and thus requires a higher 1030-nm input power. However, the available amount of pump power at 799 nm is smaller ($\approx$12 W incident) and thus more limiting (see Figure 4.14a) than the power at 1030 nm (see Figure 4.13a).

(a)   (b)

Figure 4.13: Dependence of the output power (a) and the beam quality (b) of the SFG stage for the generation of the blue beam on the 1030-nm pump power.

The beam quality of the 450-nm wave remains good for increasing pump powers of both pump wavelengths, and the beam quality of the residual 1030–nm wave only slightly degrades. In contrast to this, the effect of pump depletion for the 799-nm wave is much stronger (see Figure 4.13b).
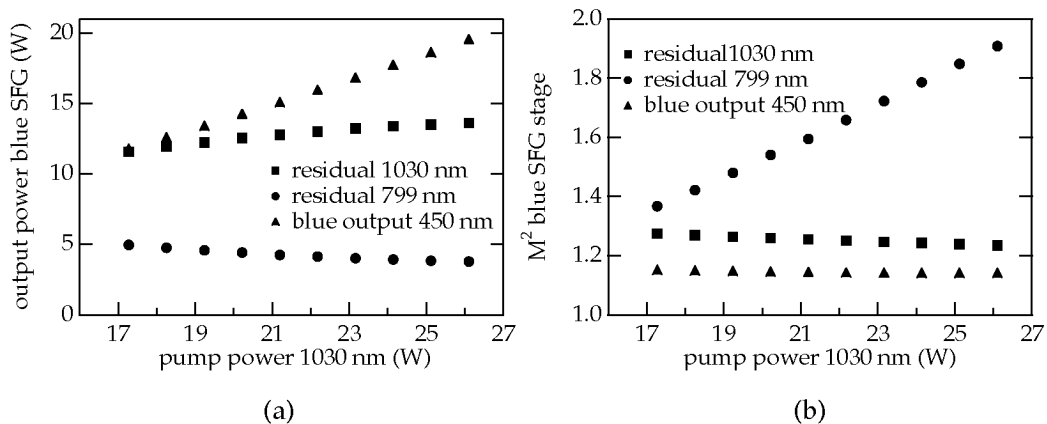
Figure 4.14: Dependence of the output power (a) and the beam quality (b) of the SFG stage for the generation of the blue beam on the 799-nm pump power.

This, however, is no problem since the residual of the 799-nm pump wave is not used for further conversion stages. The pulse length of the blue beam is relatively insensitive to the amount of pump power at 799 nm and 1030 nm.

Simulations show that higher conversion efficiency to the blue beam could be obtained with a shorter crystal and smaller pump beam radii. For example, using a 5-mm-long LBO crystal with a pump radius of 91 μm for the 1030-nm wave and 103 μm for the 799-nm wave would increase the amount of blue power by 20%, mainly because the influence of the GVM is reduced. Note that because of the short blue wavelength the GVM is much larger in the first SFG stage, compared to that in the infrared conversion stages. After a length of 10 mm, the total temporal walk-off between 1030-nm pump and the blue wave is 944 fs, what is almost the width of the pump pulse, which is simulated to be 1180 fs. The effect of the spatial walk-off, on the other hand, is not reduced for a shorter crystal, because stronger focusing is required. The simulations show signs of partial backconversion to the residual pump waves on the beam axis, but the beam quality of the generated blue beam is not yet negatively influenced.

Simulations for a situation with improved AR coatings (with an assumed reflectivity of 1% per surface for all wavelengths) result in 26% higher average

power of the blue beam. With a shorter 4-mm-long crystal and optimized mode radii, even 51% higher average power at 450 nm could be obtained. The blue average power would in this case be 18.9 W with still a good M^2 value of 1.15.

We now discuss the second SFG stage, i.e., the one for the generation of red light. Increasing the power of either pump beam separately does not increase the red output significantly (see Figure 4.15a). This indicates that the SFG process is strongly saturated, in spite of about 10 W of transmitted power at 1030 nm.
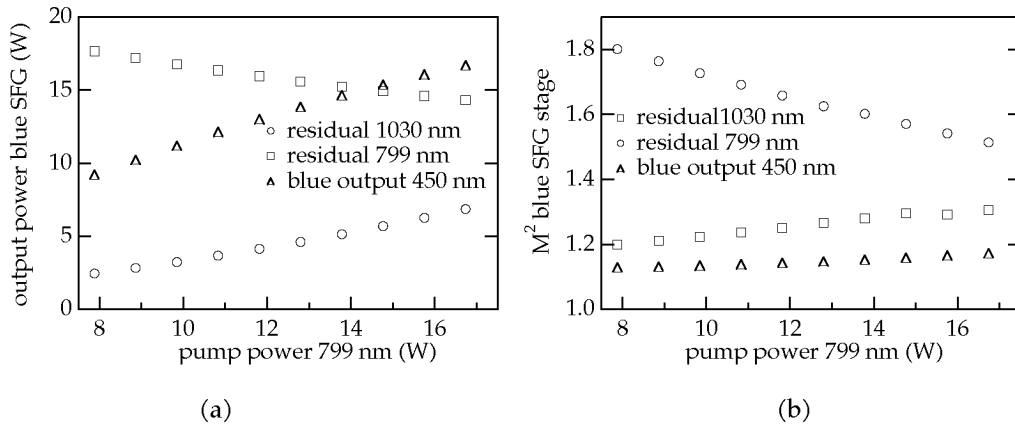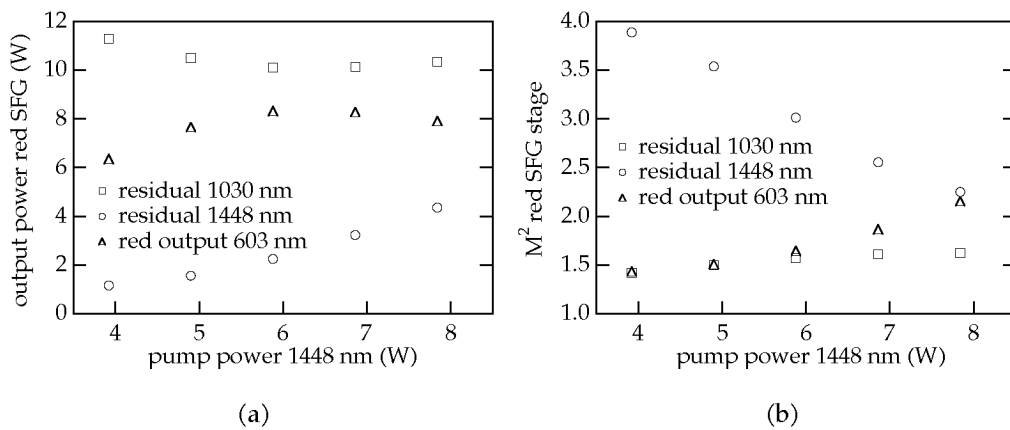

Figure 4.15: Dependence of the output power (a) and the beam quality (b) of the SFG stage for the generation of the red beam on the 1448-nm pump power.

The reason for this is that the 1030-nm pulse after the blue SFG stage is much longer than the 1448-nm pulse (see Figure 4.16), so they don't fully overlap. Note that the temporal walk-off between the 1030-nm wave and the 1448-nm pulse is only 13 fs after 15 mm and this strongly limits the fraction of pulse energy that can be converted. On the other hand, the effect of spatial walk-off is negligible in this stage.

Assuming better AR coatings with 1% reflection loss per surface for all wavelengths and also mode radii optimized for this situation, we would expect from simulations to obtain ≈10 W instead of 8.1 W in the red beam. Here, the simulated signal power from the OPA (also with optimized AR coatings) is 9.4 W (taking into account the losses in the AR coating in the blue SFM stage),

and the remaining power at 1030 nm for the red SFG stage is 15.2 W. The LBO crystal would have to be 12 mm long, and the pump radii required are 174 µm for 1030 nm and 1448 nm.
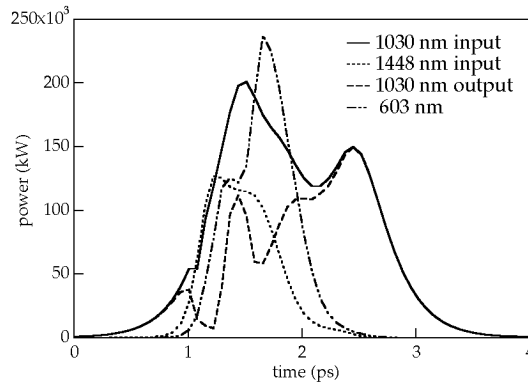
Figure 4.16: Simulated input (solid) and output (dashed) temporal pulse shape of the 1030-nm wave in the red SFG stage. The dotted line corresponds to the temporal pulse shape of the input 1448–nm wave and the dashed-dotted line to the generated red beam at 603 nm.

Another illustration of the problem of backconversion in the second SFG stage can be seen in the following Figures. The simulated near field fluence of the 1030-nm input pump wave in the SFG stage is shown in Figure 4.17.
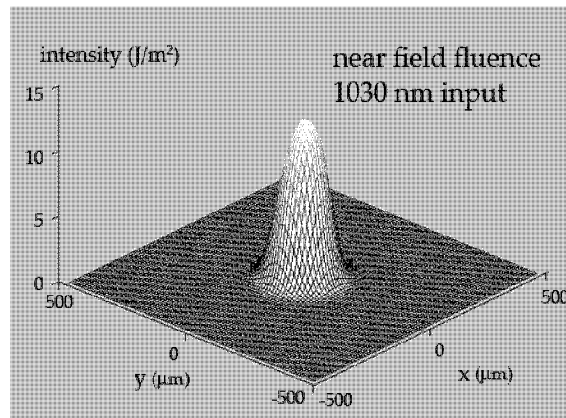
Figure 4.17: Simulated near field fluence in the x-t plane in the red SFG stage of the 1030 nm input wave.

Despite the temporal distortion of the input pulse (see Figure 4.18) we do not yet see strong distortion in the spatial profile (see Figure 4.17). Figure 4.18 shows the intensity distribution of the 1030-nm pump wave (before and after the conversion) together with the generated red beam at 603 nm. In this simulation, we show the intensity distribution on the beam axes in the time-position plane t-x (where y=0). It can be clearly seen, that the intensity distribution of the input beam (left graph in Figure 4.18) is temporally distorted. The sharp center peak in the intensity distribution of the residual pump pulse at 1030 nm (middle graph in Figure 4.18) is due to backconversion. The right graph in Figure 4.18 shows the generated red wave at 603 nm, which also shows temporal distortion.
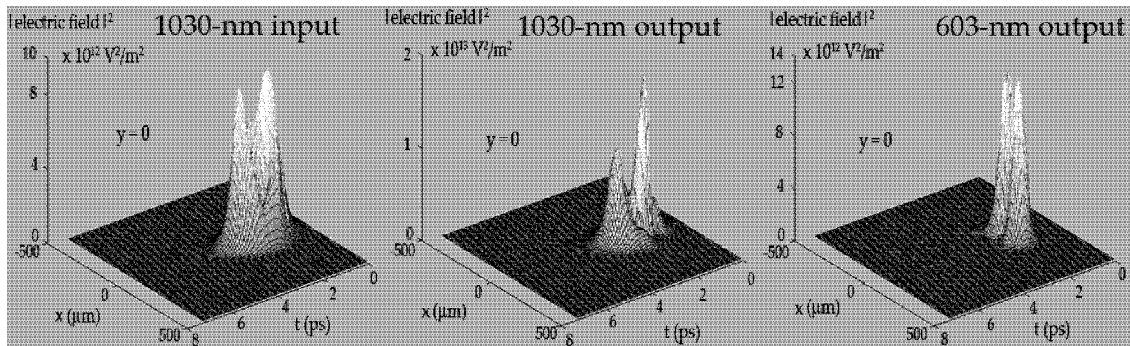
Figure 4.18: Simulated intensity distribution in the red SFG stage in the t-x plane, where y=0. The left graph represents the 1030 nm input wave, the middle graph the 1030 nm output wave and the right graph the generated red wave at 603 nm.

As the second SFG stage suffers from the temporal distortion of the 1030–nm light in the first SFG stage, one might consider using the two SFG stages in a parallel, i.e., with a beamsplitter to provide each SFG stage with a fraction of the total power of the original 1030-nm beam. Simulations showed that similar output powers in the red and blue could be obtained with such a configuration, but with somewhat deteriorated beam quality of the blue beam, because stronger focusing is required in the blue SFG stage, so that the spatial walk-off becomes more important. Moreover, one would need an additional adjustable delay line.

The wavelength of the red output is a bit shorter than the desired red (≥ 620 nm) for an RGB laser source (see Figure 4.19). This could in principle be solved with a new PPSLT crystal with poling period for a longer signal wavelength. One constraint imposed by our system is that the difference in photon energy between the blue and green colors equals the one between the green and red. For example, one could choose a red wavelength of 620 nm in combination with a blue wavelength of 440 nm by designing the poling period of the OPG for a signal wavelength of 1560 nm instead of 1448 nm. The other constraint in the OPG is the effect of group velocity mismatch that will (as numerical simulations show) deteriorate the conversion process if the signal wavelength is shifted to 1560 nm. For the original signal wavelength of 1448 nm, the group index of the pump wave lies between the indices of the signal and idler waves. This situation has been shown [82] to be ideal for the conversion efficiency. In contrast, a situation with signal and idler waves both propagating faster or slower than the pump wave will result in stronger saturation of the parametric gain. This exactly will be the case for a signal wavelength shifted to >1520 nm as then, the group index of the pump wave will be higher than the ones of signal and idler. This behavior of the group indexes is similar in other nonlinear materials such as KTP, RTA or LBO. Simulations predict that we could get the required performance from the OPG for a signal wavelength of up to ≈ 1510 nm. However, for an average signal power of 1.53 W in this situation we would already require a higher pump power of 9.5 W, as the parametric gain is reduced due to the enhanced GVM. With a signal wavelength of 1510 nm, we would obtain a red wavelength of 612 nm (still a bit short for displays) and a blue wavelength at 444 nm. It turns out that a laser wavelength of 1064 nm would actually lead to more favorable group velocities in the OPG stage even for optimum display wavelengths. However, our system requires relatively short pulses as we are using critical phase matching in several conversion stages, and so far there is no 1064-nm laser generating such pulses with sufficient peak power.

4.4 Discussion and outlook

We have carefully analyzed a powerful RGB laser system that in our experiments delivered 8 W at 603 nm (red), 23 W at 515 nm (green), and 10.1 W at 450 nm (blue) [9]. The system is based on the passively mode-locked Yb:YAG thin disk laser described in Section 3.2.4.2. A first key point for optimum performance of the chosen configuration of nonlinear conversion stages is that our laser produces sub-picosecond pulses and has thus a very high peak power that allows using critically phase-matched schemes for nonlinear conversion stages operating at room temperature. With e.g. ten times longer pulses from the laser, one would require noncritically phase-matched conversion stages to achieve efficient conversion, which (in case of LBO material) would then require several crystal ovens operated at elevated temperatures. High average power at 515 nm is crucial for the amount of power of the signal and idler waves generated in the OPA stage. At the same time, sufficient residual 1030–nm light with a good beam quality from the frequency doubler is required for the further conversion stages. An OPG stage based on PPSLT allows the generation of stable 1.6 W of signal power at 1.5 μm. With the recently demonstrated room temperature OPG based on MgO-doped SLT (see Section 5.2 and [74]), this last temperature-stabilized crystal can be replaced by an OPG with the same performance, but operated at room temperature. The power of the 799-nm pump light is crucial for a good conversion in the blue SFG stage, which is limited by GVM and spatial walk-off. The efficiency of the red SFG stage is limited by the temporal distortion of 1030-nm wave in the blue SFG stage. Because of this beam distortion and the available input powers, the red SFG stage works best if the blue SFG stage is not optimized for maximum blue output power. The detailed analysis showed that the overall performance of our system could not have been significantly improved with modified crystal lengths or focusing conditions, but better antireflection coatings could increase the output powers significantly. Note that the fabrication of these coatings is not trivial, particularly for the first (blue) SFG stage where four wavelengths are involved.

Assuming a reflectivity of the AR coatings of 1% per surface for all wavelengths, simulations predict the following performance (using the same

power from the laser, the frequency doubler and the OPG as in the experiment): The output of the OPA could be improved to 9.6 W of signal and 14.5 W of idler power. The OPA crystal length in this simulation was unchanged (10 mm), and the pump radii where 125 μm at 515 nm and 175 μm at 1448 nm, respectively. With beam radii of 330 μm at 1030 nm and 312 μm at 799 nm in the first SFG stage, a blue beam with an average power of 11.2 W at 450 nm with a good beam quality could be generated. The crystal length in this simulation was again unchanged (10 mm), only the focusing was weaker than for optimum blue light generation in order to obtain better performance in the following red stage. After the blue SFG stage, 17.2 W of residual 1030-nm light would be left as a first pump wave for the red SFG crystal. Finally, using a crystal with 12 mm length in the red SFG stage, a pump beam radius of 168 μm at 1030 nm and a pump beam radius of 173 μm for the signal wave from the OPA, a red beam at 603 nm with an average power of 12 W could be generated.

In an optimized configuration, the RGB laser system could generate a significantly higher total power of D65 (ISO 10526:1999/CIE S005/E-1998 standard) white light, which is an important parameter for an RGB laser source. With the above-mentioned powers and the wavelengths as generated in the experiment (603 nm, 515 nm, and 450 nm), the total D65 white light power would 37.5 W (12 W red, 16 W green and 9.5 W blue), corresponding to 11265 lm. The total conversion efficiency from the laser wavelength to D65 would be 47.5% and the total infrared to visible conversion efficiency would be 53%. The numerical analysis of the OPG stage showed that it is difficult to shift the signal wavelength to the desired value of 1560 nm in order to generate a red color at 620 nm. It turned out, however, that a signal wavelength of 1510 nm in the OPG should be possible, at least increasing the red wavelength by 10 nm to 612 nm. With improved wavelengths of 612 nm, 515 nm, and 445 nm, one could obtain 37.4 W of D65 power (12 W red, 16.6 W green and 8.8 W blue), assuming unchanged conversion efficiencies. The amount of D65 white light with optimized wavelength would be somewhat reduced, but the color gamut spanned by those optimized wavelengths would be larger. A laser wavelength of 1064 nm would actually make it easier to generate the optimum wavelengths for the display with optimum conversion efficiency, because the group velocities in the OPG stage would be more favorable for efficient conversion.

However, there currently exists no laser material at 1064 nm which is suitable for the generation of femtosecond pulses with high average output power.

The analyzed RGB system is unprecedented in terms of generated average powers in the colors as well as in its simplicity and practicability. One single laser oscillator without any amplifier stages provides the entire pump power of the system. The system does not require any synchronized cavities, and can be realized with room-temperature operation of all of the nonlinear crystals. Numerical simulations showed that improved AR coatings should allow achieving even better performance, with excellent conversion efficiency from infrared to D65, even though it is predicted that reaching a longer wavelength for the red output, as is desirable for displays, might be difficult. The previous point, among others, demonstrates that a careful investigation based on numerical simulations can greatly facilitate the physical understanding of device operation, optimization of device performance, and the identification of limitations.

4.5 Chromaticity chart

The color gamut is important for image projection and we therefore shortly review the definition of a chromaticity chart and compare a color gamut of the presented RGB laser source with the one from a standard high-definition TV.

Additive color mixing refers to the mixing of different colored beams by the superposition of so-called primaries. When this is done using red, green and blue primaries, the color yellow, cyan and magenta are produced in the overlap region of two primaries. The sensation of white is produced in the region where all the three primaries overlap with appropriate spectral distributions and intensities. In 1931 the Commission Internationale de l'Eclairage (CIE) developed a system based on three imaginary primaries called X, Y and Z, which are theoretically defined super-saturated colors. The imaginary primaries lie outside the bounds of the colored region called spectral locus (see Figure 4.19).

Every new color $C(\lambda)$ can be defined as a linear superposition of the imaginary primaries and weights called imaginary primary values X, Y and Z.

$$C(\lambda) = X \cdot \mathbf{X} + Y \cdot \mathbf{Y} + Z \cdot \mathbf{Z} \qquad (4.1)$$

The three-dimensional color space defined by the imaginary primary values X, Y and Z can be transformed into a two-dimensional chromaticity chart (see Figure 4.19). To do so, we define fractional components of the imaginary primary values x, y and z, which also are known as chromaticity coordinates. The chromaticity coordinates are normalized ($x+y+z=1$) and we therefore only need two of them to derive the third coordinate.

$$x = \frac{X}{X+Y+Z}, \quad y = \frac{Y}{X+Y+Z}, \quad z = \frac{Z}{X+Y+Z} \qquad (4.2)$$

As a result of this transformation, all the imaginary primary values can be represented in a two-dimensional graph (chromaticity chart, see Figure 4.19) of the two chromaticity coordinates x and y. However, by compressing the information in a two-dimensional chromaticity chart we loose information about the luminosity of the colors. A complete specification of colors using a chromaticity chart therefore requires two chromaticity coordinates and one of the imaginary primary values (*e.g.* x, y, $\mathbf{Z}$).
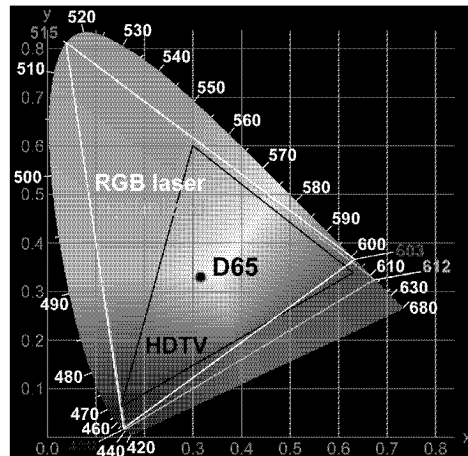
Figure 4.19: CIE 1931 Chromaticity chart with wavelengths marked around the spectral locus. The black line corresponds to a color gamut of a high-definition television (HDTV), the white line to the color gamut of the RGB laser source demonstrated in Section 4.4 and the yellow line to an RGB laser source with optimized wavelengths.

Figure 4.19 shows a chromaticity chart with the spectral locus in the plane of the chromaticity coordinates x and y. The color gamut is the range of colors that can be produced by a set of primary colors. The black triangle corresponds to the color gamut of a HDTV. The D65 white light illuminant (ISO 10526:1999/ CIE S005/E-1998 standard) has a spectral energy distribution closely matching the one from a blackbody at a temperature of 6500 K. As can be clearly seen in Figure 4.19, the color gamut of the RGB laser source presented in this Chapter (white line) is much wider than the one from a standard HDTV. Improved wavelengths in the red and blue color region (612 nm and 445 nm instead of 603 nm and 450 nm) would result in an even larger color gamut corresponding to the yellow triangle in the chromaticity chart.

Chapter 5

High Average Power
Nonlinear Optical Experiments

Passively mode-locked thin disk lasers with high average output powers and ultrashort pulse durations such as the Yb:YAG laser described in Section 3.2 constitute an excellent pump source for nonlinear devices. The high peak power of such lasers enables the generation of a very high parametric gain in nonlinear devices and therefore very efficient parametric frequency conversion. Such nonlinear devices can help to overcome the limitations set by the currently available gain materials for high power lasers.

A first limitation is the obtainable wavelength, which is typically around 1 μm for the currently available gain materials. We already have discussed in the previous Chapter that by employing nonlinear frequency conversion in $\chi^{(2)}$-active materials, the laser output of a thin disk laser at a wavelength of 1 μm can be efficiently converted to into the red, the green and the blue color region. In this Chapter, we address two more examples of high power frequency conversion applications such as a room temperature optical parametric generator (see Section 5.2) and a *fiber-feedback* optical parametric oscillator (see Section 5.3).

A second limitation set by the gain material is the achievable pulse duration, which is limited by the emission bandwidth of the gain material. This limitation too can be overcome with nonlinear devices and we will shortly

review in Section 5.4 how the pulse duration of 760 fs from the Yb:YAG thin disk laser can be externally reduced to 24 fs with nonlinear pulse compression in a microstructured fiber.

5.1 Periodically poled stoichiometric materials

Periodically poled stoichiometric materials such as lithium tantalate [77, 83] are very suitable materials for frequency conversion at high average power. The high power *fiber-feedback* OPO experiment presented in Section 5.3 is based on periodically poled stoichiometric $LiTaO_3$ (PPSLT) and the room temperature OPG experiment described in Section 5.2 uses a periodically poled MgO-doped stoichiometric $LiTaO_3$ crystal (PPMgSLT).

5.1.1 Periodically poled stoichiometric lithium tantalate

The photorefractive damage threshold of stoichiometric lithium tantalate (SLT) is more than two orders of magnitude higher [84] than in congruent lithium tantalate (CLT). In addition, the green induced infrared absorption in SLT was measured to be weaker than in CLT [84]. Moreover, domain switching in SLT can be realized with a much lower electric field than in conventional CLT. It has been reported in Ref. [77] that with a 13 times lower coercive field than in congruent materials (1.7 kV/mm), the poling of much thicker SLT samples becomes possible. Recently, the poling of 3–mm–thick samples has been demonstrated [84].

The PPSLT crystal we used for the *fiber-feedback* OPO (see Section 5.3) and for the RGB experiment (see Chapter 4) was fabricated in the National Institute for Material Science (Tsukuba, Japan) and the Research Institute of Electrical Communication (Tohoku, Japan). The crystal has a length of 17.5 mm and a thickness of 1 mm. The poling periods of the crystal are 28 μm and 29 μm and the phase-matching temperatures for the two grating periods are shown in Figure 5.1 (calculated with the Sellmeier equation for undoped stoichiometric $LiTaO_3$ [81]). The end faces of the crystal were polished but not coated, leading

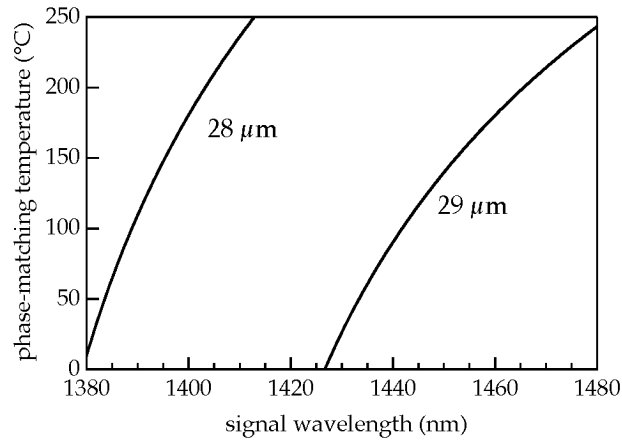to a reflectivity per surface of about $\approx$13% at a wavelength of 1030 nm for normal incidence.

Figure 5.1:   Calculated phase-matching temperatures of the PPSLT crystal as function of the signal wavelength (for grating periods 28 μm and 29 μm, and for a pump wavelength of 1030 nm).

5.1.2 Periodically poled MgO-doped stoichiometric lithium tantalate

Additional doping of stoichiometric lithium tantalate with a small amount of MgO allows reducing the sensitivity of the crystal to photorefractive damage. Recently, room-temperature operation of an OPO based on a 3-mm-thick PPMgSLT sample has been demonstrated [85]. We use in the OPG experiment a 30-mm-long PPMgSLT crystal with a poling period of 30 μm (see Figure 5.2). The thickness of the crystal is 1 mm and the end faces were polished but uncoated, leading to a reflectivity per surface of about $\approx$13% at a wavelength of 1030 nm for normal incidence.

The light-colored region in Figure 5.2 corresponds to the 2-mm-wide poled region of the PPMgSLT crystal. The white lines in the poled region correspond to damaged regions that occurred during the OPG experiment at the highest power level. Taking into account that the pump beam at 1030 nm propagated from the left side of the crystal to the right side, it is obvious that damage was

caused by the pump wave near the focal region and not by the generated signal wave.
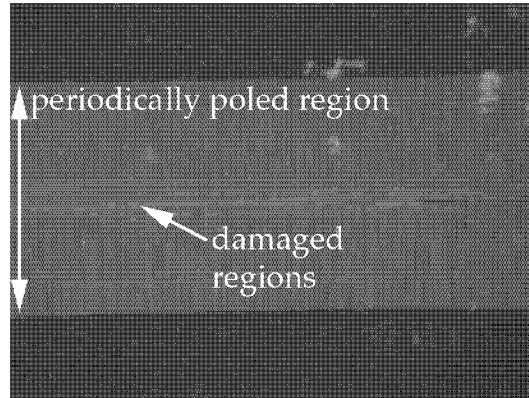

Figure 5.2:   Picture of the PPMgSLT after the OPG experiment. The white lines in the poled region (light colored region of the picture) correspond to damaged regions in the crystal.

5.2 Room temperature optical parametric generator

In this Section, we present the optical parametric generation in a periodically poled Mg:SLT (PPMgSLT) crystal, operated near room temperature without temperature stabilization.

Optical parametric generators (OPG) based on periodically poled ferroelectric crystals have been shown to be attractive sources of wavelength-tunable ultrashort pulses. Compared to synchronously pumped parametric oscillators, they are simpler and more robust, since synchronized cavities are not required. They do however require high pump pulse energies to exceed the threshold for parametric generation and must be operated with high parametric gain (order of 100 dB) for efficient conversion. Recent development of high average power passively mode-locked thin disk lasers allowed to reach this level of parametric gain without amplification of the laser pulses, so that a parametric generator can be driven at the full laser repetition rate of several tens of megahertz.

Single-pass femtosecond OPG at 35 MHz has previously been demonstrated in periodically poled lithium niobate (PPLN), where tunability of the signal output has been obtained in the broad range of 1.38-1.56 μm using different poling periods and crystal temperatures [78]. Pumped with 0.6-ps pulses from a passively mode-locked Yb:YAG thin disk laser at 1030 nm, the OPG generated pulses with a duration of 307 fs. The average signal power was limited to 0.5 W by damage of the congruent material. Better performance was later achieved using periodically poled stoichiometric lithium tantalate (PPSLT), which has a higher damage threshold [79]. In that experiment, 300-fs pulses at 1030 nm from a passively mode-locked Yb:KYW thin disk laser [53] were used at a repetition rate of 24 MHz, yielding stable 1 W average signal power in 320-fs pulses. Compared to stoichiometric $LiNbO_3$ (SLN), the lower coercive field of stoichiometric $LiTaO_3$ (SLT) allows high quality domain switching even in thicker crystals [77]. This makes it a favorable material for femtosecond high power applications, where large mode areas are required to avoid crystal damage. In another approach, 7-ps pulses from an 82-MHz oscillator-amplifier system were used to generate 6.3 W of average signal power in a PPLN crystal [80]. Here the use of longer pulses allowed efficient conversion and higher average pump power at moderate peak intensities inside the crystal. To avoid photorefractive damage, the crystals in all the mentioned experiments were operated at an elevated temperature in temperature-stabilized ovens. This elevated temperature has long been a requirement for periodically poled crystals, adding complexity to the otherwise simple setup of an OPG. Higher resistance to photorefractive damage and green-induced infrared absorption has been observed and investigated in MgO-doped SLN (Mg:SLN) [86, 87] and more recently, efficient optical parametric oscillation could be demonstrated at room temperature in MgO-doped SLT (Mg:SLT) [12].

5.2.1 Experimental setup

Pumped with 6.4 W from a passively mode-locked Yb:YAG thin disk laser at 1030 nm, the OPG delivers stable 1.5 W average signal power at 1484 nm using the full laser repetition rate of 59 MHz. The idler wavelength (not measured) is 3.37 μm, and some green light at 515 nm arises from fourth-order phase-matched second-harmonic generation. With higher pump power (7.7 W),

we achieved even 2.4 W of signal power for a few minutes, before damage occurred.

We used a laser setup similar to the one described in Section 3.2.4.2. The laser generated up to 50 W of average output power in 725-fs pulses. After passing a variable attenuator and a Faraday isolator (see Figure 5.3), the pump beam was focused to a 34-μm radius inside the 30-mm long PPMgSLT crystal. The uncoated crystal has a thickness of 1 mm and an MgO doping concentration of 1 mol. %. The periodically poled region is 2 mm wide and consists of a single 30-μm poling period (see Figure 5.2). The crystal is mounted onto a copper heat sink for passive cooling.
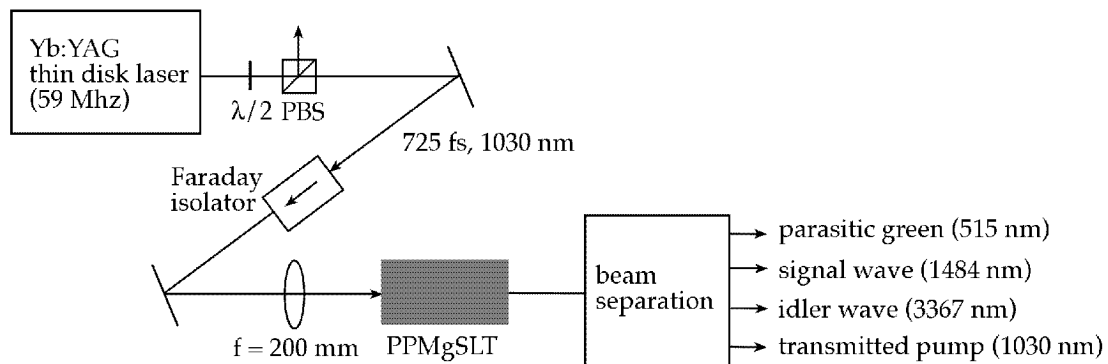
Figure 5.3: Experimental setup of the OPG (not to scale). $\lambda/2$, half-wave plate; PBS, polarizing beam splitter; PPMgSLT, periodically poled MgO-doped LiTaO$_3$ crystal.

5.2.2 Results

Pumped with 6.4 W incident on the entrance face, we obtained 1.5 W average signal power and 0.6 W idler power. At this power level, the OPG operated stably with a calculated pump peak intensity of 6.3 GW/cm^2 inside the crystal, assuming no significant conversion at the position of the focus. The parasitic green light had an average power of 0.18 W. The total conversion efficiency from pump to signal and idler is 33%. Taking into account the losses due to Fresnel reflections at the crystal's uncoated entrance and exit faces, the total internal conversion efficiency is 43%. Here we used a reported Sellmeier

equation for undoped SLT [81] to calculate the reflection losses for the various wavelengths.

Figure 5.4 shows the measured average output powers of signal and idler and the transmitted pump power as function of the incident pump power. Opened or closed symbols correspond to measurements with the beam at two different transverse positions in the crystal, because damage occurred within a few minutes at the first position at an average signal power of 1.75 W, where the corresponding peak pump intensity inside the crystal was 6.6 GW/cm^2. We believe that the pump (and not the signal or idler) intensity is relevant for damage, since damage was observed near the beam focus (see Figure 5.2), where signal and idler powers are still rather small. In the second measurement, 2.4 W of signal and 1 W of idler power were reached with an incident pump power of 7.7 W. This translates to a total conversion efficiency of 43%, while the total internal conversion efficiency is 58%.
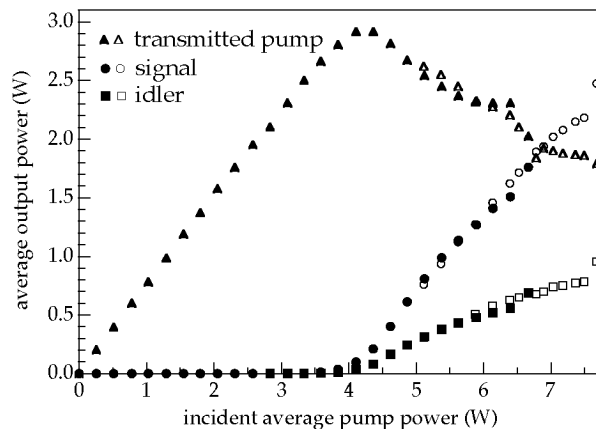
Figure 5.4:   Average output powers of signal, idler and transmitted pump versus average pump power incident on the crystal. Filled and open symbols correspond to two measurements at different crystal positions.

At 1.5 W of average signal power, the triangular shape of the measured intensity autocorrelation indicates a distortion of the temporal pulse shape (see Figure 5.5). This is due to the combined action of pump depletion and temporal walk-off between the pump and signal pulse resulting from the group velocity

mismatch (GVM) inside the PPMgSLT crystal (see below). At 0.6 W average signal power the distortions are not yet observed and we obtained a FWHM pulse duration of 0.62 ps using a sech^2 fit. With a FWHM spectral bandwidth of 5.6 nm the time-bandwidth product is 0.47. At 1.1 W of average signal power, the influence of GVM on the temporal pulse shape starts to become visible in the autocorrelation. Here we estimated (again with a sech^2 fit) a pulse duration of 0.8 ps. The spectral bandwidth was 4.9 nm, leading to a time-bandwidth product of 0.53. Using a knife-edge method, we measured the beam quality at average signal powers of 0.6 W, 1.1 W, and 1.5 W with resulting M^2 values of 1.25, 1.4, and 1.6, respectively. This reduction in beam quality with increasing conversion efficiency is typical for high gain optical parametric systems [76].

We further investigated the influence of the GVM on the temporal pulse shape using an advanced numerical simulation model, which takes into account the full spatial and temporal nature of the nonlinear interaction and exact dispersion [11]. To simulate the quantum noise, from which the OPG starts, the model uses signal and idler inputs with numerically generated fluctuations. The GVM automatically enters the model by using the Sellmeier equations from Ref. [81] to calculate the wavelength dependencies of the refractive index.

Best agreement with the experiment was achieved using an effective nonlinearity of $d_{\text{eff}} = 9.65$ pm/V for the first, and $d_{\text{eff}} = 10$ pm/V for the second position in the crystal at which the measurements were made. This is close to the value of 10 pm/V from Ref. [12] for second-harmonic generation from 1064 nm to 532 nm. The influence of the GVM on the amplification process depends on the relative walk-off of the signal and idler with respect to the pump. Neglecting conversion, a pump and signal pulse simultaneously entering the crystal would exit the crystal with a time separation of ≈2.5 ps due to the GVM of ≈83 fs/mm. With the wavelengths we use, the signal and idler walk off in opposite directions relative to the pump. This is a favorable condition that allows high gain even if the walk-off time for linear pulse propagation is longer than the pulse length [82]. In the regime with low conversion, the strong temporal gain guiding by the pump pulse can produce high-quality signal and idler pulses, which overlap well with the pump pulse.

When the pump pulse becomes depleted, its peak will shift in time, and resulting change of the temporal gain guiding can distort the generated pulses.
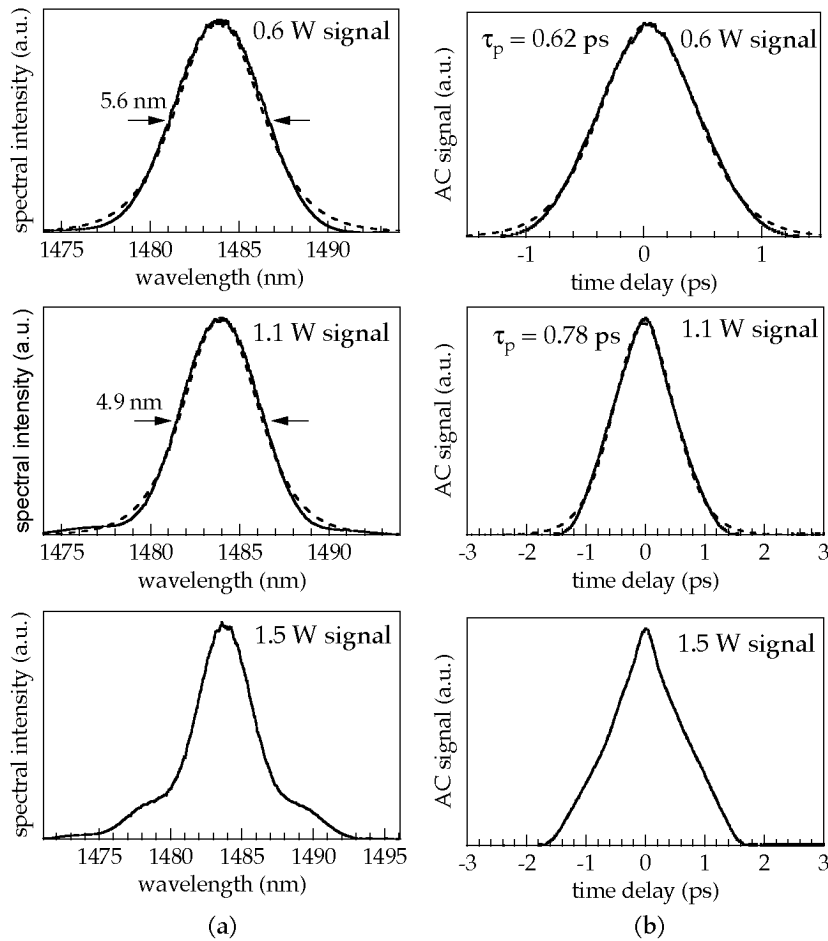
Figure5.5:   Optical spectrum (a) and intensity autocorrelation (b) of the measured signal pulses for 0.6 W, 1.1 W and 1.5 W of average signal output power.

In Figure 5.6, this is demonstrated using the signal pulses retrieved from the simulation at average signal output powers of 0.6 W, 1.1 W and 1.5 W. The intensity autocorrelations calculated from these pulses show good qualitative agreement with the measured intensity autocorrelations in Figure 5.5b.

For even higher pump power, backconversion can cause further distortion and finally, these effects lead to two distinct peaks in the temporal pulse profile

when simulating the highest experimentally achieved average signal power of 2.4 W (see Figure 5.7).
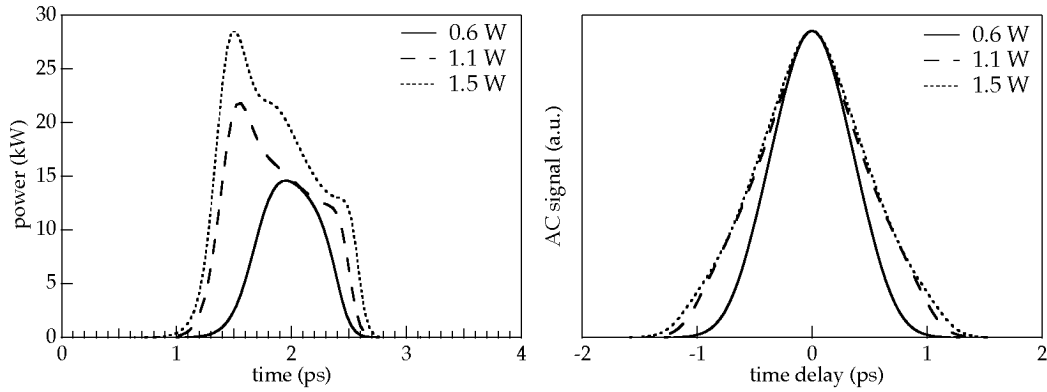
Figure 5.6:   Time-dependent power (left) and autocorrelation signal (right) of the pulses retrieved from simulations with average signal output powers of 0.6 W (solid), 1.1 W (dashed) and 1.5 W (dotted). The temporal distortion leads to a triangularly shaped intensity autocorrelation.
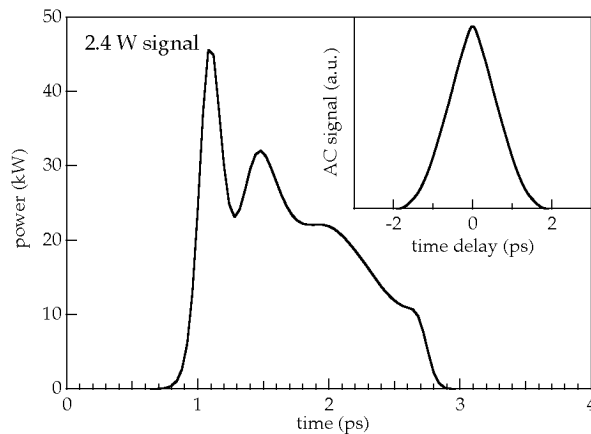
Figure 5.7:   The temporal pulse shape of the simulated signal pulse at 2.4 W average signal power shows two distinct peaks. The shape of the intensity autocorrelation (inset) characteristic for such a pulse was also observed in the experiment.

Using a shorter crystal would reduce the influence of the GVM and allow for better temporal pulse shape. However, the higher intensities required would result in crystal damage and simulations using a 25-mm-long crystal

have shown that equivalent conversion could not be achieved even with tighter focusing. Hence the use of relatively long crystals appears to be the only feasible solution to achieve sufficient gain for high conversion in a femtosecond OPG, despite the significant temporal walk-off.

We have demonstrated stable and efficient room temperature femtosecond optical parametric generation with high average signal output power of 1.5 W at the full laser repetition rate of 59 MHz. The resulting pulses have pulse durations similar to the pump pulse despite the influence of the GVM. This result will in particular allow the construction of an RGB system similar to the one presented in Chapter 4, but with all nonlinear crystals operated near room temperature. The system will then not require any temperature-stabilized oven, which constitutes a further simplification and a significant step towards a commercially feasible high power RGB source.

5.3 High power fiber-feedback optical parametric oscillator

Optical parametric generators (OPGs) probably are the most compact and simple sources for the generation of wavelength-tunable ultashort pulses, but in contrast to optical parametric oscillators (OPOs), they require a very high parametric gain to excess the threshold for optical parametric generation and therefore tend to suffer from crystal damage. Recently, Südmeyer et al. demonstrated what is believed to be the first *fiber-feedback* OPO, a novel type of synchronously pumped OPO [78]. In this device a single-mode fiber represents most of the OPO cavity length. Although the fiber feedback introduces substantial losses (mainly at the fiber launch), high conversion efficiency can be achieved by employment of a high parametric gain and strong output coupling directly after the nonlinear crystal. Additional intra-cavity losses then only weakly influence the generated power. This concept led to compact, stable, and efficient systems in the femtosecond and picosecond regimes [78]. The femtosecond versions are unusually insensitive to drifts of the OPO cavity length and do not require active stabilization.

The consequence of the feedback through the single-mode fiber is that the required gain in a *fiber-feedback* OPO is significantly lower than the gain needed for parametric generators and therefore the intensities inside the nonlinear crystal can be reduced well below the damage threshold. In this Section, we review a recently demonstrated high-power version of a *fiber-feedback* OPO with up to 19 W of signal power in femtosecond pulses in the 1.5 μm spectral region [88].

5.3.1 Experimental setup

The *fiber-feedback* OPO (see Figure 5.8) described in this Section is based on a 17.5-mm-long PPSLT crystal pumped with up to 58 W at 1030 nm from a passively mode-locked thin disk Yb:YAG laser, which is similar to the one described in Chapter 3.2.4.2. The pump beam radius inside the 1-mm-thick PPSLT crystal is 160 μm in the horizontal and 130 μm in the vertical direction. The calculated parametric gain is 60 dB. The crystal is operated at 150 °C to avoid photorefractive damage. The poling period is 29 μm, leading to a signal wavelength of 1.448 μm (for 150 °C). For simplicity we used an uncoated crystal and accepted the relatively high reflection losses (13% per surface). The different wavelength components are separated with dichroic mirrors (M_3–M_7). The power levels of the remaining pump and idler waves were slightly corrected for transmission losses in the dichroic mirrors (transmission of idler mirror M_3, 95%; transmission of residual pump mirror M_4, 94.5%). Only a weak reflection (4% of the power) from an uncoated glass substrate is used for the signal feedback, while the transmission (92%) of this glass substrate represents the signal output. The feedback light at 1.448 μm is launched into a 2.6-m-long large mode area fiber [89] that is single mode at the signal wavelength (the mode area in the fiber is 436 μm^2).

The dispersion of the fiber is determined mainly by the material dispersion of fused silica; the zero-dispersion wavelength is 1.3 μm. The light emerging from the fiber is mode-matched with lenses f_2 and f_3 and fed back into the crystal through dichroic mirror M_2, which is highly reflective for the pump wave and transmissive at the signal wavelength. The repetition rate of the OPO

cavity is matched to the pump laser. The propagation in the fiber corresponds to 71% of the total optical path for one round-trip.
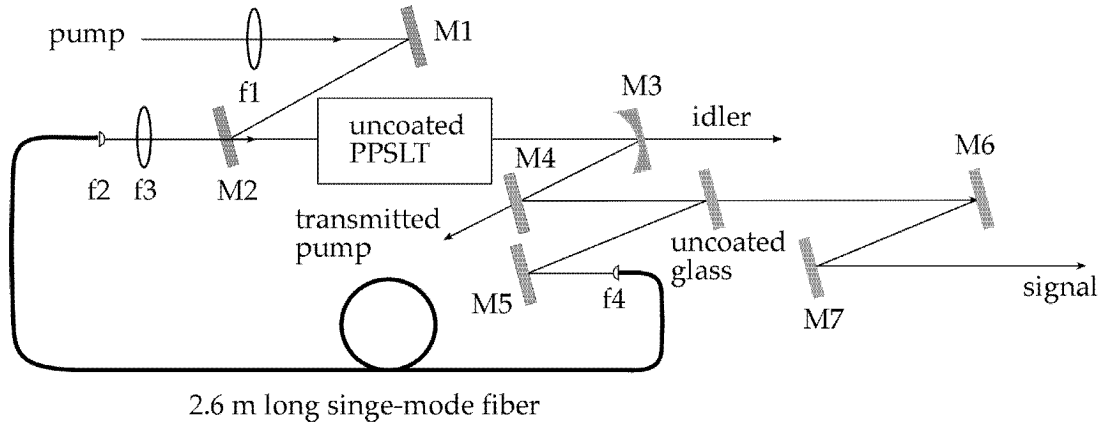
Figure5.8:   Setup of the OPO ring cavity. M_1–M_7, mirrors; f_1–f_4, lenses; PPSLT, crystal of periodically poled stoichiometric LiTaO$_3$.

5.3.2 Results

We obtained up to 19 W of average signal power at 1.448 μm for a pump power of 58 W incident on the crystal (Figure 5.9). We would expect to obtain even higher signal powers by reducing the losses of several non-optimized optical components. In particular, an antireflection coating on the PPSLT crystal would greatly reduce the losses; it would basically remove 14% of pump losses at the crystal input face and a similar amount of signal loss at the exit face. Also, the transmission of the output coupler could be optimized. In addition, we would expect to obtain wavelength tuning by changing the operating temperature of the PPSLT crystal in a certain wavelength range. The change in wavelength at the operating point of the OPO would be 0.23 nm/K.
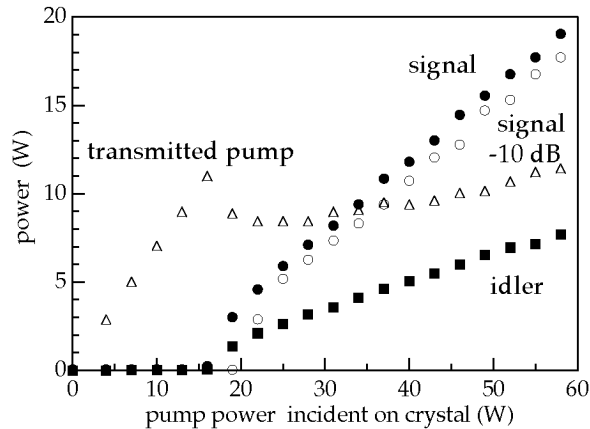
Figure 5.9:   Signal power without attenuator (filled circles), signal power with additional 10-dB attenuator (open circles), idler power (filled rectangles), and power of the transmitted pump (open triangles) versus pump power.

The duration of the signal pulses was measured by intensity autocorrelation. Assuming a $sech^2$ pulse shape, the pulse duration (FWHM) is typically near 840 fs (Figure 5.10). The width of the optical spectrum is approximately 3.3 nm (FWHM), leading to a time–bandwidth product of 0.4.

Figure 5.10:   Left, measured intensity autocorrelation (solid line) of the signal wave with 19-W average power. The dashed curve represents the $sech^2$ fit with a pulse duration of 840 fs. Right, measured optical spectrum.

One of the main advantages of such a *fiber-feedback* OPO is the unusual insensitivity to adjustment of the cavity length: the cavity length can be varied over a range of 0.4 mm (corresponding to more than one pulse width), while the output power is reduced by less than 10% (Figure 5.11). Over this range, the ce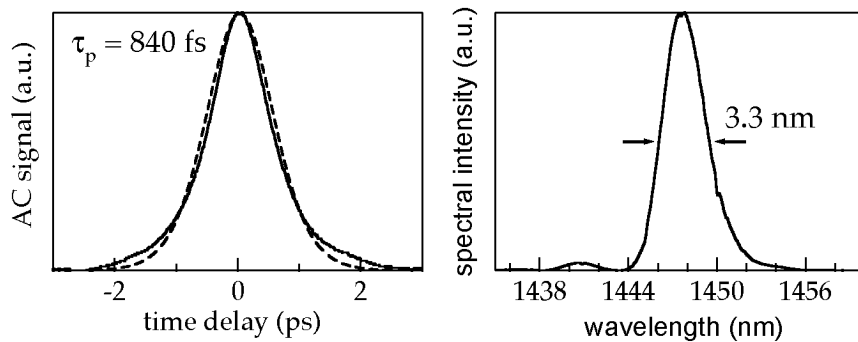ntral wavelength changes only slightly from 1447.9 nm for a shorter cavity to 1447.5 nm for a longer cavity (with a FWHM bandwidth varying in the range 3.3–3.8 nm). The pulse duration changes from 650 fs (for a shorter cavity) to 940 fs. Therefore, stable operation over hours is achieved without the need for active cavity length stabilization.
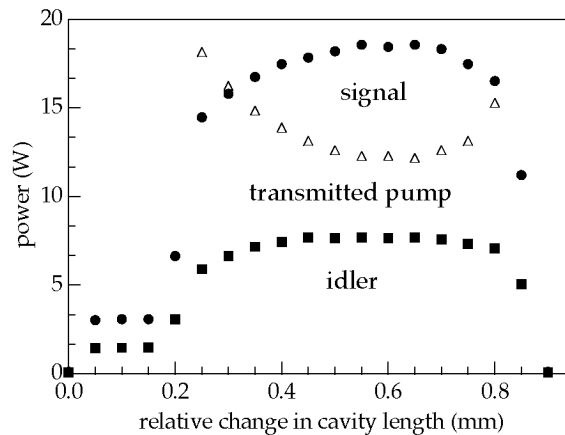
Figure 5.11: Average output power of the signal (filled circles), idler (filled rectangles), and transmitted pump (open triangles) as functions of the relative change of the cavity length.

In addition, the *fiber-feedback* OPO is very insensitive to cavity losses in the feedback loop: when an additional attenuator with 10-dB loss was inserted in front of the fiber launch (between $M5$ and $f4$), the maximum signal output power was reduced by less than 5%. It is important to note that the phase-matching bandwidth of the crystal is significantly smaller than the pulse bandwidth. This, however, poses no problem in the high gain regime, where even a temporally stretched signal pulse is compressed again by the action of the temporally limited gain. Also important to note is that the small phase-matching bandwidth explains the weak dependence of the signal wavelength on the cavity length.

Recently it has been found that high gain OPOs operated with very high peak powers and high conversion efficiency cannot provide a perfect transverse beam quality of the output beams [76]. This is because gain guiding leads to a reduced mode size of the signal beam near the end of the crystal, where most of the power conversion occurs (see Chapter 4.2). The small signal beam area results in backconversion occurring in the center of the transverse profile in situations with strong saturation as is necessary for good conversion. The OPO described here is already operating in this regime. Nevertheless, the transverse beam quality factor M^2 of the signal beam has been measured to be 1.6 at full power, i.e., not too far from the diffraction limit. For a reduced pump power of 37 W and 10.5 W of signal output power, we measured the M^2 value to be below 1.3. After the fiber of the feedback loop, the average power of the feedback signal was measured to be 90 mW at full power. This leads to only moderate nonlinear phase shifts in the large mode area fiber. With a standard telecom fiber we would expect significant nonlinear phase shifts, but numerical simulations indicated no strong effect of these phase shifts on the OPO performance.

5.4 Nonlinear pulse compression at high average power

Although the available average powers from passively mode-locked thin disk lasers generating pulses with a few-hundred femtoseconds have been scaled to very high average output powers, there is a lack of gain materials for generating similar powers in the sub-100-fs regime. To further reduce the pulse duration of a high power femtosecond laser, the well-known pulse compression technique using a nonlinear fiber and a prism compressor has recently been applied for the first time at such high power levels [90]. The use of a large mode area microstructured fiber allowed us to overcome limitations arising from the high peak intensity when operating at such power levels. Pulses with a duration of 810-fs were compressed to 33 fs (FWHM) which resulted in a peak power of 12 MW. The result was achieved using 38 W of average power from a 34-MHz passively mode-locked thin disk laser (such as the one presented in

Section 3.2.4.1), while the compressed output pulses had an average power of 18 W.

The higher output power available from our passively mode-locked thin disk laser now allowed us to significantly increase the average output power and peak power of the compressed pulses. The increased intensities enabled us to use shorter fiber samples, which allowed better compensation of the material dispersion and resulted in significantly shorter pulses.

In this Section, we shortly review the latest result of 32 W of average power in 24-fs-pulses at a pulse repetition rate of 57 MHz. The main pulse carries 0.41 µJ of energy with a peak power of 16 MW [91]. We used a large mode area (LMA) microstructured fiber with a mode area of $\approx 200~\mu m^2$ and a length of 14.3 cm for the spectral broadening, while two SF10 prisms were used in a double-pass configuration to remove the resulting chirp and compress the pulses.

5.4.1 Setup

The pump source used for the experiment the Yb:YAG thin disk laser presented in Section 3.2.4.2 emitting 80 W of average output power at a wavelength of 1030 nm. It is passively mode-locked using a semiconductor saturable absorber mirror (SESAM) [6, 7] and generates nearly transform-limited soliton pulses with a pulse duration of 760 fs at a pulse repetition rate of 57 MHz and excellent beam quality ($M^2 < 1.1$).

After the output coupler we use a set of polarizing optics to adjust the power incident on the fiber and to control the input polarization. A Faraday isolator is used to avoid residual reflections from the fiber face back into the laser cavity. The first half-wave plate ($\lambda/2$ #1) shown in Figure 5.12 is used for the power adjustment, while the second half-wave plate ($\lambda/2$ #2) allows to change the polarization incident on the fiber. We use two focusing lenses to control waist size and position of the focus. The LMA fiber used has a mode radius of $\approx 8~\mu m$ and thus an effective mode area of $\approx 200~\mu m^2$. For an incident average power of up to 60 W launched onto the fiber input we found an optimum fiber length of 14.3 cm. We removed the fiber's polymer jacket to

prevent damage by absorption of light launched into the fiber cladding. Due to the strict single-mode guidance of the fiber, bending of the short fiber sample is not required for single-mode operation.
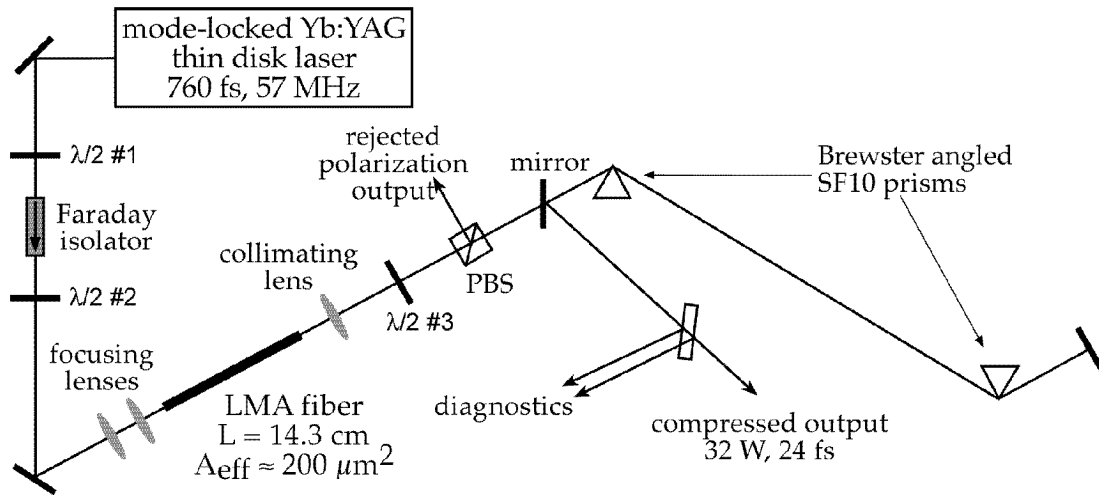

Figure 5.12: Experimental setup (not to scale). PBS, polarizing beam splitter; $\lambda/2$, half-wave plates; LMA, large mode area fiber.

After the fiber output, a third lens is used to collimate the beam, while the following half wave-plate ($\lambda/2$ #3) and polarizing beam splitter define a linear polarization state of the fiber output. A pair of Brewster-angled SF10 prisms is used to linearly compress the spectrally broadened pulses. The pulses are extracted from the prism compressor on a mirror by introducing a small vertical offset for the beam traveling in the backward direction. The wedged glass plate allows beam extraction for diagnostics.

5.4.2 Results

We measured 32 W of average power in the output using launched power of up to 60 W and a launch efficiency around 70%, whilst 10 W was rejected by the polarizing beam splitter after the third half-wave plate ($\lambda/2$ #3). The optical spectrum of the output spans the range 970 to 1090 nm (Figure 5.13, left). Assuming a flat phase, the calculated FWHM pulse duration of this spectrum would be 20 fs.

The prism compressor was optimized for shortest pulse duration of the compressed pulses, which we characterized using the pulse retrieval technique "phase and intensity from correlation and spectrum only" (PICASO) [92]. For this retrieval algorithm, the optical spectrum and autocorrelation trace are used as input along with the autocorrelation of the pulses after propagation through an element with known dispersion. On the right of Figure 5.13 the measured autocorrelation trace is shown (solid line) along with the autocorrelation of the pulse retrieved by the algorithm (dashed line), which are in excellent agreement.
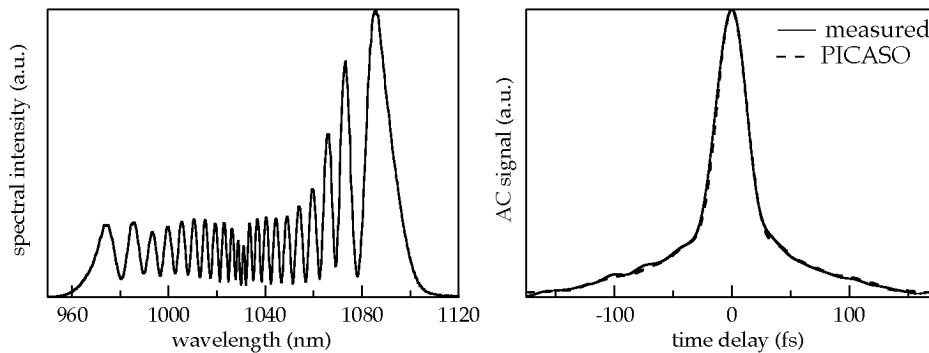
Figure 5.13: Measured optical spectrum (left) and autocorrelation trace (right, solid line) at 32 W of average output power. Autocorrelation trace of pulses retrieved by the PICASO algorithm (right, dashed line).

The output pulse is shown in Figure 5.14. The main pulse carries 73% of the total pulse energy ($E_{p'} = 0.56$ µJ) and has a FWHM duration of 24 fs, which corresponds to 1.2 times the transform-limited pulse duration calculated from the spectrum. It therefore has a pulse energy of 0.41 µJ and a peak power of 16 MW, corrected for energy in pedestals. The pedestals are caused by third-order dispersion, which is not compensated in our experiment. Compared to previous results we have been able to significantly increase the average power and the peak power of the compressed pulses to 32 W and 16 MW respectively [91].
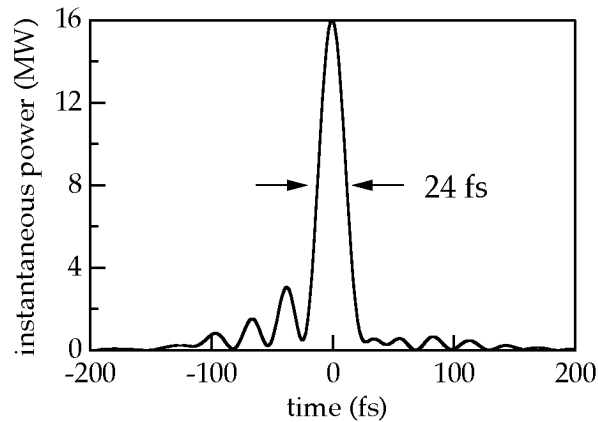
Figure 5.14: Pulse retrieved by the PICASO algorithm from the measured data at 32 W average output power (Figure 5.13). The main pulse carries 73% of the total energy. It has a FWHM duration of 24 fs and a peak power of 16 MW.

The maximum average power in the compression experiment currently is limited by fiber damage. Newest experiments have shown that we have bulk damage in the fiber and to overcome this damage problem we need large mode area fibers with even larger effective mode areas that the 200 μm^2 used in this experiment. In addition to their large effective mode area, the fibers have to provide strictly single transverse mode propagation even in very short fiber pieces in the order of 10 cm. With even higher peak powers from such compression experiments many applications such as waveguide writing and experiments in strong field physics may appear feasible. Examples for applications in strong field physics are high harmonic generation [93, 94, 95], above threshold ionization [96, 97], or laser plasma generated X-rays [98].

Chapter 6

Conclusion and Outlook

In this thesis, we have described the development of a passively mode-locked Yb:YAG thin disk laser with a record high average output power and its application as pump source for nonlinear optical devices, in particular for a high average power red-green-blue (RGB) laser source suitable for image projection.

The generation of femtosecond pulses with very high average powers poses numerous challenges that have to be faced. Arguably the biggest one is the thermal load in the gain material that can be drastically reduced by choosing a suitable gain material. We have chosen Yb:YAG because of its low quantum defect, good thermal conductivity and simple electronic structure. In addition, the bandwidth of Yb:YAG supports sub-picosecond pulse durations which makes it very attractive for high power femtosecond lasers.

Another crucial aspect for reducing the thermal load in the gain material is its geometry. The concept of a passively mode-locked thin disk laser is perfectly suited for femtosecond high power lasers. The gain material in this concept typically has a thickness on the order of 100 μm and is attached directly to a heat sink for cooling. The disk is used in reflection and its rear side is coated for high reflectivity for pump and laser wavelengths. As the radius of the pump beam on the disk is much larger than its thickness, the heat flow is nearly one-dimensional and its direction is parallel to the propagation direction in the laser cavity. The consequences of this special geometry are only weak thermal

lensing and aberrations and therefore this concept allows for high power diffraction-limited laser operation, a prerequisite for passive mode locking. The heat flow in the SESAM also is nearly one-dimensional as its substrate is thin compared to the laser mode radius. Therefore, the combination of a thin disk laser head with a SESAM turned out to be a power-scalable concept for passive mode locking and achieving femtosecond pulses [8].

Despite the power-scalability of the thin disk laser concept, the scaling of the average power of a femtosecond laser is a demanding task as there are numerous challenges that have to be overcome. The laser cavity has to be carefully designed to fulfill the boundary conditions for mode locking and to minimize the thermal problems in the intra-cavity components. The process of soliton mode locking requires a balance between self phase modulation (SPM) and negative group delay dispersion (GDD). We used the following two approaches for dispersion compensation: (i) A Gires-Tournois interferometer (GTI), which allowed for the generation of tunable pulses in the picosecond range, and (ii) dispersive mirrors, which made the generation of femtosecond pulses possible. The performance and stability of the laser containing dispersive mirrors was better because they introduced weaker thermal lenses than the GTI. However, dispersive mirrors too show some thermal lensing and typically have a lower damage threshold than standard high reflective mirrors. Those issues have to be considered in the cavity design and careful experimental optimization is required for the maximum performance of the laser.

We demonstrated a mode-locked Yb:YAG thin disk laser generating tunable pulses with 6-24 ps duration with up to 60 W of average power at a pulse repetition rate of 34 MHz. We in addition presented an Yb:YAG laser with 80 W of average power in 705 fs pulses at a pulse repetition rate of 57 MHz. Today (Mai 2005), these results set the standard in the field of high power picosecond and femtosecond solid-state lasers.

There in only a very limited number of gain materials suitable for high average power femtosecond lasers and thus there are limits in terms of the accessible wavelengths and pulse durations. The Yb:YAG thin disk laser constitutes an excellent pump source for nonlinear optical devices manly

because of its high peak power which allows for very efficient nonlinear frequency conversion in critically phase-matched nonlinear crystals.

As a first example for nonlinear frequency conversion we presented an RGB laser source for projection displays pumped by the Yb:YAG thin disk laser. There is a variety of configurations of nonlinear conversion stages which can be used to generate the visible beams required for an RGB laser source (see e.g. Ref. [73]). A thorough comparison of different configurations is rather difficult as it depends on the imposed constraints such as the required output powers and beam qualities. Also, beside the output power, there exists a great variety of other parameters to optimize, such as the number of required nonlinear crystals, required crystal ovens and temperature acceptance, just to name a few. We have provided a detailed analysis including advanced numerical simulations [11] for one configuration, which appears particularly attractive in various respects. The RGB system is unprecedented in terms of the generated average powers in the colors as well as in its simplicity and practicability. One single laser oscillator without any amplifier stages provides the entire pump power of the system. The system does not require any resonant cavities, and only one of the nonlinear crystals has to be temperature-stabilized. The RGB laser source simultaneously generates average powers of 8 W at 603 nm, 23 W at 515 nm, and 10.1 W at 450 nm. Numerical simulations have shown that improved AR coatings of the nonlinear crystals and slightly optimized focusing conditions and crystal lengths in the conversion stages should allow achieving even better performance of greater than 11 W per color, resulting in a color balanced output of 37.5 W of D65 white light.

A prerequisite for an RGB laser source operated at room temperature is an optical parametric generator (OPG) with high average power and stable long-term operation at room temperature. The recent fabrication improvements of periodically poled MgO-doped LiTaO$_3$ have enabled us to demonstrate such a room temperature OPG. This device generates up to 2.4 W of average signal power at a wavelength of 1.484 μm. Stable long-term OPG operation with 1.5 W of average power has been obtained, which would enable us to build a room temperature RGB laser source. Even higher average powers of signal and idler waves can be obtained with a *fiber-feedback* optical parametric oscillator (OPO).

A *fiber-feedback* OPO is a synchronously pumped high gain OPO with resonant feedback of the signal wave trough a single mode fiber. Compared to synchronously pumped low gain OPOs, a *fiber-feedback* OPO exhibits a number of attractive properties such as a compact setup, low sensitivity to cavity losses and low sensitivity against drifts in the cavity length. We have demonstrated a *fiber-feedback* OPO with an average signal power of 19 W at a wavelength of 1,448 μm.

The obtainable pulse duration of mode-locked lasers is limited by the emission bandwidth of the gain material. We have reported on external nonlinear pulse compression in a large mode area microstructured fiber, which allows increasing the optical bandwidth through self phase modulation in the fiber and removing the resulting chirp with pair of prisms. We obtained a compressed output of 32 W of average power with 24 fs FWHM duration, corresponding to a peak power of 16 MW at the full laser repetition rate of 57 MHz. Such high peak powers are particularly interesting for applications in strong field physics.

Promising future projects may include the scaling of the average output power of the compression experiment and increasing of the pulse energy of thin disk lasers. Including multiple passes of the laser cavity through the thin disk in combination with an increased transmission of the output coupler should allow to increase the pulse energy of a thin disk laser while retaining the intra-cavity power at a level the current dispersive mirrors can stand.

References

1. T. H. Maiman, "Stimulated optical radiation in ruby," *Nature* **187**, 493 (1960).

2. R. J. Keyes, and T. M. Quist, "Injection luminescent pumping of $CaF_2:U^{3+}$ with GaAs diode lasers," *Appl. Phys. Lett* **4**, 50 (1964).

3. R. L. Byer, "Diode Laser-Pumped Solid-State Lasers," *Science* **239**, 742 (1988).

4. A. E. Siegman, *Lasers* (University Science Books, Mill Valley, California, 1986)

5. A. Giesen, H. Hügel, A. Voss, K. Wittig, U. Brauch, and H. Opower, "Scalable Concept for Diode-Pumped High-Power Solid-State Lasers," *Appl. Phys. B* **58**, 363 (1994).

6. U. Keller, D. A. B. Miller, G. D. Boyd, T. H. Chiu, J. F. Ferguson, and M. T. Asom, "Solid-state low-loss intracavity saturable absorber for Nd:YLF lasers: an antiresonant semiconductor Fabry-Perot saturable absorber," *Opt. Lett.* **17**, 505 (1992).

7. U. Keller, K. J. Weingarten, F. X. Kärtner, D. Kopf, B. Braun, I. D. Jung, R. Fluck, C. Hönninger, N. Matuschek, and J. Aus der Au, "Semiconductor saturable absorber mirrors (SESAMs) for femtosecond to nanosecond pulse generation in solid-state lasers," *IEEE J. Sel. Top. Quantum Electron.* **2**, 435 (1996).

8. J. Aus der Au, G. J. Spühler, T. Südmeyer, R. Paschotta, R. Hövel, M. Moser, S. Erhard, M. Karszewski, A. Giesen, and U. Keller, "16.2 W average power from a diode-pumped femtosecond Yb:YAG thin disk laser," *Opt. Lett.* **25**, 859 (2000).

9. F. Brunner, E. Innerhofer, S. V. Marchese, T. Südmeyer, R. Paschotta, T. Usami, H. Ito, S. Kurimura, K. Kitamura, G. Arisholm, and U. Keller, "Powerful red-green-blue laser source pumped with a mode-locked thin disk laser," *Opt. Lett.* **29**, 1921 (2004).

10. E. Innerhofer, F. Brunner, S. V. Marchese, G. Arisholm , R. Paschotta, T. Usami, H. Ito, S. Kurimura, K. Kitamura, and U. Keller, "Analysis of nonlinear wavelength conversion system for a red-green-blue laser projection source," *submitted to JOSA B*, (2005).

11. G. Arisholm, "Quantum noise initiation and macroscopic fluctuations in optical parametric oscillators," *J. Opt. Soc. Am. B* **16**, 117 (1999).

12. N. E. Yu, S. Kurimura, Y. Nomura, M. Nakamura, and K. Kitamura, "Efficient optical parametric oscillation based on periodically poled 1.0 mol % MgO-doped stoichiometric $LiTaO_3$," *Appl. Phys. Lett.* **85**, 5134 (2004).

13.   D. Grischkowsky, and A. C. Balant, "Optical pulse compression based on enhanced frequency chirping," *Appl. Phys. Lett.* **41**, 1 (1982).

14.   C. V. Shank, R. L. Fork, R. Yen, R. H. Stolen, and W. J. Tomlinson, "Compression of femtosecond optical pulses," *Appl. Phys. Lett.* **40**, 761 (1982).

15.   T. Südmeyer, F. Brunner, E. Innerhofer, R. Paschotta, K. Furusawa, J. C. Baggett, T. M. Monro, D. J. Richardson, and U. Keller, "Nonlinear femtosecond pulse compression at high average power levels by use of a large area holey fiber," *Opt. Lett.* **28**, 1951 (2003).

16.   G. H. C. New, "Pulse evolution in mode-locked quasi-continuous lasers," *IEEE J. Quantum Electron.* **10**, 115 (1974).

17.   H. A. Haus, "Theory of Mode Locking with a Slow Saturable Absorber," *IEEE J. Quantum Electron.* **11**, 736 (1975).

18.   H. A. Haus, "Theory of modelocking with a fast saturable absorber," *J. Appl. Phys.* **46**, 3049 (1975).

19.   H. A. Haus, J. G. Fujimoto, and E. P. Ippen, "Structures for additive pulse modelocking," *J. Opt. Soc. Am. B* **8**, 2068 (1991).

20.   O. E. Martinez, R. L. Fork, and J. P. Gordon, "Theory of passively modelocked lasers for the case of a nonlinear complex propagation coefficient," *J. Opt. Soc. Am. B* **2**, 753 (1985).

21.   F. X. Kärtner, I. D. Jung, and U. Keller, "Soliton Modelocking with Saturable Absorbers," *IEEE J. Sel. Topics in Quantum Electron.* **2**, 540 (1996).

22.   I. D. Jung, F. X. Kärtner, L. R. Brovelli, M. Kamp, and U. Keller, "Experimental verification of soliton modelocking using only a slow saturable absorber," *Opt. Lett.* **20**, 1892 (1995).

23.   R. Paschotta, and U. Keller, "Passive mode locking with slow saturable absorbers," *Appl. Phys. B* **73**, 653 (2001).

24.   E. G. Arthurs, D. J. Bradley, and A. G. Roddie, "Buildup of picosecond pulse generation in passively mode-locked rhodamine dye lasers," *Appl. Phys. Lett.* **23**, 88 (1973).

25.   J. P. van der Ziel, W. T. Tsang, R. A. Logan, R. M. Mikulyak, and W. M. Augustyniak, "Subpicosecond pulses from passively modelocked GaAs buried optical guide semiconductor lasers," *Appl. Phys. Lett.* **39**, 525 (1981).

26.   Y. Silberberg, P. W. Smith, D. J. Eilenberger, D. A. B. Miller, A. C. Gossard, and W. Wiegmann, "Passive modelocking of a semiconductor diode laser," *Optics Letters* **9**, 507 (1984).

27.   R. Häring, R. Paschotta, A. Aschwanden, E. Gini, F. Morier-Genoud, and U. Keller, "High–power passively mode–locked semiconductor lasers," *IEEE J. Quantum Electron.* **38**, 1268 (2002).

28. A. Aschwanden, D. Lorenser, H. J. Unold, R. Paschotta, E. Gini, and U. Keller, "2.1-W picosecond passively mode-locked external-cavity semiconductor laser," *Opt. Lett.* **30**, 272 (2005).

29. K. J. Blow, and D. Wood, "Modelocked lasers with nonlinear external cavities," *J. Opt. Soc. Am B* **5**, 629 (1988).

30. E. P. Ippen, H. A. Haus, and L. Y. Liu, "Additive Pulse Modelocking," *J. Opt. Soc. Am. B* **6**, 1736 (1989).

31. D. E. Spence, P. N. Kean, and W. Sibbett, "60-fsec pulse generation from a self-mode-locked Ti:sapphire laser," *Opt. Lett.* **16**, 42 (1991).

32. T. Brabec, C. Spielmann, P. F. Curley, and F. Krausz, "Kerr lens modelocking," *Opt. Lett.* **17**, 1292 (1992).

33. M. Piché, and F. Salin, "Self-mode locking of solid-state lasers without apertures," *Opt. Lett.* **18**, 1041 (1993).

34. U. Morgner, F. X. Kärtner, S. H. Cho, Y. Chen, H. A. Haus, J. G. Fujimoto, E. P. Ippen, V. Scheuer, G. Angelow, and T. Tschudi, "Sub-two-cycle pulses from a Kerr-lens mode-locked Ti:sapphire laser," *Opt. Lett.* **24**, 411 (1999).

35. D. H. Sutter, G. Steinmeyer, L. Gallmann, N. Matuschek, F. Morier-Genoud, U. Keller, V. Scheuer, G. Angelow, and T. Tschudi, "Semiconductor saturable-absorber mirror-assisted Kerr-lens mode-locked Ti:sapphire laser producing pulses in the two-cycle regime," *Opt. Lett.* **24**, 631 (1999).

36. L. R. Brovelli, U. Keller, and T. H. Chiu, "Design and Operation of Antiresonant Fabry-Perot Saturable Semiconductor Absorbers for Mode-Locked Solid-State Lasers," *J. Opt. Soc. Am. B* **12**, 311 (1995).

37. U. Keller, in *Nonlinear Optics in Semiconductors* E. Garmire, A. Kost, Eds. (Academic Press, Inc., Boston, 1999), **59**, 211.

38. M. Haiml, U. Siegner, F. Morier-Genoud, U. Keller, M. Luysberg, R. C. Lutz, P. Specht, and E. R. Weber, "Optical nonlinearity in low-temperature grown GaAs: microscopic limitations and optimization strategies," *Appl. Phys. Lett.* **74**, 3134 (1999).

39. M. Haiml, U. Siegner, F. Morier-Genoud, U. Keller, M. Luysberg, P. Specht, and E. R. Weber, "Femtosecond response times and high optical nonlinearity in Beryllium doped low-temperature grown GaAs," *Appl. Phys. Lett.* **74**, 1269 (1999).

40. C. Hönninger, R. Paschotta, F. Morier-Genoud, M. Moser, and U. Keller, "Q-switching stability limits of continuous-wave passive mode locking," *J. Opt. Soc. Am. B* **16**, 46 (1999).

41. A. Nebel, B. Ruffing, and R. Wallenstein, "A high power diode-pumped all-solid-state RGB laser source," in Conference of Lasers and Electro-Optics (CLEO 1998), Vol. 6 of OSA Technical Papers Series (Optical Society of America, Washington D.C., 1998), Postdeadline Paper CPD3, 1998.

42. R. Wallenstein, "Advanced solid state sources for high power visible light generation," in Technical Digest of Conference on Lasers and Electro-Optics (Optical Society of America, Washington, DC, 2001), paper CThC3, 2001.

43. J. Limpert, T. Clausnitzer, A. Liem, T. Schreiber, H.-J. Fuchs, H. Zellmer, E.-B. Kley, and A. Tünnermann, "High-average-power femtosecond fiber chirped-pulse amplification system," *Opt. Lett* **28**, 1984 (2003).

44. M. Karszewski, U. Brauch, K. Contag, S. Erhard, A. Giesen, I. Johannsen, C. Stewen, and A. Voss, "100 W TEM$_{00}$ Operation of Yb:YAG Thin Disc Laser with High Efficiency," in Advanced Solid State Lasers, Vol. XIX of OSA Technical Digest Series (Optical Society of America, Washington D. C., 1998), p. 296, 1998.

45. Y. Jeong, J. K. Sahu, D. N. Payne, and J. Nilsson, "Ytterbium-doped large-core fiber laser with 1.36kW continous-wave output power," *Opt. Express* **12**, 6088 (2004).

46. P. Peuser, and N. P. Schmitt, *Diodengepumpte Festkörperlaser* (Springer-Verlag, 1994)

47. W. Koechner, *Solid-State Laser Engineering.* A. L. Schawlow, A. E. Siegman, T. Tamir, H. K. V. Lotsch, Eds., Springer Series in Optical Sciences (Springer-Verlag, Heidelberg, Germany, 1996), vol. 1.

48. W. Koechner, "Thermal lensing in a Nd:YAG laser rod," *Appl. Opt.* **9**, 2548 (1970).

49. M. Stalder, M. Bass, and B. H. T. Chai, "Thermal quenching of fluorescence in chromium-doped fluoride laser crystals," *J. Opt. Soc. Am. B* **9**, 2271 (1992).

50. L. D. DeLoach, S. A. Payne, L. L. Chase, L. K. Smith, W. L. Kway, and W. F. Krupke, "Evaluation of Absorption and Emission Properties of Yb Doped Crystals for Laser Applications," *IEEE J. Quantum Electron.* **29**, 1179 (1993).

51. X. Zou, and H. Toratani, "Evaluation of spectroscopic properties of Yb-doped glasses," *Phys. Rev. B* **52**, 15889 (1995).

52. P. Klopp, V. Petrov, and U. Griebner, "Potassium Ytterbium Tungstate Provides the Smallest Laser Quantum Defect," *Jpn. J. Appl. Phys.* **42**, 246 (2003).

53. F. Brunner, T. Südmeyer, E. Innerhofer, R. Paschotta, F. Morier-Genoud, J. Gao, K. Contag, A. Giesen, V. E. Kisel, V. G. Shcherbitsky, N. V. Kuleshov, and U. Keller, "240-fs pulses with 22-W average power from a mode-locked thin-disk Yb:KY(WO$_4$)$_2$ laser," *Opt. Lett.* **27**, 1162 (2002).

54. P. Klopp, V. Petrov, U. Griebner, K. Petermann, V. Peters, and G. Erbert, "Highly efficient mode-locked Yb:Sc$_2$O$_3$ laser," *Opt. Lett* **29**, 391 (2004).

55. U. Griebner, V. Petrov, K. Petermann, and V. Peters, "Passively mode-locked Yb:Lu$_2$O$_3$ laser," *Opt. Express* **12**, 3125 (2004).

56. C. Hönninger, R. Paschotta, M. Graf, F. Morier-Genoud, G. Zhang, M. Moser, S. Biswal, J. Nees, A. Braun, G. A. Mourou, I. Johannsen, A. Giesen, W. Seeber, and U. Keller, "Ultrafast ytterbium-doped bulk lasers and laser amplifiers," *Appl. Phys. B* **69**, 3 (1999).

57. A. Giesen, private communication (2001).

58. R. Adair, L. L. Chase, and S. A. Payne, ""Nonlinear refractive index of optical crystals"," *Phys. Rev. B* **39**, 3337 (1989).

59. V. Magni, "Multielement stable resonators containing a variable lens," *J. Opt. Soc. Am. A* **4**, 1962 (1987).

60. F. X. Kärtner, and U. Keller, "Stabilization of soliton-like pulses with a slow saturable absorber," *Opt. Lett.* **20**, 16 (1995).

61. D. Kopf, G. J. Spühler, K. J. Weingarten, and U. Keller, "Mode-locked laser cavities with a single prism for dispersion compensation," *Appl. Opt.* **35**, 912 (1996).

62. F. Gires, and P. Tournois, "Interferometre utilisable pour la compression d'impulsions lumineuses modulees en frequence," *C. R. Acad. Sci. Paris* **258**, 6112 (1964).

63. F. Brunner, R. Paschotta, J. Aus der Au, G. J. Spühler, F. Morier-Genoud, R. Hövel, M. Moser, S. Erhard, M. Karszewski, A. Giesen, and U. Keller, "Widely tunable pulse durations from a passively mode-locked thin disk Yb:YAG laser," *Opt. Lett.* **26**, 379 (2001).

64. R. Paschotta, J. Aus der Au, G. J. Spühler, S. Erhard, A. Giesen, and U. Keller, "Passive mode locking of thin disk lasers: effects of spatial hole burning," *Appl. Phys. B* **72**, 267 (2001).

65. A. Giesen, U. Brauch, I. Johannsen, M. Karszewski, C. Stewen, and A. Voss, "Diode Pumped Thin Disk High Power Yb Lasers," in CLEO/Europe Technical Digest, 1996 OSA Technical Digest Series (Optical Society of America, Washington D. C., 1996), invited paper CML1, 1996.

66. S. Erhard, K. Contag, I. Johannsen, M. Karszewski, T. Rupp, C. Stewen, and A. Giesen, "Novel pump design of Yb:YAG thin disc laser for operation at room temperature with improved efficiency," in Advanced Solid State Lasers, Vol. XXVI of OSA Technical Digest Series (Optical Society of America, Washington D. C., 1999), p. 38, 1999.

67. T. Y. Fan, and R. L. Byer, "Modelling and CW Operation of a Quasi-Three-Level 946 nm Nd:YAG Laser," *IEEE J. Quantum Electron.* **23**, 605 (1987).

68. T. Kasamatsu, and H. Sekita, "Laser-diode-pumped Nd:YAG active-mirror laser," *Appl. Opt.* **36**, 1879 (1997).

69. K. Contag, M. Karszewski, C. Stewen, A. Giesen, and H. Hugel, "Theoretical modelling and experimental investigations of the diode-pumped thin-disk Yb:YAG laser," *Quantum Electron.* **29**, 697 (1999).

70. E. Innerhofer, T. Südmeyer, F. Brunner, R. Häring, A. Aschwanden, R. Paschotta, U. Keller, C. Hönninger, and M. Kumkar, "60 W average power in picosecond pulses from a passively mode-locked Yb:YAG thin-disk laser," in Conference on Laser and Electro-Optics CLEO 2002, Talk CTuD4, 2002.

71. D. Lee, and P. F. Moulton, "High-efficiency, high-power, OPO-based RGB source," in Technical Digest of Conference on Lasers and Electro-Optics (Optical Society of America, Washington, DC, 2001), paper CThJ2, 2001.

72. E. Innerhofer, T. Südmeyer, F. Brunner, R. Häring, A. Aschwanden, R. Paschotta, U. Keller, C. Hönninger, and M. Kumkar, "60 W average power in 810-fs pulses from a thin-disk Yb:YAG laser," *Opt. Lett.* **28**, 367 (2003).

73. R. Wallenstein, US patent US005828424, "Process Apparatus for generating at least three beams of different wavelength for the display of color video pictures", (1998).

74. S. V. Marchese, E. Innerhofer, R. Paschotta, S. Kurimura, K. Kitamura, G. Arisholm, and U. Keller, "Room temperature femtosecond optical parametric generation in MgO-doped stoichiometric $LiTaO_3$," *submitted to Opt. Lett.*, (2005).

75. D. A. Roberts, "Simplified Characterization of Uniaxial and Biaxial Nonlinear Optical Crystals: A Plea for Standardization of Nomenclature and Conventions," *IEEE J. Quantum Electron.* **28**, 2057 (1992).

76. G. Arisholm, T. Südmeyer, and R. Paschotta, "Limits to the power scalability of high-gain optical parametric oscillators and amplifiers," *J. Opt. Soc. Am. B* **21**, 578 (2004).

77. K. Kitamura, Y. Furukawa, K. Niwa, V. Gopalan, and T. E. Mitchell, "Crystal growth and low coercive field 180° domain switching characteristics of stoichiometric $LiTaO_3$," *Appl. Phys. Lett.* **73**, 3073 (1998).

78. T. Südmeyer, J. Aus der Au, R. Paschotta, U. Keller, P. G. R. Smith, G. W. Ross, and D. C. Hanna, "Novel ultrafast parametric systems: high repetition rate single-pass OPG and fibre-feedback OPO," *J. Phys. D: Appl. Phys.* **34**, 2433 (2001).

79. T. Südmeyer, F. Brunner, R. Paschotta, U. Keller, T. Usami, H. Ito, M. Nakamura, and K. Kitamura, "Femtosecond Optical Parametric Generation (OPG) in Periodically Poled Stoichiometric $LiTaO_3$ with >1 W Average Power," in Conference on Laser and Electro-Optics CLEO 2002, Talk CTuO4, 2002.

80. B. Köhler, U. Bäder, A. Nebel, J.-P. Meyn, and R. Wallenstein, "A 9.5-W 82-MHz-repetition-rate picosecond parametric optical parametric generator with cw diode laser injection seeding," *Appl. Phys. B* **75**, 31 (2002).

81. A. Bruner, D. Eger, M. B. Oron, P. Blau, M. Katz, and S. Ruschin, "Temperature-dependent sellmeier equation for the refractive index of stoichiometric lithium tantalate," *Opt. Lett.* **28**, 194 (2003).

82. R. Danielius, A. Piskarskas, A. Stabinis, G. P. Banfi, P. D. Trapani, and R. Righini, "Traveling-wave parametric generation of widely tunable, highly coherent femtosecond light pulses," *J. Opt. Soc. Am. B* **10**, 2222 (1993).

83. T. Hatanaka, K. Nakamura, T. Taniuchi, H. Ito, Y. Furukawa, and K. Kitamura, "Quasi-phase matched optical parametric oscillation with periodically poled stoichiometric LiTaO$_3$," *Opt. Lett.* **25**, 651 (2000).

84. M. Nakamura, S. Takekawa, K. Terabe, K. Kitamura, T. Usami, K. Nakamura, H. Ito, and Y. Furukawa, "Near-stoichiometric LiTaO$_3$ for bulk quasi-phase-matched devices," *Ferroelectrics* **273**, 199 (2002).

85. K. Kitamura, N. A. Yu, M. Nakamura, and S. Kurimura, "2x2x35L mm3 rod-type periodically-poled 1.0 mol% MgO-doped stoichiometric LiTaO3 for optical parametric oscillation," in Technical Digest of Advanced Solid State Photonics (Optical Society of America, Washington, DC, 2004), paper PD10, 2004.

86. Y. Furukawa, K. Kitamura, S. Takekawa, K. Niwa, and H. Hatano, "Stoichiometric Mg:LiNbO$_3$ as an effective material for nonlinear optics," *Optics Lett.* **23**, 1892 (1998).

87. Y. Furukawa, K. Kitamura, A. Alexandrovski, R. K. Route, M. M. Fejer, and G. Foulon, "Green-induced infrared absorption in MgO doped LiNbO$_3$," *Appl. Phys. Lett.* **78**, 1970 (2001).

88. T. Südmeyer, E. Innerhofer, F. Brunner, R. Paschotta, U. Keller, T. Usami, H. Ito, M. Nakamura, K. Kitamura, and D. C. Hanna, "High power femtosecond fiber-feedback OPO based on periodically poled stoichiometric LiTaO$_3$," *Opt. Lett.* **29**, 1111 (2004).

89. N. G. R. Broderick, H. L. Offerhaus, D. J. Richardson, and R. A. Sammut, "Power scaling in passively mode-locked large-mode area fiber lasers," *IEEE Photonics Technol. Lett.* **10**, 1718 (1998).

90. T. Südmeyer, F. Brunner, E. Innerhofer, R. Paschotta, K. Furusawa, J. C. Baggett, T. M. Monro, D. J. Richardson, and U. Keller, "Nonlinear femtosecond pulse compression at high average power levels using a large mode area holey fiber," *Opt. Lett.* **28**, 951 (2003).

91. E. Innerhofer, F. Brunner, S. V. Marchese, R. Paschotta, U. Keller, K. Furusawa, J. C. Baggett, T. M. Monro, and D. J. Richardson, "32 W of average power in 24-fs pulses from a passively mode-locked thin disk laser with nonlinear fiber compression," in Advanced Solid-State Photonics, talk TuA3, 2005.

92. J. W. Nicholson, J. Jasapara, W. Rudolph, F. G. Omenetto, and A. J. Taylor, "Full-field characterization of femtosecond pulses by spectrum and cross-correlation measurements," *Opt. Lett.* **24**, 1774 (1999).

93. M. Ferray, A. L'Huillier, X. F. Li, L. A. Lompré, G. Mainfray, and C. Manus, "Multiple-harmonic conversion of 1064 nm radiation in rare gases," *J. Phys. B: At. Mol. Opt. Phys.* **21**, L31 (1988).

94. P. Salières, and M. Lewenstein, "Generation of ultrashort coherent XUV pulses by harmonic conversion of intense laser pulses in gases: towards attosecond pulses," *Meas. Sci. Technol.* **12**, 1818 (2001).

95. A. McPherson, G. Gibson, H. Jara, U. Johann, T. S. Luk, I. McIntyre, K. Boyer, and C. K. Rhodes, "Studies of multiphoton production of vacuum-ultraviolet radiation in the rare gases," *J. Opt. Soc. Am. B* **4**, 595 (1987).

96. G. G. Paulus, W. Nicklich, H. Xu, P. Lambropoulos, and H. Walther, "Plateau in above threshold ionization spectra," *Phys. Rev. Lett.* **72**, 2851 (1994).

97. R. Wiehle, B. Witzel, H. Helm, and E. Cormier, "Dynamics of strong-field above-threshold ionization of argon: Comparison between experiment and theory," *Phys. Rev. A* **67**, 063405 (2003).

98. M. M. Murnane, H. C. Kapteyn, M. D. Rosen, and R. W. Falcone, "Ultrafast X-Ray Pulses from Laser-Produced Plasmas," *Science* **251**, 531 (1991).

Curriculum Vitæ

Personal Data

Name:	Edith Innerhofer
Date of birth:	March 16, 1975
Nationality:	Swiss, Italian

Education

Since 01/2001	Ph.D. studies in the group of Prof. Dr. Ursula Keller, Physics Department/Institute of Quantum Electronics, ETH Zürich, Switzerland.
10/2000	Master of science in physics ("Diplom"), ETH Zurich, (Switzerland).
10/1995 – 10/2000	Studies in physics, ETH Zurich, (Switzerland).

Research experience

04/2000 – 08/2000	Master thesis at the Physics Department/Institute of Quantum Electronics, ETH Zürich, Switzerland (Mode-locked $Yb:KGd(WO_4)_2$ lasers)
07/1999 – 08/1999	Semester project at the Physics Department/Institute of Quantum Electronics, ETH Zürich, Switzerland (Diode-pumped $Yb:Yb^{3+}Ca_4O(BO_3))_3$ laser)

Awards and Honors

02/2005	ASSP 2005 Best Student Paper Prize

Danksagung

Ich möchte mich an dieser Stelle bei allen Kolleginnen und Kollegen bedanken, die zum Erfolg dieser Doktorarbeit beigetragen haben. Ohne ihre tatkräftige Unterstützung wäre die vorliegende Arbeit nicht möglich gewesen. Im besonderen gilt mein Dank:

Prof. Dr. Ursula Keller für die Möglichkeit, dass ich in ihrer Gruppe die Doktorarbeit auf einem solch interessanten Gebiet durchführen konnte und für ihre Unterstützung.

PD Dr. Rüdiger Paschotta für die ausgezeichnete Betreuung dieser Doktorarbeit, sowohl in fachlichen wie auch menschlichen Aspekten und für die äusserst angenehme Art und Weise, mit welcher er die All-Solid-State Gruppe leitet.

Prof. Dr. Tilman Esslinger für die Bereitschaft, das Korreferat zu dieser Doktorarbeit zu übernehmen.

Dr. Clemens Hönninger, Dr. Malte Kumkar und Dr. Dirk Sutter von der Firma TRUMPF-Laser GmbH in Schramberg, Deutschland für die Leihe des Yb:YAG Scheibenlaserkopfes und ihre wiederholt tatkräftige Unterstützung bei der Lösung von technischen Schwierigkeiten.

Dr. Gunnar Arsiholm, Forsvarets forskningsinstitut Kjeller, for his powerful numerical simulation tool Sisyfos that was very important for the succes of the RGB project and for his extremely competent and nice support during the simulations at any time.

Besonders danke ich dem *High-Power Team,* in welchem ich miterleben durfte, was es bedeutet, in ein Team zu arbeiten und welches mich auch in schwierigen Momenten dieser Doktorarbeit immer unterstützt hat. Ich bin überzeugt, dass unsere gute Zusammenarbeit untereinander massgeblich zum Erfolg der Projekte beigetragen hat. Bei Thomas Südmeyer möchte ich mich für eine sehr angenehme und erfolgreiche Zusammenarbeit am zeitweise sehr zickigen YAG Laser („er ist männlich☺") bedanken und für die vielen nützlichen Tips und Tricks bei der Problemlösung (nicht nur im Labor), die ich von ihm lernen konnte. Weiter möchte ich mich bei Thomas für die Vorarbeit bei der Planung des RGB Projektes bedanken, das jedoch leider erst nach seinem Abschluss verwirklicht werden konnte. Bei Felix Brunner möchte ich mich für eine gute und fruchtbare Zusammenarbeit beim RGB Projekt bedanken, die auch nach „aufgelösten" Kristallen und nach 32 Stunden im Labor noch tadellos funtionierte und für seine mutige Verteidigung meinerseits am Conference Dinner der ASSP'02 in Québec. Sergio Vincenzo Marchese möchte ich für die Unterstützung beim Aufbau des 57-MHz Lasers während seiner Diplomarbeit danken, die schlussendlich zum „Weltrekord" Yb:YAG Laser gefüht hat und für die angenehme Laborgemeinschaft mit „cooler" Musik in letzten Jahr.

Dr. Reto Häring für das Design und Dr. Emilio Gini für das Wachstum DES SESAMs, mit welchem wir den Yb:YAG Laser modengekoppelt haben.

Dr. Jürg aus der Au und Dr. Gabriel Spühler für die sehr wichtige Vorarbeit in den Highpower-Projekten, auf deren Basis wir unsere Forschung weiterführen konnten.

Den momentanen und ehemaligen Zimmergenossen vom F17, Dr. Alex Aschwanden (der Tänzer), Aude-Reine Bellancourt (die Skifahrerin), Dr. Felix Brunner (100% Zürcher), Dr. Reto Häring ("du siehst aus wie ein Mikey Mouse"), Dr. Lukas Krainer ("des passt schon"), Dr. Steve Lecomte ("Pralinen für Weihnachten"), Sergio Vincenzo Marchese (per Velo nach Sizilien) und Benjamin Rudin ("das ist … was?") für die gute Büroatmosphäre, die das tägliche Leben sehr angenehm gemacht haben.

Ich danke Stefan für seine liebevolle Unterstützung von Nah und Fern und und sein grosses Verständnis meiner Arbeit gegenüber. Ich freue mich schon jetzt darauf, dass wir die grosse geographische Distanz zwischen uns endlich minimieren können. Ganz besonders danke ich meinen Eltern und meinen Freunden dafür, dass sie mich durch alle Hochs und Tiefs der letzten Jahre liebevoll und tatkräftig unterstützt haben.

Zürich, Mai 2005

(Edith Innerhofer)